# On the Monte Carlo simulation of neutron-induced indirect DNA damage to estimate neutron carcinogenic potential

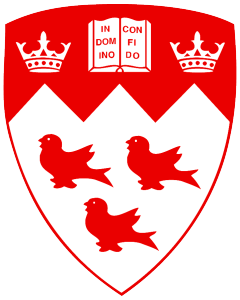


**James Alfred Manalad**

Medical Physics Unit
McGill University, Montreal
December 2021

A thesis submitted to McGill University in partial fulfillment of the requirements for the degree of
*Master of Science in Medical Radiation Physics*

# Acknowledgements

To my supervisor, Dr. John Kildea, thank you so much for all your guidance and support. Most of all, thank you for believing in my abilities when I cannot do so sometimes.
To my mentor, Dr. Logan Montgomery, thank you for the long hours of discussion, review, and editing. I am grateful for all the knowledge and insights you have imparted to me.
To the NICE-ROKS group, thank you for the small moments in our weekly meetings. Special thanks to Felix for helping me structure my outlines and to Luc for translating my work.
To Ives, Jan, and Shirin, thank you for the care that you have for your students.
To Chris and Peter, thank you for all the Geant4 help and tips.
To Alaina, Alana, Kayla, Sabrina, Jorge, and Marc, thank you for the friendship, motivation, inspiration, and love. Strong bonds are indeed formed over mutual suffering.
To the baristas at 2C Van Horne, thank you for all the thesis fuel and my corner spot.
To my parents, siblings by blood, and siblings by choice, thank you for all the love and support.
Finally, to my backbone and life partner, Leah, you have been with me through it all. Thank you for loving and accepting all of me. I am forever grateful for you.

*Mabuhay po kayo!*

P.S. To COVID-19, you will not be missed.

# Abstract

The exposure of patients undergoing high-energy radiotherapy to secondary radiation of neutrons poses a serious risk of iatrogenic secondary cancer induction. Ionizing radiation, such as neutrons, inflicts damage to the DNA via energy depositions to DNA moieties (direct action) and via the radiolysis of nearby water molecules that then generate chemical species that can react with DNA moieties to induce damage (indirect action). This thesis aims to elucidate the underlying mechanisms of neutron-induced carcinogenesis by investigating the role of indirect action in the formation of clustered DNA lesions (especially those containing double-strand breaks or DSBs), believed to be a main mechanism from which radiation-induced mutagenic consequences emerge.

Using the Monte-Carlo-based TOPAS simulation framework and its radiobiological extension TOPAS-nBio, we have expanded an existing simulation pipeline of our research group for direct action to include indirect action. The resulting indirect DNA damage yields (DYs) from simulated irradiations of our in-house nuclear DNA model have been validated with experimental data and benchmarked against previous simulation work. DNA DYs from our simulated monoenergetic neutron irradiations (1 eV to 10 MeV) were compared with those of 250 keV X-rays to estimate the energy-dependent relative biological effectiveness (RBE) of neutrons, our proxy for carcinogenic risk. We found that the majority of neutron-induced DNA damage are isolated simple lesions due to indirect action, while most clustered lesions are hybrid in nature. Our estimated neutron RBE values for inducing DSB-containing clusters or complex DSB clusters (C-DSBs) via independent indirect action fell under those of independent direct action and published radiation protection factors, but were higher than those due to combined (direct and indirect) action despite this latter resulting in significantly more C-DSBs.

# Résumé

L'exposition des patients subissant une radiothérapie à haute énergie au rayonnement secondaire des neutrons présente un risque sérieux d'induction de cancer secondaire iatrogène. Les rayonnements ionisants, tels que les neutrons, endommagent l'ADN via le dépôt d'énergie sur des fragments d'ADN (action directe) et via la radiolyse de molécules d'eau avoisinantes qui génèrent par la suite des espèces chimiques pouvant réagir avec l'ADN et induire des dommages (action indirecte). Cette thèse vise à élucider les mécanismes sous-jacents de la cancérogenèse induite par les neutrons en étudiant le rôle de l'action indirecte dans la formation de dommages multiples locaux (DMLs) de l'ADN (en particulier celles produisant des cassures double-brin ou CDBs), considérées comme un mécanisme important menant aux effets mutagènes radio-induits.

En utilisant l'architecture de simulation Monte-Carlo de TOPAS et l'extension radiobiologique TOPAS-nBio, nous avons ajouté l'action indirecte au système de simulation existant et créé par notre groupe de recherche pour suivre l'action directe. Les rendements de dommages (RDs) indirects à l'ADN résultant d'irradiations simulées par notre modèle d'ADN nucléaire interne ont été validés avec des données expérimentales et comparés à des travaux précédents. Les RDs de l'ADN de nos irradiations neutroniques monoénergétiques simulées (1 eV à 10 MeV) ont été comparées à celles de rayons X de 250 keV pour en estimer l'efficacité biologique relative (EBR) des neutrons, notre mesure de référence du risque cancérogène. Nous avons constaté que la majorité des dommages à l'ADN induits par les neutrons sont des lésions simples isolées dues à l'action indirecte, tandis que la plupart des DMLs sont de nature hybride. Nos valeurs estimées d'EBR neutroniques induisant des DMLs complexes contenant des CDBs (C-CDBs) via une action indirecte indépendante étaient inférieures à celles de l'action directe indépendante et des facteurs de radioprotection publiés, mais étaient supérieures à celles dues à l'action combinée (directe et indirecte), même si cette dernière produit significativement plus de C-CDBs.

# Contents

# List of Figures

# List of Tables

# List of Abbreviations

| | |
|---|---|
| **ALARA** | **A**s **l**ow **a**s **r**easonably **a**chievable |
| **AP** | **Ap**urinic or **Ap**yrimidinic |
| **BD** | **B**ase **d**amage |
| **BER** | **B**ase **e**xcision **r**epair |
| **BP** | **B**ase **p**air |
| **CCS** | **C**anadian **C**ancer **S**ociety |
| **C-DSBs** | **C**omplex **DSB** cluster**s** |
| **CPD** | **C**umulative **p**robability **d**istribution |
| **CPU** | **C**entral **p**rocessing **u**nit |
| **DaMaRiS** | **D**N**A** **M**ech**a**nistic **R**epa**i**r **S**imulator |
| **DNA** | **D**eoxyribo**n**ucleic **a**cid |
| **DSB** | **D**ouble-**s**trand **b**reak |
| **DY** | **D**amage **y**ield |
| **EBRT** | **E**xternal **b**eam **r**adiation **t**herapy |
| **Geant4** | **Ge**ometry **an**d **T**racking version **4** |
| **GPU** | **G**raphics **p**rocessing **u**nit |
| **HRR** | **H**omologous **r**ecombination **r**epair |
| **ICRP** | **I**nternational **C**ommision on **R**adiological **P**rotection |
| **ICRU** | **I**nternational **C**ommission on **R**adiation **U**nits and Measurements |
| **IR** | **I**onizing **r**adiation |

| | |
|---|---|
| **LET** | **L**inear **e**nergy **t**ransfer |
| **Linac** | **Lin**ear **ac**celerator |
| **LMDS** | **L**ocally **m**ultiply **d**amaged **s**ites |
| **LNT** | **L**inear-**n**on-**t**hreshold |
| **MC** | **M**onte **C**arlo |
| **MEDRAS** | **Me**chanistic **D**NA **R**epair **a**nd **S**urvival |
| **MLC** | **M**ulti-**l**eaf **c**ollimator |
| **NHEJ** | **N**on-**h**omologous **e**nd-**j**oining |
| **N-DSBs** | **N**on-**DSB** cluster**s** |
| **OER** | **O**xygen **e**nhancement **r**atio |
| **PDF** | **P**robability **d**istribution **f**unction |
| **RBE** | **R**elative **b**iological **e**ffectiveness |
| **RCS** | **R**eactive **c**arbon **s**pecies |
| **RER** | **R**adiation **e**ffects **r**atio |
| **RF** | **R**adio **f**requency |
| **RIBE** | **R**adiation-**i**nduced **b**ystander **e**ffect |
| **RIGI** | **R**adiation-**i**nduced **g**enomic **i**nstability |
| **RNG** | **R**andom **n**umber **g**enerator |
| **RNS** | **R**eactive **n**itrogen **s**pecies |
| **ROS** | **R**eactive **o**xygen **s**pecies |
| **RT** | **R**adiation **t**herapy or **R**adio**t**herapy |
| **SB** | **S**trand **b**reak |
| **SBY** | **S**trand **b**reak **y**ield |
| **SSB** | **S**ingle-**s**trand **b**reak |
| **TOPAS** | **To**ol for **Pa**rticle **S**imulation |
| **TOPAS-CDD** | **TOPAS C**lustered **D**NA **D**amage |
| **US NRC** | **U**nited **S**tates **N**uclear **R**egulatory **C**ommission |

# Contribution of Authors

This thesis was exclusively written by the author, James Alfred Manalad, with guidance from Dr. John Kildea and Dr. Logan Montgomery. Unless otherwise indicated, all figures and tables were produced by the author. All main sources of help were acknowledged.

- Chapters 1 to 4: The literature review was written entirely by the author. All sources of information were cited properly.
- Chapter 5: All work mentioned that is not of the author were clearly attributed. All the software written for this present project was solely by the author as an expansion to the open-source software TOPAS Clustered DNA Damage (TOPAS-CDD).
- Chapters 6 to 8: All data, analysis, and conclusions presented are the author's own, unless otherwise indicated.

# Chapter 1

# Introduction

## 1.1 Problem statement

Over the last two decades, radiation therapy (RT) (a.k.a. radiotherapy) techniques have become increasingly precise in targeting malignant cells and sparing healthy cells, resulting in improved patient outcomes. However, despite these developments, cancer patients undergoing radiation therapy remain exposed to a non-therapeutic out-of-field secondary radiation. This whole-body dose of secondary radiation poses a risk for iatrogenic second cancer induction. At the same time, the issue of iatrogenic second cancers is becoming increasingly relevant with the advancement of modern diagnostic and treatment techniques that improve the life expectancy of cancer patients.

At high photon energies ($\gtrsim$8 MeV), a spectrum of secondary neutrons contributes to the non-therapeutic dose received by patients undergoing RT. Neutrons are of particular concern with respect to second cancers because their carcinogenic risk is known to be highly energy dependent possibly extending up to 20 times the risk from photons at certain energies, but a complete biophysical model to explain this energy dependence is outstanding. Our research group has previously investigated this energy dependence by developing a computational model to simulate neutron relative biological effectiveness (RBE) for inducing clustered DNA damage as a function of energy [8]. However, this model considered only the direct action of ionizing radiation (IR). Therefore, the purpose of this MSc thesis project was to expand on our previous work by incorporating indirect action, given that it is known to constitute a significant proportion of radiation-induced DNA damage.

## 1.2 Outline

In this thesis, we discuss in Chapter 1 the relevant topics and background knowledge to situate the project in the field, further build up its motivations, and establish its primary objectives. Chapter 2 is a review of the necessary concepts in radiation physics and dosimetry to understand how ionizing particles arise and interact with matter, and how radiation is quantified. Afterwards, Chapter 3 provides sufficient background information in molecular biology, radiochemistry, and organic chemistry to map out at a high level the key steps between human-body exposure to IR and carcinogenesis. In Chapter 4, the topics related to how IR may be computationally simulated are covered in detail. This chapter also serves to discuss the foundational work upon which the present project is built. Chapter 5 recapitulates the objectives of this project and outlines the specific steps undertaken to accomplish them. The results of the work done are presented in Chapter 6 and discussed in Chapter 7 along with the issues encountered. Finally, Chapter 8 summarizes the key points and the results of this project along with some concluding thoughts.

## 1.3 Cancer

### 1.3.1 Cancer burden

Cancer is the leading cause of death in Canada according to the Canadian Cancer Society (CCS) [18]. About one in two Canadians will be diagnosed with some form of cancer during their lifetime and approximately half of those diagnosed with cancer will die from it [18]. Due to the growing and aging Canadian population, the CCS projects an increase of 40% in cancer cases between 2015 and 2030. Such persistent prevalence of cancer serves to inspire continual scientific and medical effort seeking to improve cancer detection, diagnosis, and treatment. For instance, the overall five-year survival rate of cancer patients in Canada has increased over the decades from 25% in the 1940s to 55% in the early 1990s, and is currently estimated to be at 63% [19]. These improvements in survival rates, however, come with an increase in cases of survivors developing second cancers, some of which are due to their radiation treatment [20].

### 1.3.2 What is cancer?

Cancer refers to a large set of diseases that have uncontrolled cell proliferation as their unifying feature. It may emerge anywhere in the human body regardless of one's age. A cell with an abnormal growth often develops into a lump of abnormal cells called a neoplasm (a.k.a tumour). Tumours may be benign or malignant (cancerous). Benign tumours remain confined to their site of origin, while malignant tumours, with their uncontrolled cell division and capacity to invade nearby tissues, may enter the blood and lymph systems and spread elsewhere in the body. Malignant tumours eventually take over their site of proliferation, develop their own blood vessels to support further growth, and cause disruptions in regular functions of the body [21]. Left untreated, malignant tumours may cause organs and/or organ systems to fail and eventually lead to death.

### 1.3.3 Treatment modalities

Benign tumors pose a low health risk to patients and may be treated comparatively simply by surgical removal or by RT localized to the site of the disease and neighbouring healthy tissue. On the other hand, malignant tumors that may or may not have already metastasized (i.e., spread to other parts of the body) pose a significant risk of harm and require additional treatment modalities such as chemotherapy and hormonal therapy that act on the entire body of the patient. Chemotherapy serves to neutralize rapidly-dividing cells (a key characteristic of cancer cells), while hormonal therapy acts to suppress cancerous growth by denial of necessary hormones. For many patients, a combination of these modalities is used to treat their disease. In this thesis, the cancer treatment modality of interest is RT, which is performed for approximately half of all cancer patients [22].

## 1.4 Radiation therapy

Simply put, RT is the medical application of IR to cure or control diseases such as cancer. Depending on the patient's case, the goal of RT may be to protect the patient against the onset of a disease progression (preventive/prophylactic), to eliminate the patient's disease (curative/therapeutic), and/or to improve the patient's quality of life by alleviating symptoms of the disease (palliative). To achieve such goals, careful treatment planning and sophisticated radiation delivery methods capable of maximizing damage to the target lesion while minimizing

damage to healthy tissue must be employed. Radiation delivery in RT may come in the form of brachytherapy or external beam radiation therapy (EBRT).

### 1.4.1 Radiation delivery mechanisms

Brachytherapy involves the insertion of radioactive sources into the patient. The radioactive source is placed close to the tumor site in such a way that most of the radiation is delivered to the malignancy and the nearby healthy tissue is spared as much as possible.

As the name implies, EBRT uses a radiation source that is situated outside of the patient. The beam coming from this source is directed at the patient, but shaped such that radiation is localized to the distinguishable site of malignancy (for therapeutic purposes) and surrounding tissue suspected of harboring subclinical disease (for prophylactic purposes). Historically, radioactive isotopes such as $^{60}$Co were used as the radiation source for EBRT. However, due to the better control of radiation output and choices of IR that they offer, particle accelerators have taken the place of radioactive isotopes. The most commonly used particle accelerator in the context of medical treatments is the medical linear accelerator (or linac). EBRT is the form of RT we are more interested in for the purpose of this thesis due to its widespread use.

### 1.4.2 Medical linear accelerators

Linacs are capable of generating high-energy radiation (usually photon or electron) beams in the MeV range. To generate such beams, a cathode filament inside the linac is first heated to induce thermionic electron emission. The higher the temperature of the filament, the more electrons are emitted. These low-energy electrons are then injected into a cylindrical vacuum chamber known as the waveguide where they are accelerated using high-power radiofrequency (RF) waves. Upon reaching the linac head at the end of the waveguide, the electrons are magnetically focused to hit a high-density metallic target in order to produce high-energy X-ray photons through a phenomenon known as bremsstrahlung (discussed further in Section 2.2.2). The target may also be removed if a direct electron beam is deemed more appropriate to use. In this latter case, the electron pencil beam instead hits a scattering foil to allow for beam spreading. Before the high-energy photon hits the patient, it is first shaped by an array of heavy metal beam-shaping leaves called a multi-leaf collimator (MLC). During EBRT treatments, the leaves of the MLC are arranged such that the resulting radiation beam conforms to the shape of the patient's tumour. The bremsstrahlung target, the scattering foil, and the MLC (among other

beam-shaping, output-monitoring, and shielding components) are all mounted inside a rotating gantry. The placement of the leaves of the MLC may be modified while the gantry is rotating around the patient, which allows for even more conformal radiation delivery to the target region inside the patient lying on the treatment couch. Figure 1.1 shows a simplified schematic diagram of a linac and its various components.

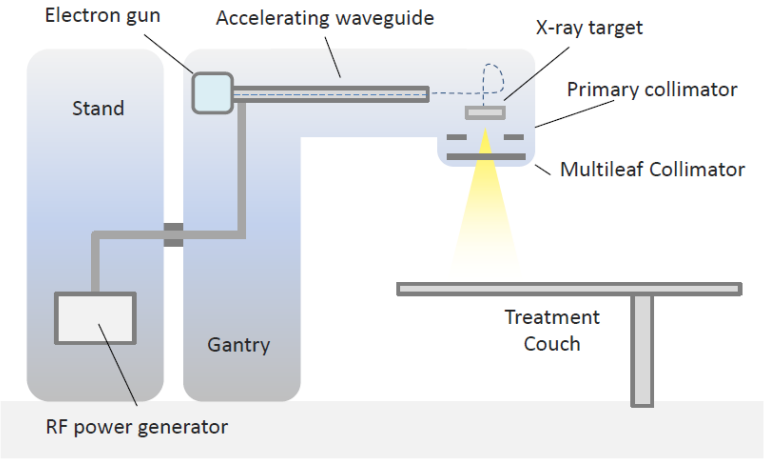


Figure 1.1 A simplified schematic diagram of a linac showing its various components. Figure from H. Patrick [1] with permission.

### 1.4.3 Other medical accelerators

In general, high-energy radiation beams (such as a photon beam coming out from a linac) are capable of penetrating deep into the patient's body. However, for surface treatments, such as those performed for skin cancers, machines capable of producing radiation in the keV range are employed. These units also exploit the bremsstrahlung effect, but use lower energy electrons that are much less penetrating. Specially designed $^{60}$Co machines called Gamma Knife units use highly-conformed gamma rays to treat brain tumours [23]. Recently, EBRT techniques using protons and heavy ions have gained popularity due to these particles being able to deliver the majority of their energies at specific depths that can be matched to the depth of the tumour, thus maximizing the damage to the tumour while minimizing the damage to healthy tissue beyond it. However, there are still significant challenges to be overcome in their development which impedes their widespread use [24].

## 1.5 Secondary radiation

Despite the highly successful advancements in RT in the form of increasingly precise delivery methods of IR that have improved patient outcomes, there still exists a small but statistically significant risk of carcinogenesis post-RT [25].

### 1.5.1 Classification of radiation doses in EBRT

In the context of EBRT, primary radiation refers to the radiation coming directly from the source (i.e., the treatment beam), while secondary radiation refers to radiation resulting from interactions of the primary radiation with matter. During EBRT treatments, patients are exposed to in-field and out-of-field radiation doses. The in-field dose comes mainly from the ionizing particles contained within the field of the primary beam, whereas the out-of-field dose comes strictly from secondary radiation. Moreover, the radiation dose received by the patient may be target or non-target. Target dose is the dose delivered intentionally to the site of malignancy and surrounding healthy tissue accounting for setup and motion errors. On the other hand, non-target dose is the non-therapeutic dose that is received purely consequently by healthy tissue either in-field from primary radiation (as is the case for healthy tissue along the path of the treatment beam), or out-of-field from secondary radiation escaping from the shielded linac head and radiation scattered by the collimating system, the patient, the treatment couch, the walls, and other objects inside the patient and within the shielded treatment room (a.k.a. bunker) [26].

### 1.5.2 Protection against primary and secondary radiation

There are various physical measures that can be put in place designed to protect the public and clinical staff from primary and secondary radiation such as the thick concrete walls and door of the bunker that attenuate the radiation coming from within it to safe levels. Instead of using a massive door that may be challenging to install, some bunkers instead opt for a maze for the same purpose. On the other hand, patients always remain vulnerable to secondary radiation. The out-of-field radiation dose received by patients is found to be dependent on the distance from the treatment field and is estimated to be around 0.01–1% of the target dose [26]. Although insufficient to cause radiation burns and other deterministic effects (i.e., direct cause-and-effect observables due to irradiation), secondary radiation may bring about carcinogenic risk and other

long-term stochastic effects (i.e., probabilistic consequences). The focus of this thesis is on the stochastic effects of secondary radiation, in particular those arising from neutrons.

## 1.6 Neutron risk

During high-energy EBRT ($\gtrsim$8 MeV) treatments, ensuing photonuclear and electronuclear interactions result in the emission of highly penetrating secondary neutrons that are scattered everywhere inside the patient and the bunker. At photon beam energies $\gtrsim$10 MeV, the proportion of contaminating neutrons originating from the linac head becomes relevant [26]. The various radiation-matter interactions involved are discussed in Sections 2.2 to 2.4. Among the secondary radiations that permeate the bunker, neutrons are of particular interest with regard to second cancer induction due to their elevated radiation weighting and quality factors compared with other types of radiation, which denote greater associated biological risk.

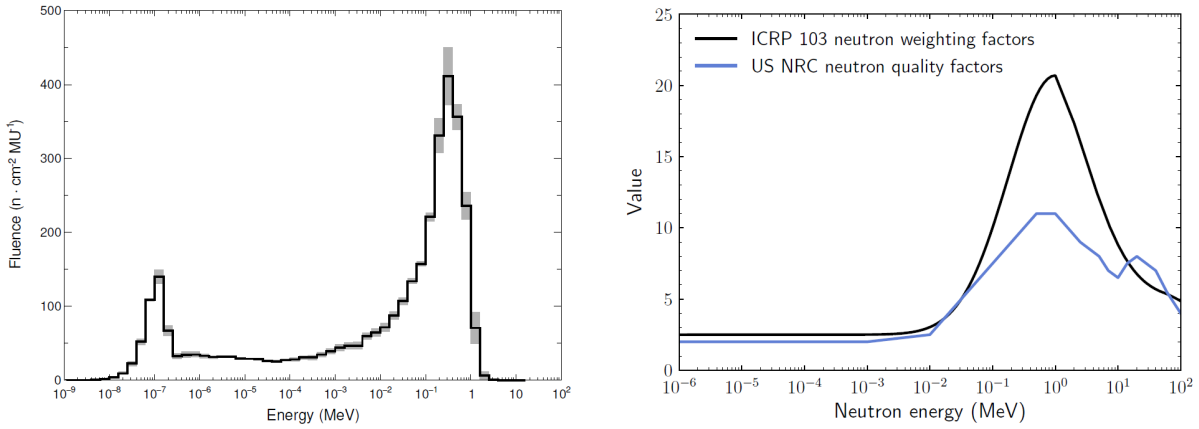


(a) (b)

Figure 1.2 (a) Dose-normalized neutron fluence spectrum of a 10 MV beam from a Varian TrueBeam linac measured 100 cm from the gantry. (b) Plots of the ICRP neutron weighting factors and US NRC neutron quality factors. Figures from L. Montgomery [2] with permission.

The neutron radiation weighting factors ($w_R$) of the International Commision on Radiological Protection (ICRP) [10] and the neutron quality factors ($Q$) of the United States Nuclear Regulatory Commission (US NRC) [11] are experimentally-extracted consensus values that serve to characterize the general associated biological risk of neutron irradiation. The higher these values are, the greater the associated biological risk. The experimental basis of these factors stem from combined neutron relative biological effectiveness (RBE) data collected for a

variety of stochastic biological endpoints [10]. Neutron RBE simply describes how much more potent neutrons are compared to another type of radiation for inducing the same endpoint (more details in Section 2.5.2).

Measurements of neutron fluence performed to estimate the spectrum of neutron energies received by patients during high-energy EBRT demonstrate a minor thermal fluence peak at around 0.025 eV and a major fast neutron peak around 1 MeV as can be seen in Figure 1.2-a. The latter peak at about 1 MeV is of particular importance because the neutron radiation weighting and quality factors exhibit a peak at a similar energy as depicted in Figure 1.2-b. This means that the majority of neutrons are encountered by patients at the energy at which they are most biologically damaging. Both the ICRP weighting factors and the US NRC quality factors display an energy dependence and peak at around 1 MeV for neutrons. However, clear discrepancies between the two sets of factors (particularly in the peak magnitude) can be observed. Indeed, such discrepancies have served to motivate our research group's previous work on investigating neutron RBE for inducing clusters of DNA lesions (via direct action of IR), with the goal of producing a fundamental model explaining the energy dependence of neutron RBE for stochastic effects [8].

## 1.7 Indirect action of neutron radiation

In general, IR acts to inflict damage to the DNA molecule via two distinct mechanisms: direct and indirect action (a.k.a. direct and indirect effects). Direct action refers to the direct interaction between ionizing particles and DNA constituent molecules via energy depositions in the molecules themselves that may lead to DNA damage. On the other hand, indirect action refers to the potentially-damaging interactions between DNA constituent molecules and reactive chemical molecules produced via radiation-water interactions in the aqueous material surrounding the DNA. These mechanisms are revisited in greater detail in Section 3.2.

The exploration of DNA damage is of particular relevance in this thesis because of its role in the emergence of neoplasms due to the carcinogenic effects of IR. Radiation-induced carcinogenesis is further discussed in Section 3, but may be summarized as follows: IR effectively inflicts clusters of DNA lesions (via direct and indirect action) that are mitigated by error-prone repair mechanisms, the lingering errors of which may result in an increased number of mutations that may accumulate over time to transform a healthy cell into a cancerous cell. In

this thesis, we focus on how the indirect action of neutron radiation is implicated in this chain of events leading to radiation-induced carcinogenesis by neutrons.

In dosimetry, IR can be characterized using a metric known as linear energy transfer (LET) (discussed further in Section 2.1.4), which describes the distribution of energy deposition along the path of an ionizing particle. The higher the LET of an ionizing particle, the denser the ionization events along its path. Indirect action has been shown to be the dominant damage-inflicting mechanism of IR for low-LET particles (such as electrons and high-energy protons) [27], and a significant damage contributor for high-LET particles (such as low-energy protons and alpha particles) [28, 29]. The interest in exploring DNA damage due to indirect action of neutron radiation stems from previous findings of our research group revealing that the primary contributors to secondary neutron dose relevant to high-energy EBRT are electrons and protons of various energies and LETs where indirect action may be dominant [7]. Further, our group's recent effort in developing a model that elucidates the energy dependence of neutron RBE for stochastic effects only considered direct action of neutron radiation to the DNA molecule [2, 8]. This thesis serves as an expansion that incorporates the effects of indirect action.

## 1.8 Computational models

An important component of this thesis is the use of computational simulations to model DNA damage mechanisms of IR. Recent advances in computation technology and the development of experimentally-validated software for radiation transport simulation permit the practical use of *in silico* models in the study of radiation-induced DNA damage.

Recent work using Monte Carlo (MC) simulations (further explored in Chapter 4) of direct and indirect action by protons and alpha radiation on geometric DNA models demonstrated that indirect action substantially increases the yield of DNA damage in the form of double-strand breaks (which are implicated in the formation of clustered lesions) [4, 30, 31]. Certainly, such results, which may be used as points of comparison, further motivate our investigation on the role of indirect action in inducing carcinogenesis by neutrons using computational methods. Further, the work of Montgomery *et al*. (2021) [8], which we aim on expanding, was performed by simulating neutron irradiation of a geometric DNA model that was developed in-house. Thus, for proper expansion and direct comparison of results, the use of similar computational methods in this project was imperative.

## 1.9 Project objectives: first look

In this thesis, we explore the neutron-induced carcinogenic risk related to indirect action. We hypothesize that the energy dependence of the carcinogenic effects of neutron irradiation (as reflected in the ICRP neutron weighting factors and US NRC neutron quality factors) may be explained by the energy-dependent RBE of neutrons for inducing clusters of DNA lesions via both direct and indirect action. The prior work of our group [8] focused on the contribution of direct action whose resulting RBE values were indeed shown to follow a similar trend as the neutron radiation weighting and quality factors. Meanwhile, this present work explores the contribution of indirect action. Specifically, in this thesis project, we had the following primary objectives:

1. Expand the simulation code of Montgomery *et al*. (2021) [8, 32] to incorporate indirect action and indirect damage scoring.
2. Validate the implementation of indirect action and indirect damage scoring by comparing indirect damage yields with published values.
3. Quantify neutron-induced carcinogenic risk by estimating the RBE of monoenergetic neutrons for inducing simulated clustered DNA damage due to:
   (a) Indirect action alone.
   (b) The combined effects of direct and indirect actions.
4. Evaluate the quantification of neutron-induced carcinogenic risk by comparing the energy-dependent neutron RBE curves obtained from objective 3 with:
   (a) The neutron RBE for clustered DNA damage due to direct action alone [6, 8].
   (b) The ICRP neutron radiation weighting factors [10].
   (c) The US NRC neutron quality factors [11].

Details regarding the Monte Carlo simulations implicated in these objectives are discussed in Chapters 4 and 5. The objectives of this thesis are revisited and expanded upon in Chapter 5.

# Chapter 2

# Radiation Physics and Dosimetry

This chapter serves to define the various physical and dosimetric concepts related to IR and present the underlying physics of the many interactions of IR with matter at the atomic and subatomic scales.

## 2.1 Concepts related to ionizing radiation

### 2.1.1 The structure of the atom

In the Rutherford-Bohr model, an atom is composed of a positively charged nucleus and a negatively charged electron ($e^-$) cloud held together by the attractive electromagnetic force. The nucleus contains at least one proton ($p^+$) that is positively charged and zero or more neutrons ($n^0$) that are electrically neutral (or uncharged). The constituent particles of the nucleus (i.e., protons and neutrons) are referred to as nucleons and they are bound together by the strong nuclear force. The electron cloud is composed of layers of shells or orbitals corresponding to discrete (or quantized) energy levels. Electrons in the inner shells (lower energy levels) are more tightly bound to the nucleus than those in the outer shells (higher energy levels) due to the distance-dependence of the electromagnetic force. An atom has the same number of electrons as protons and so has a net charge of zero (i.e., it is neutral). An atom or a group of atoms (i.e., a molecule) that has a non-zero net positive or negative charge is referred to as an ion.

### 2.1.2 Excitation and ionization

An electron bound to an atom is said to be in the ground state if it is in the orbital having the lowest energy level. Through a process known as electronic excitation, an electron may be promoted to a higher energy state (or an excited state), leaving a vacancy in its original orbital. This process occurs if the electron obtains a specific amount of energy identical to the energy difference between its current orbital and a higher-energy orbital via interactions with radiation involving energy transfer. Inversely, electrons in a higher energy state may relax to a lower energy state to fill inner-shell vacancies. This de-excitation process respects conservation laws via the emission of photons referred to as characteristic X-rays. The name comes from the fact that these X-rays have a discrete energy corresponding to the electronic structure of their atom of origin. Similar to atomic electrons, atomic nuclei also have quantized energy states and thus, may undergo excitation and eventual de-excitation.

Given sufficient energy, an electron may be able to escape its atom, which results in the atom's ionization (i.e., the atom becomes an ion). In general, ionization refers to any physical or chemical process resulting in the gain or loss of electrons in atoms. Similar to electronic excitation, atomic ionization via ejection of inner-shell electrons also results in vacancies that may be filled-in by outer-shell electrons followed by characteristic X-ray emissions. The energy required to eject an electron from its shell is referred to as its binding energy. Electrons in the inner shells are more tightly-bound due to their higher binding energy. The ionization potential of an atom or a molecule corresponds to the binding energy of its least bound electron.

### 2.1.3 Classification of ionizing radiation

As denoted by the name, IR refers to subatomic particles capable of inducing ionization of atoms. IR may be classified as directly ionizing or indirectly ionizing. Directly-ionizing radiation refers to charged particles such as electrons, protons, and ions, while indirectly-ionizing radiation refers to neutral particles such as photons and neutrons. IR may also be classified according to its place of origin: nuclear or non-nuclear. Nuclear radiation, as the name implies, refers to ionizing particles coming from the nucleus which include alpha ($\alpha$) particles (helium nuclei composed of 2 protons and 2 neutrons), beta ($\beta$) particles (electrons or positrons), gamma ($\gamma$) rays (photons), and neutrons. Non-nuclear radiation comprises all the rest of ionizing particles that are not emitted from the atomic nucleus.

### 2.1.4 Linear energy transfer

An important physical quantity that is used to characterize IR is linear energy transfer (LET). For IR traversing a medium, LET is defined as the rate of energy absorption ($E$) by the medium along the path ($l$) of the radiation:

$$LET = \frac{dE}{dl} \tag{2.1}$$

In essence, LET describes the spatial density of ionizations in the medium. IR with LET < 10 keV/$\mu$m (low-LET) is considered as sparsely-ionizing, whereas LET > 10 keV/$\mu$m (high-LET) denotes that the radiation is densely-ionizing [9]. Table 2.1 summarizes examples of low-LET and high-LET radiations.

Table 2.1 Types of ionizing radiation with their respective LET values [9].

| | Particle | Kinetic energy | LET (keV/$\mu$m) |
|---|---|---|---|
| Low-LET | X-rays | 3 MeV | 0.3 |
| | | 250 keV | 2 |
| | Electrons | 1 MeV | 0.25 |
| | | 10 keV | 2.3 |
| High-LET | | 1 keV | 12.3 |
| | Neutrons | 14 MeV | 12 |
| | Protons | 2 MeV | 17 |
| | Carbon ions | 100 MeV | 100-2000 |

### 2.1.5 Cross sections

Radiation transport is a stochastic process. As ionizing particles travel through a medium, they undergo a series of discrete and probabilistic interactions. The probability of occurrence (or cross section) of these interactions is dependent upon various factors such as particle type and energy, and the physical properties of the medium. Radiation transport can be modeled on the macroscopic scale given that these interaction probabilities converge to mean values.

## 2.2 Charged particles

Charged particles are particles that are subject to electromagnetic forces due to their electric charge and induced magnetic fields caused by their motion. Charged particles that are freely propagating in space and have sufficient energy to ionize the atoms they encounter are considered directly-ionizing radiation.

### 2.2.1 Classification of charged particles

Charged particles may be grouped according to their mass: light, intermediate, or heavy. Light charged particles refer to electrons and positrons, intermediate charged particles include charged muons and pions, while heavy charged particles refer to protons, alphas, and heavier ions.

### 2.2.2 Interactions of charged particles

The interactions of charged particles with atoms of an absorbing medium are governed by Coulomb interactions with either orbital electrons or atomic nuclei. The type of Coulomb collision that occurs depends on the relative magnitude of the impact parameter $b$, which is the closest distance between the trajectory of the charged particle and the center of the atom's nucleus, compared to the outer radius $a$ of the target atom as depicted in Figure 2.1.

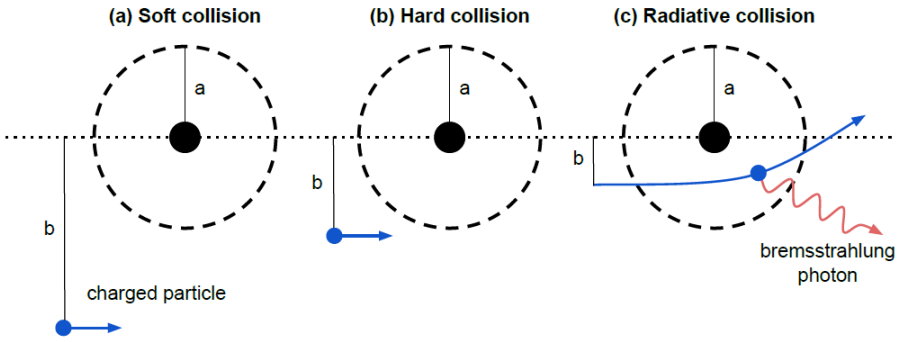


Figure 2.1 The different types of Coulomb interactions showing outer atomic radius $a$ and impact parameter $b$: (a) soft collision where $b \gg a$, (b) hard collision where $b \approx a$, and (c) radiative collision where $b \ll a$. Figure from L. Montgomery [2] with permission.

### Soft collisions

A soft (a.k.a. distant) collision occurs when the incident charged particle passes relatively far away from the target atom ($b \gg a$). In this case, the incident charged particle interacts with the bound electrons of the target atom via transfer of some energy that could induce atomic polarization, excitation, or ionization [9]. Soft collisions are the vastly dominant type of interaction for charged particles, but only a small amount of energy is transferred in each interaction.

### Hard collisions

A hard (a.k.a. close) collision occurs when the incident charged particle arrives at a point nearly tangential to the outer radius ($b \approx a$). In this case, the charged particle may interact with a single bound electron via transfer of a significant amount of energy that most likely induces ionization. The electron emitted via such interaction is known as a $\delta$-ray if it has enough energy to enter into further Coulomb interactions with nearby atoms. Although the cross section of soft collisions is much higher than hard collisions, the energy absorbed by the medium via hard collisions is much greater. The proportion of energy transferred from the incoming particle to the bound electron is dependent on the mass of the incoming particle. Incident electrons may transfer all of their kinetic energy in one hard collision, whereas heavy charged particles may only transfer a relatively small portion of their energy. A hard collision between an incident positron and an atomic electron leads to the annihilation of both particles, simultaneously creating an electron vacancy and emitting annihilation photons. About 50% of the total energy transferred by incident charged particles to the medium is via soft and hard collisions [9].

### Radiative collisions

A radiative collision occurs when the incident charged particle gets in close enough proximity with the nucleus to interact with the latter's Coulomb field ($b \ll a$). In most cases, these interactions are effectively elastic collisions and only involve a slight angular deflection of the incident particle's trajectory [9]. However, in the case of inelastic collisions, the electromagnetic interaction between the incident particle and the nucleus results in the slowing down of the particle. The kinetic energy lost by the decelerating particle is emitted away as an X-ray photon in a process referred to as bremsstrahlung (German word for "braking radiation") production.

The angle of emission of the bremsstrahlung photon is dependent on the kinetic energy of the incoming particle. The higher the kinetic energy of the incident charged particle, the more forward (i.e., closer to the direction of the incident particle) the direction of photon emission. The overall intensity of the bremsstrahlung photons is proportional to the factor $(zZ/m)^2$ where $z$ and $m$ are respectively the atomic number and mass of the incident charged particle, and $Z$ is the atomic number of the target atom. Given such dependencies for direction and intensity of photon emission, high-energy electrons impinging on a high-$Z$ target material is an effective way to generate high-energy X-ray photons that may be used for medical purposes.

## 2.3 Photons

Electromagnetic radiation may be subdivided into discrete particulate chunks (or quanta) known as photons. Photons are massless particles of energy that travel at the speed of light $c$ ($c = 2.998 \times 10^8$ m/s in vacuum) and may be classified as non-ionizing or ionizing radiation depending on their individual energy relative to the materials they encounter. Photon energy is defined as $h\nu$ where $h$ is Planck's constant ($h = 6.626 \times 10^{-34}$ J·s) and $\nu$ is the photon's frequency (derived from its wave-like properties). Non-ionizing photons have insufficient energy to induce ionization of target atoms and thus, are typically absorbed as heat. Although non-ionizing photons may induce burns at very high intensities, they are considered biologically safe in typical scenarios. The type of photon radiation of concern in radiation safety is ionizing photons. Ionizing photons (i.e., photons with enough energy to induce ionization) are either X-rays or $\gamma$-rays. Historically, $\gamma$-rays were considered to have higher energies than X-rays, but with the advent of modern particle accelerators, the two are now differentiated by their place of origin. X-rays are generated extra-nuclearly via de-excitation of bound electrons and bremsstrahlung production, while $\gamma$-rays are generated via de-excitation of excited nuclei and nuclear interactions. The cross sections of photon interactions with matter depend heavily on the photon energy $h\nu$, the absorbing medium's atomic number $Z$ and mass density $\rho$.

### 2.3.1 Linear attenuation

Unlike charged particles that can deposit their energy incrementally over multiple interactions along their trajectories, incident photons may only be (i) completely absorbed, (ii) partially absorbed and scattered, or (iii) just scattered upon interaction in a medium. The intensity of a

photon beam is proportional to the amount of individual photons in the beam. When a photon beam travels through a medium, its intensity decreases with increasing penetration depth as individual photons are stochastically absorbed or scattered out of the beam by the medium. The described decrease in intensity is known as the linear attenuation of photons and it is modeled macroscopically by the Beer-Lambert law:

$$I(d) = I_0 e^{-\mu d} \tag{2.2}$$

where $I(d)$ is the depth-dependent intensity, $I_0$ is the initial intensity, $\mu$ is the linear attenuation coefficient, and $d$ is the depth travelled inside the medium. The coefficient $\mu$ in this generalized equation encapsulates the different cross sections of each photon interaction in the medium. Thus, $\mu$ is a function of $h\nu$, $Z$, and $\rho$.

### 2.3.2 Interactions of photons

Photons undergo a number of different interactions that may lead to scattering, photoexcitation, photoionization, or combinations thereof. The scattering of a photon simply refers to the deflection of its trajectory and may involve energy loss and absorption of its energy by the medium. Photoexcitation and photoionization respectively refer to excitation and ionization induced by photon absorption. Photoexcitation only occurs for specific photon energies absorbed by atomic electrons or nuclei due to the quantized nature of electronic and nuclear energy states, whereas photoionization only occurs for photon energies exceeding the binding energy of their target atomic electrons. Depending on the energy of the incident photon, there may be more particles emitted from the ionized atom along with the photon-absorbing electron. The most important photon interactions relevant to EBRT ($\lesssim$20 MeV) are described in the following sections.

#### Thomson scattering

Thomson scattering occurs when a photon interacts with a loosely-bound electron where the oscillating electric field of the photon acts to oscillate the electron at the same frequency which effectively results in the deflection of the photon with negligible energy loss [9]. Thomson scattering is most prominent for low-energy photons ($h\nu \ll m_e c^2$) on high-$Z$ materials.

### Compton effect

The Compton effect (a.k.a incoherent photon scattering) occurs when a photon interacts with a loosely-bound electron via energy transfer resulting in both the emission of the target electron and the photon with reduced energy and a different direction. Effectively, this interaction can be viewed as a partial energy transfer of the incident photon to the electron resulting in the electron's ejection and the deflection of the photon. The distribution of energy to the emitted electron and scattered photon post-interaction, as well as their respective scattering angles, are well-defined but stochastic in nature. Compton scattering is the dominating photon interaction in low-$Z$ materials (and in high-$Z$ materials for photons in the intermediate energy range 800 keV $\lesssim h\nu \lesssim$ 4 MeV) [9].

### Rayleigh scattering

Rayleigh scattering (a.k.a. coherent photon scattering) is the deflection of an incident photon due to its interaction with tightly-bound atomic electrons where the atom is neither excited nor ionized. The target atom as a whole absorbs the transferred momentum, but because of its minuscule recoil energy, there is negligible energy loss for the photon [9]. Rayleigh scattering occurs mostly for low-energy photons on high-$Z$ materials.

### Photoelectric effect

The photoelectric effect occurs when an incident photon interacts with a tightly-bound electron via complete energy transfer resulting in the emission of the electron. As such, the kinetic energy of the emitted electron is equivalent to the difference between the incident photon's energy and the electron's binding energy. The photoelectric effect is the prevailing interaction for lower-energy photons on high-$Z$ materials where they have sufficient energy to induce electron emissions (10 keV $\lesssim h\nu \lesssim$ 1 MeV) [9].

### Auger effect and internal conversion

Auger effect and internal conversion are interactions of photons coming from within an atom with electrons bound in the same atom. Both result in the emission of the electrons taking part in the interaction. The difference between the two interactions is that the photons interacting via

the Auger effect are characteristic X-rays due to electronic de-excitation, whereas the photons in internal conversion are $\gamma$-rays due to nuclear processes.

#### Pair production and triplet production

Pair production occurs when a high-energy photon interacts with the electric field of the target atom's nucleus to spontaneously produce an electron-positron pair. To respect conservation laws, the photon energy must exceed 1.022 MeV (i.e., the combined rest mass energy of an electron and a positron) for this process to occur. Photons with energies greater than 2.044 MeV may instead interact with the electric field of a bound electron and undergo triplet production. Similar to pair production, an electron-positron pair is created in triplet production with the added ejection of the target electron. These interactions are dominant for incident high-energy photons ($\gtrsim$4 MeV) on high-$Z$ materials [9].

#### Photoneutron production

Photonuclear interactions (a.k.a. photodisintegration) refer to a set of interactions where photons directly interact with atomic nuclei to induce nuclear instability and subsequent emission of nuclear fragments. In the case of high-energy photon EBRT, the most common of these interactions is photoneutron production where a neutron is emitted from the nucleus subsequent to the absorption of an incident photon. Neutrons, protons, and alpha particles are relatively easy to liberate from the nucleus compared to heavier ions because they have the least binding energies. For photoneutron production to occur, the energy of the incoming photon must exceed a threshold of approximately 10 MeV [9]. Compared to the overall attenuation of photons via other photon-matter interactions in the absorbing media, photon attenuation via photoneutron production may be deemed negligible. However, due to the significant biological risks brought about by secondary neutrons, photoneutron production must be considered in radiation safety.

## 2.4 Neutrons

Neutrons are uncharged particles having a slightly larger mass than protons. They are typically bound with protons via the strong nuclear force forming the nucleus of atoms. However, they may be liberated or freed from atomic nuclei via certain physical interactions.

### 2.4.1 Classification of neutrons

Free neutrons are commonly categorized according to their kinetic energy due to the energy-dependence of their cross sections. This classification is summarized in Table 2.2.

Table 2.2 Classification of neutrons according to their kinetic energy $E_K$ [9].

| Category | Kinetic energy range |
|---|---|
| Ultracold | $E_K < 2 \times 10^{-7}$ eV |
| Very cold | $2 \times 10^{-7}$ eV $\leq E_K \leq 5 \times 10^{-5}$ eV |
| Cold | $5 \times 10^{-5}$ eV $\leq E_K \leq 0.025$ eV |
| Thermal | $E_K \approx 0.025$ eV |
| Epithermal | 1 eV $\leq E_K \leq 1$ keV |
| Intermediate | 1 keV $\leq E_K \leq 100$ keV |
| Fast | 100 keV $\leq E_K \leq 20$ MeV |
| Relativistic | 20 MeV $\leq E_K$ |

### 2.4.2 Interactions of neutrons

Similar to photons, neutrons are neutral and indirectly ionizing, but unlike photons, neutrons are relatively massive and primarily interact with atomic nuclei instead of bound electrons.

#### Elastic scattering

Similar to elastic collision scenarios in the macroscopic scale, the elastic scattering of non-relativistic neutrons with atomic nuclei conserves both energy and momentum. In this interaction, the incident neutron induces some recoil and energy transfer to the nucleus. The energy transferred in this process is inversely dependent on the atomic mass. Thus, neutron interactions with hydrogen atoms, having the least atomic mass, result in maximum energy transfer. Accordingly, hydrogenous materials such as water, polyethylene, and concrete provide effective neutron moderation for neutron detection and shielding purposes.

The cross section of neutron elastic scattering for most materials is relatively constant with incident neutron energy except for some resonance peaks with certain materials. In these resonance cases of elastic scattering, the neutron is absorbed by the target nucleus resulting in a compound nucleus, which then triggers the emission of a single neutron having identical kinetic energy as the incident particle [33].

### Inelastic scattering

The inelastic scattering of neutrons is similar to the resonance cases of elastic scattering in that the incident neutron becomes absorbed by the target nucleus to form an excited compound nucleus that then de-excites via particle emission. The difference is that in this de-excitation process, two particles are instead emitted: (i) a neutron with less kinetic energy compared to the incident neutron, and (ii) a gamma photon. Neutron inelastic scattering only occurs past a certain incident energy threshold ($\sim$MeV) that differs between materials.

### Neutron capture

Neutron capture, similar to scattering interactions, occurs when an incident neutron merges with a target nucleus forming a compound nucleus. Unlike scattering interactions, however, the neutron stays inside the nucleus in this case. To de-excite, the compound nucleus instead emits a $\gamma$-ray or a charged particle depending on the incident neutron energy. For incident neutrons with energies $\lesssim$1 MeV, the cross sections for neutron capture is inversely proportional to neutron velocity [34]. In other words, the faster neutrons are, the more difficult they are to capture via the short-range strong nuclear force.

### Neutron-induced fission

Neutron-induced fission refers to the interaction between an incident thermal neutron and a nucleus with sufficiently-high $Z$ that induces the splitting of the heavy nucleus into two smaller daughter nuclei. This interaction involves the release of a large amount of energy and the emission of $\gamma$-rays and fast neutrons. These emitted neutrons, if slowed to thermal energies, may induce further nuclear fission, leading to a chain reaction of highly exothermic processes. Indeed, controlled neutron-induced fission is the underlying principle behind nuclear reactors. This interaction is of little importance in the context of RT since fissionable nuclei are typically not present during RT treatments.

### Neutron-induced nuclear spallation

Nuclear spallation is the fragmentation of a nucleus into multiple smaller components due to the intense impact of an incident extremely high-energy neutron ($\gtrsim$100 MeV) [9]. Similar

to nuclear fission, this interaction is not significant in the context of RT given the absence of neutrons having such energies.

### 2.4.3 Neutron secondary particle spectra

Neutron cross section data on the most abundant elements in the human body (hydrogen, oxygen, carbon, and nitrogen) demonstrate that the most likely interactions between neutrons and human tissue are elastic scattering and neutron capture (with significant contribution from inelastic scattering at higher neutron energies) [35]. Following their production during high-energy photon EBRT, photoneutrons (see Section 2.3.2) undergo neutron-matter interactions with atomic nuclei of various nearby objects and human tissue to generate $\gamma$-rays (from inelastic scattering and neutron capture) and charged particles (from neutron capture). The gamma emissions may then interact with nearby atoms to liberate electrons via photon-matter interactions. The variety of ionizing particles (with varying energies) that are effectively generated via neutron-matter interactions and subsequent processes constitute the neutron secondary particle spectra. This collection of ionizing particles forms the IR implicated in the mechanisms of direct and indirect action that inflict DNA damage as described in Section 3.2.1.

## 2.5 Dosimetric concepts

### 2.5.1 Absorbed dose

Absorbed dose is an important metric used in medical physics and health physics to quantify the amount of radiation received by an irradiated medium. Technically, absorbed dose is defined as the ratio of the energy absorbed by a point volume and its mass. In practice, this quantity is extended and averaged over a macroscopic volume and is mathematically described as:

$$D = \frac{\Delta E_{abs}}{\Delta m} \tag{2.3}$$

where $\Delta E_{abs}$ is the energy absorbed by an irradiated volume of mass $\Delta m$. Absorbed dose is expressed in units of gray (Gy) which is equivalent to joules per kilogram (J/kg). For consistency with literature conventions, absorbed dose is referred to as dose in this thesis.

### 2.5.2 Relative biological effectiveness

The manner by which IR deposits energy depends heavily upon the nature of the ionizing particle and its energy. As described previously, relative biological effectiveness (RBE) is a measure of the relative potency between two types of radiation for inducing a certain biological endpoint. Radiobiological endpoints can be any quantitative biological value such as life-shortening, incidence rate of carcinogenesis, number of chromosomal aberrations, number of DNA strand breaks, etc. Technically, RBE is defined to be the ratio of doses required by a reference radiation $X$ (typically 250 keV X-rays, or $\gamma$-rays from a $^{60}$Co or $^{137}$Cs source) and a test radiation to induce the same biological effect:

$$\text{RBE} = \frac{D_X}{D_{test}} \tag{2.4}$$

Although RBE is dependent upon various factors beyond the specified biological endpoint (such as dose rate and tissue and cell type), RBE for stochastic effects generally peaks at the low-dose region, while RBE for deterministic effects peaks at the high-dose region [10].

In practice, it is often challenging to obtain identical levels of biological effect from two different radiation types. In contrast, it is relatively easy to ensure equal amounts of dose delivered. As such, many studies on RBE instead use the radiation effects ratio (RER) which compares the induced biological effects of two radiation qualities at the same dose [36]. Throughout this thesis, the more familiar term RBE is used to refer to RER to be consistent with the literature.

### 2.5.3 Equivalent dose and radiation weighting factors

To incorporate differences in the biological effectiveness of various radiation types into radiation protection, the ICRP established the use of radiation weighting factors ($w_R$) to calculate a dosimetric quantity referred to as equivalent dose ($H_T$). Equivalent dose is the sum of absorbed doses $D_{T,R}$ (to a specific tissue or organ $T$ by one or more types of radiation $R$) multiplied by a corresponding radiation weighting factor. Mathematically, equivalent dose is expressed as:

$$H_T = \sum_R w_R D_{T,R} \tag{2.5}$$

Equivalent dose is indicated in units of sieverts (Sv) which is mathematically equivalent to Gy, but is used to distinguish equivalent dose from absorbed dose. The radiation weighting factors published by the ICRP are based on combined data from a large number of experiments and analyses including epidemiological studies, simulations, and low-dose RBE experiments for inducing various stochastic effects such as life-shortening and carcinogenesis in animals [10]. The $w_R$ factors are meant to be used in radiation protection, and are thus conservative estimates of risk for a variety of stochastic effects. Moreover, these weighting factors are updated as new experimental data become available. The most recent ICRP radiation weighting factors can be found in ICRP Publications 92 [37] and 103 [10].

Table 2.3 The ICRP radiation weighting factors and US NRC radiation quality factors for various radiation types [10, 11]. The corresponding neutron factors are energy-dependent and were shown earlier in Figure 1.2-b.

| Radiation type | Radiation weighting factor $w_R$ | Radiation quality factor $Q$ |
|---|---|---|
| Photons (X-rays, $\gamma$-rays) | 1 | 1 |
| Electrons, $\beta$ radiation, muons | 1 | 1 |
| Alpha particles, heavy ions, fission fragments | 20 | 20 |
| Protons, charged pions | 2 | 10 |

Similar to the ICRP, the US NRC has also developed a set of weighting factors referred to as radiation quality factors ($Q$) to characterize radiation-related biological risk [11]. Table 2.3 summarizes the value of $w_R$ and $Q$ for different types of radiation. The higher the value of the radiation factor, the higher the associated biological risk. Both the ICRP neutron weighting factors and the US NRC neutron quality factors are energy-dependent and are shown in Figure 1.2-b of Section 1.6. Although essential in radiation protection, it is important to recognize that these quantities are not intended for estimating carcinogenic risk.

### 2.5.4 Effective dose and tissue weighting factors

To account for variations in the radiosensitivity of different tissues and organs in the human body, a corresponding set of tissue weighting factors ($w_T$) were also published by the ICRP [38]. These factors are used to calculate a quantity known as the effective dose ($E$) (also expressed in Sv) which is the sum of equivalent doses (in all irradiated tissues and organs) scaled by their

associated tissue weighting factor:

$$E = \sum_T w_T H_T \tag{2.6}$$

### 2.5.5 Dose equivalents

In the event of an actual exposure of a human body to IR, measurable quantities (unlike equivalent dose and effective dose) known as dose equivalents may be used to quantify the dose received by the body [10]. Generally speaking, dose equivalent is simply the product of the absorbed dose and the appropriate quality factor $Q$ (from the US NRC) for the IR. The particular dose equivalent quantity pertinent to this thesis is the ambient dose equivalent $H^*(10)$ which is the dose equivalent measured at a radial depth of 10 mm in the ICRU sphere, a phantom sphere of ICRU 4-element soft tissue ($\rho = 1$ g/cm$^3$, mass composition: 76.2% oxygen, 11.1% carbon, 10.1% hydrogen, and 2.6% nitrogen) with a diameter of 30 cm intended to approximate the human torso [5].

# Chapter 3

# Radiation-induced Carcinogenesis

IR is potentially capable of interacting with any molecule in an organism because, unlike various other cytotoxic agents, ionizing particles are not hindered by biological barriers such as the selective channels of cellular membranes. In contrast with the physical processes described in Sections 2.2 to 2.4 that last up to approximately a few femtoseconds, stochastic radiation-induced biological effects may not be evident until years or decades post-irradiation. Even worse, heritable effects may take generations to manifest [39]. In this chapter, we discuss the necessary biological, radiochemical, and organochemical concepts to explore the various pathways by which exposure to IR may eventually lead to carcinogenesis.

## 3.1 The DNA molecule

The deoxyribonucleic acid (DNA) molecule is a long and complex molecule that encodes the genetic information of life. This genetic code dictates the physical characteristics of organisms and the proper functioning of the biological mechanisms required to sustain life and maximize the chance of reproduction. Prior to exploring the carcinogenic consequences induced by IR, it is important to understand the naturally-present molecular structures and processes in biological systems starting with DNA, which is the primary sensitive target in cells that is believed to be correlated with the cancerous effects of radiation exposure [39].

### 3.1.1 Structure of the DNA molecule

A nucleotide (shown in Figure 3.1-a) is the basic unit (or monomer) of DNA and is composed of a deoxyribose sugar linked via ester bonding to a phosphate group, and via glycosidic bonding to one of four nucleobases (a.k.a nitrogenous bases or nucleic bases): adenine (A), thymine (T), cytosine (C), and guanine (G). The deoxyribose sugar is a single-ring 5-Carbon sugar as depicted in Figure 3.1-b. The positions of the carbon atoms in the deoxyribose are numbered $1'$ (1-prime) to $5'$ (5-prime) (the carbon atoms are named C$1'$ to C$5'$ respectively) clockwise in accordance with organic chemistry naming conventions. A DNA strand is a polymer chain of nucleotides linked together between the $3'$ position of one nucleotide (specifically, the OH of the deoxyribose sugar) and the $5'$ position of another (specifically, the $O^-$ of the phosphate group). This chain of deoxyribose and phosphate molecules held by strong phosphodiester bonds form the sugar-phosphate backbone of the DNA strand (see Figure 3.2-a).

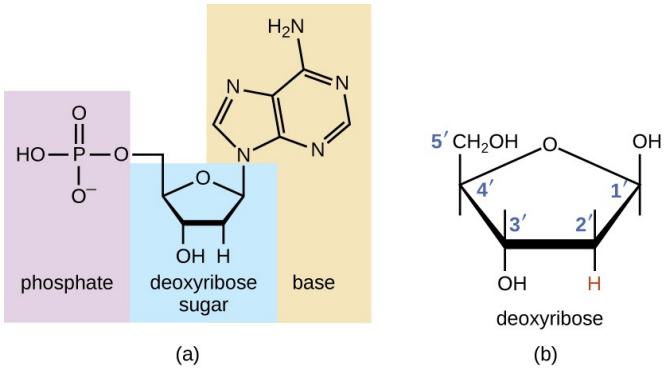


Figure 3.1 (a) A nucleotide composing of a phosphate, a deoxyribose sugar and a nitrogenous base (b) A deoxyribose sugar with the numbered positions of the C-atoms. Figure source: [3].

A double-stranded DNA molecule is made of two antiparallel DNA strands (denoted by the opposing $3'$ and $5'$ ends in Figure 3.2-c), joined together by various weak non-covalent bonds, but most notably by hydrogen bonds between opposing nucleobases (or base pairs; bp). The hydrogen bonding between the base pairs is selective in that only A-T and C-G pairings are formed (see Figure 3.2-b). In the case of a damaged single DNA strand, this selectivity permits the use of the undamaged strand as a template for repair. The two strands of DNA are arranged in a double helix configuration. In this form of the DNA molecule, carbon atoms in the $1'$ to $3'$ positions are generally more difficult for chemical species to reach and interact with because they are hidden in the minor and major grooves of the double helix as depicted in Figure 3.2-a.

In contrast, C4′ and C5′ atoms, positioned on the surface of the DNA, are relatively easier to react with given their topological accessibility [40].

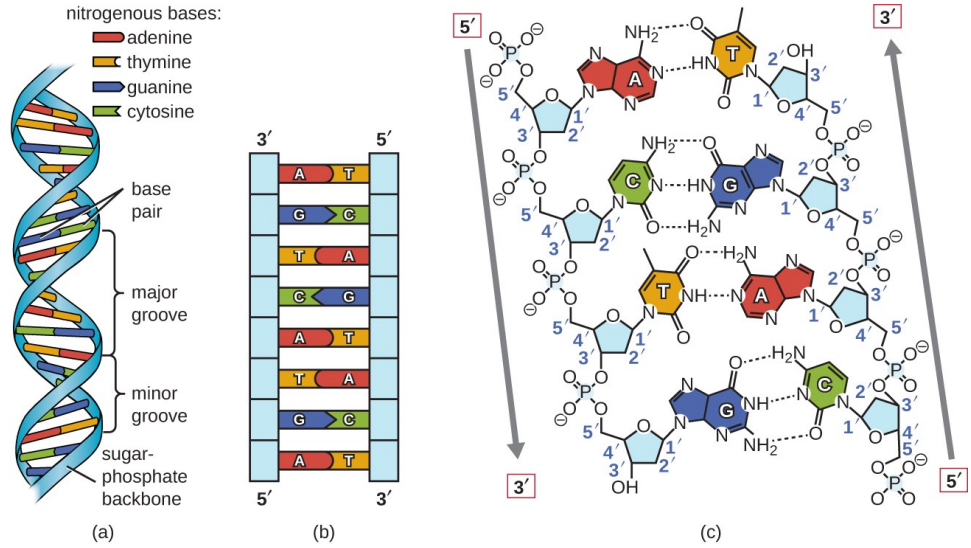


Figure 3.2 Different representations of the DNA molecule. (a) Different parts of the DNA double-helix. (b) Block representation of the DNA (rectangles: segments of the sugar-phosphate backbone, various other shapes: the different nucleobases A-T-C-G) showing the 3′ to 5′ strand and the 5′ to 3′ strand. (c) Atomistic representation of four base pairs of the DNA. The carbon atoms in the deoxyribose molecules of the sugar-phosphate backbone are labeled accordingly. Figure source: [3].

### 3.1.2 Higher-order structures

The iconic DNA double helix wraps around stabilizing histone proteins to form nucleosome structures. Nucleosomes may then link together and be condensed into chromatin fibres that further arrange compactly into chromosomes. For human somatic cells (i.e., all cells except sperm and egg cells) that are preparing for cell division (or mitosis), the chromosomes are replicated to produce two sister chromatids joined together by a centromere. An approximate total of 3.1 Gbp distributed unequally into 24 chromosomes constitutes the human genome according to the Human Genome Project [41]. Post-replication and just prior to mitosis, the number of base pairs in a human somatic cell is about 6.2 Gbp [42].

### 3.1.3 Genes and mutations

Genes are specific sequences of DNA base pairs that contain genetic information to produce specific proteins that are functionally implicated in different biological systems. Genes are first read and transcribed into a single-stranded polymer of nucleotides known as a messenger ribonucleic acid (mRNA). The mRNA molecule then exits the cellular nucleus so it can be read by ribosomes (located right outside of the nucleus) in increments of 3 base pairs (a.k.a. codons) that correspond to specific protein-building units known as amino acids. The necessary amino acids are collected and assembled to create the gene-encoded protein. The principle of producing RNA from DNA and proteins from RNA are core tenets of the central dogma of molecular biology [43]. It reasonably follows that DNA modifications in genes may induce various effects on biological functions. Although the vast majority (estimated to be >98% [44]) of the DNA in the human genome is non-coding (i.e., does not encode protein sequences), it does not mean that non-coding DNA serves no purpose as they contain information governing processes such as gene regulation and DNA packaging [45].

#### Types of genetic mutation

Genetic mutations are modifications in the DNA sequence that may be passed down to daughter cells and even offspring in the case of complex organisms [46]. These molecular changes arise from DNA damage and from random errors in DNA replication and repair mechanisms, and may be most simply classified as (i) base substitutions, (ii) insertions, or (iii) deletions. A base substitution is simply the replacement of one nucleobase for another during DNA replication. Deletion is the removal of one or more base pairs from the DNA molecule, whereas insertion is the addition thereof.

#### Effects of genetic mutation

Genetic mutations may have no effect (a.k.a. neutral) or lead to a protein's loss-of-function or gain-of-function [46]. Loss-of-function mutations are generally detrimental to the organism in that they disrupt regular protein functions. On the other hand, gain-of-function mutations may be detrimental or beneficial depending on the function gained, but generally introduce irregularities in natural functions. Non-neutral genetic mutations, when they occur in germ cells, are vehicles for introducing genetic variations in populations and influence the evolution

of species over long periods of time. Although at times beneficial, mutations in somatic cells can result in detrimental biological effects such as cancer.

### 3.1.4 Naturally-occurring DNA damage

DNA damages (a.k.a. lesions) are abnormalities in the chemical structure of the DNA molecule due to physical or chemical interactions. DNA damage is not to be confused with mutations in the DNA which are persistent changes in the sequence of base pairs. As stated above, errors in DNA damage repair mechanisms is one pathway by which mutations may arise. We pay special attention to this pathway because IR increases the occurrence of such errors via overwhelming amounts of damage inflicted to the DNA molecule.

#### Sources of natural damage

Natural damage to DNA occurs primarily from metabolic or hydrolytic processes [47]. Endogenous processes such as oxidative metabolism generate a large number of reactive chemical species such as free radicals (compounds with an unpaired electron), reactive oxygen species (ROS), reactive nitrogen species (RNS), and reactive carbonyl species (RCS) that may react with DNA constituent molecules to induce DNA damage. Among such species, hydroxyl radicals (·OH) (free radical ROS) are of particular importance due to their significantly higher reactivity and because they may be transported further via their diffusible and latent form in hydrogen peroxide ($H_2O_2$) [48]. Hydrolysis is the breaking of chemical bonds via interactions with water molecules, which happens spontaneously in cells given that water molecules constitute about 70% of the total cell mass [49]. Most spontaneous DNA damage is naturally balanced by multiple sophisticated DNA repair mechanisms that repair damaged DNA with high fidelity [50]. In other words, despite the abundance of naturally-occurring DNA damage, mutations arising from erroneous repair rarely occur. ROS have been shown to be implicated in the various processes involved in repair mechanisms and are likely released inside the cell as a stress response due to DNA damage [51].

#### Types of natural damage

The two fundamental types of DNA damage are DNA strand breaks (SBs) and base damages (BDs). A SB occurs due to the cleavage of the phosphodiester bond between adjacent segments of the sugar-phosphate backbone. If a SB is isolated on one strand of the DNA, it is referred to

as a single-strand break (SSB), whereas two SBs occurring on opposite DNA strands within 10 to 20 bp are referred to as double-strand breaks (DSBs) [52, 53]. BDs refer to a variety of damages to the nucleobases, the most common of which are apurinic/apyrimidinic sites (AP sites) and oxidized bases. An AP site is created at the location of a nucleobase that has been removed from the DNA molecule following the hydrolytic cleavage (i.e., via hydrolysis) of its glycosidic linkage with a deoxyribose. Oxidized bases, on the other hand, are simply due to the oxidation (i.e., chemical removal of an atomic electron) of nucleobases. Among such damage types, DSBs correlate best with cell killing due to their capability of inducing chromosomal aberrations lethal to the cell [54].

In humans, oxidative DNA damage is estimated to occur at around $10^4$ times per cell per day [55]. AP sites occur at approximately the same rate [56]. The occurrence rate of SSBs is also estimated to be in the order of $10^4$ per cell per day [57], whereas DSBs occur at about 50 per cell per day [58]. In contrast, the mutation rate in normal cells falls at around $10^{-10}$ mutations per nucleotide per cell per generation [50] (in the order of $10^{-1}$ per cell per day).

## 3.2 Ionizing radiation and DNA damage

### 3.2.1 Direct and indirect action

Radiation-induced DNA damage is believed to arise from two distinct processes: direct and indirect action. In direct action, ionizing particles deposit their kinetic energy directly into atoms of the DNA molecule through various interaction mechanisms, resulting in excitations and ionizations that lead to DNA damage. In indirect action, ionizing particles first interact with and dissociate intracellular water molecules in a process known as radiolysis. Through various branching physical and chemical processes, water radiolysis generates a number of reactive molecule species that are capable of chemically attacking and destabilizing nearby DNA sub-structures and can thereby induce damage. Experimental [27, 59] and theoretical [60] studies show that for low-LET radiation, approximately 65-71% of induced DNA damages can be attributed to indirect action, whereas for high-LET radiation this contribution is about 30%. Given that the focus of this thesis is on the indirect action of IR, details regarding water radiolysis are further discussed.

### 3.2.2 Water radiolysis leading to DNA damage

Water radiolysis is essentially the dissociation of water molecules into constituent particles by IR. This process can be broken down into three somewhat overlapping stages: the physical, physico-chemical, and chemical stages [9].

#### Physical stage

In the physical stage of water radiolysis, ionizing particles interact with water molecules via excitation or ionization mechanisms, which last approximately 1 fs after exposure. For incident photons, these mechanisms include the photoelectric effect, Compton scattering, and pair production (discussed in Section 2.3). For incident charged particles, Coulomb interactions take place (discussed in Section 2.2). The excitation of an $H_2O$ molecule results in an unstable $H_2O^*$ molecule. The ionization of an $H_2O$ molecule results in an unstable $H_2O^+$ cation and a free electron $e^-$. A minimum energy of approximately 7.5 eV is required for water excitation while approximately 12.6 eV is required for ionization [9]. The free electrons generated by ionization can then initiate additional excitations and ionizations of neighboring water molecules, provided they have sufficiently high kinetic energy. If they do not have sufficient energy for further interactions, they simply thermalize until equilibrium with liquid water.

#### Physico-chemical stage

The physico-chemical stage (a.k.a. intermediate stage) immediately follows after the physical stage and lasts up to approximately 1 ps. Here, the products of the physical stage ($H_2O^*$, $H_2O^+$, and $e^-$) undergo a sequence of further processes that result in the generation of various reactive molecule species. Although the complete series of events in this stage has yet to be fully characterized experimentally, the most dominant processes and resulting products (outlined shortly after) are well understood. The excited $H_2O$* molecules can either revert to ground state $H_2O$ via heat dissipation or undergo dissociative relaxation. $H_2O^*$ most commonly dissociates into a hydrogen radical H· and a hydroxyl radical ·OH. Other dissociation channels of $H_2O^*$ include the dissociation into $H_2$ and $O(^1D)$, where the latter is the singlet state of atomic oxygen, and dissociation into 2H· and $O(^3P)$, the triplet state of atomic oxygen [12]. The unstable $H_2O^+$ cations can then react with $H_2O$ molecules through a process known as protonation to produce one ·OH radical and one hydronium $H_3O^+$ cation. Aside from the processes mentioned in the physical stage, the free $e^-$ can recombine with water molecules or go through a process

known as solvation where it is enclosed by six water molecules to form a composite known as a solvated electron $e^-_{aq}$ (a.k.a. aqueous electron or hydrated electron). The majority of the products generated in the physico-chemical stage are highly reactive due to having an unpaired valence electron.

### Chemical stage

The chemical stage follows the physico-chemical stage and lasts until about 1 $\mu$s. In this stage, the products from the previous stage diffuse and interact with each other or with other nearby materials, such as DNA molecules. Table 3.1 summarizes the several dozen possible reactions in the chemical stage of irradiated pure liquid water, whereas the most important products of water radiolysis are listed in Table 3.2. The importance of these chemical species stems from either their reactivity, potential for inducing further ionizations and excitations, overall abundance, and/or diffusive capabilities.

### Radiochemical yield

Molecules involved in the chemical stage may be characterized by their radiochemical or radiolytic yield (a.k.a. G-value). The G-value of a reactive molecule $X$ is defined to be the number of species $X$ generated per 100 eV of deposited energy in a medium by a primary particle and its secondaries [9]. Mathematically, the G-value of species $X$ is expressed as:

$$G_X(t) = \frac{N_X(t) \cdot 100}{E} \tag{3.1}$$

Here, $N_X(t)$ is the number of species $X$ at time $t$, and $E$ is the absorbed energy expressed in eV. From the equation above, we see that G-value is a time-dependent measure of the production of chemical species $X$, i.e., it decreases as molecules of $X$ engage in chemical reactions and increases as molecules of $X$ are generated from other reactions. Indeed, impurities in the medium or other compounds introduced therein that may react with the radiolytically-generated molecule species serve to affect the radiochemical yield. G-value yields are typically expressed in units of molecules/100 eV.

Table 3.1 A summary of the various reactions in the chemical stage [12].

| Reactions in the chemical stage | |
|---|---|
| $H\cdot + H\cdot \rightarrow H_2$ | $H_2O_2 + e^-_{aq} \rightarrow OH^- + \cdot OH$ |
| $H\cdot + \cdot OH \rightarrow H_2O$ | $H_2O_2 + OH^- \rightarrow HO_2^- + H_2O$ |
| $H\cdot + H_2O_2 \rightarrow H_2O + \cdot OH$ | $H_2O_2 + O(^3P) \rightarrow HO_2\cdot + \cdot OH$ |
| $H\cdot + e^-_{aq} \rightarrow H_2 + OH^-$ | $H_2O_2 + O\cdot^- \rightarrow HO_2\cdot + OH^-$ |
| $H\cdot + OH^- \rightarrow H_2O + e^-_{aq}$ | $H_2 + O(^3P) \rightarrow H\cdot + \cdot OH$ |
| $H\cdot + O_2 \rightarrow HO_2\cdot$ | $H_2 + O\cdot^- \rightarrow H\cdot + OH^-$ |
| $H\cdot + HO_2\cdot \rightarrow H_2O_2$ | $e^-_{aq} + e^-_{aq} \rightarrow H_2 + 2OH^-$ |
| $H\cdot + O_2\cdot^- \rightarrow HO_2^-$ | $e^-_{aq} + H^+ \rightarrow H\cdot$ |
| $H\cdot + O(^3P) \rightarrow \cdot OH$ | $e^-_{aq} + O_2 \rightarrow O_2\cdot^-$ |
| $H\cdot + O\cdot^- \rightarrow OH^-$ | $e^-_{aq} + HO_2\cdot \rightarrow HO_2^-$ |
| $\cdot OH + \cdot OH \rightarrow H_2O_2$ | $H^+ + O_2\cdot^- \rightarrow HO_2\cdot$ |
| $\cdot OH + H_2O_2 \rightarrow HO_2\cdot + H_2O$ | $H^+ + HO_2^- \rightarrow H_2O_2$ |
| $\cdot OH + H_2 \rightarrow H\cdot + H_2O$ | $H^+ + O\cdot^- \rightarrow \cdot OH$ |
| $\cdot OH + e^-_{aq} \rightarrow OH^-$ | $OH^- + HO_2\cdot \rightarrow O_2\cdot^- + H_2O$ |
| $\cdot OH + OH^- \rightarrow O\cdot^- + H_2O$ | $OH^- + O(^3P) \rightarrow HO_2^-$ |
| $\cdot OH + HO_2\cdot \rightarrow O_2 + H_2O$ | $HO_2\cdot + O(^3P) \rightarrow O_2 + \cdot OH$ |
| $\cdot OH + O_2\cdot^- \rightarrow O_2 + OH^-$ | $HO_2\cdot + HO_2\cdot \rightarrow H_2O_2 + O_2$ |
| $\cdot OH + HO_2^- \rightarrow HO_2\cdot + OH^-$ | $HO_2\cdot + O_2\cdot^- \rightarrow HO_2^- + O_2$ |
| $\cdot OH + O(^3P) \rightarrow HO_2\cdot$ | $HO_2^- + O(^3P) \rightarrow O_2\cdot^- + \cdot OH$ |
| $\cdot OH + O\cdot^- \rightarrow HO_2^-$ | $O(^3P) + O(^3P) \rightarrow O_2$ |

Table 3.2 A list of the most important chemical products of water radiolysis [9].

| Radicals | Ions | Molecules |
|---|---|---|
| Hydrogen - $H\cdot$ | Proton - $H^+$ | Dihydrogen - $H_2$ |
| Hydroxyl - $\cdot OH$ | Hydroxide - $OH^-$ | Oxygen - $O_2$ |
| Superoxide - $O_2\cdot$ | Dioxidanide - $HO_2^-$ | Hydrogen peroxide - $H_2O_2$ |
| Hydroperoxyl - $HO_2\cdot$ | Hydronium - $H_3O^+$ | |
| Solvated electron - $e^-_{aq}$ | | |

### 3.2.3 Mechanisms of radiation-induced DNA damage

Whereas radiation-induced direct damage to the DNA is inflicted via excitation and ionization of atoms in the DNA molecule itself, indirect damage mechanisms involve chemical reactions of distinct DNA constituent molecules (a.k.a DNA moieties) with reactive products of water

radiolysis. Ionization events are more important in that there is a lack of evidence showing biologically significant damage due to excitations [61]. SBs are primarily induced in the DNA molecule by both actions through the creation of radical sites (in this case, carbon atoms with an unpaired electron) in deoxyribose sugars that may then react with oxygen through various mechanisms, resulting in the cleavage of phosphodiester bonds linking adjacent sugar-phosphate segments [62]. Radiation-induced BDs come in the form of altered nucleobases due to direct ionizations and reactions with chemical species, and AP sites similarly created due to chemical reactions and the exposure of glycosidic joints to hydrolytic processes following SB events [61]. A BD in the form of a radical site induced in a nucleobase (via direct or indirect action) may lead to a SB if the radical site transfers to the sugar-phosphate backbone [63, 64]. Given that the focus of this thesis is on indirect action, its mechanisms of damage infliction are discussed in further detail.

#### Relevance of ·OH radicals in indirect action

Experiments on the cell-killing effects of IR that investigate indirect action show that the reactive molecule that is most effective in inducing DNA damage is ·OH due to its significantly higher reactivity compared to other reactive species [27]. It is estimated in mammalian cells that about 62% of radiation-induced DNA damage is due to indirect DNA damage from ·OH radicals [65]. Mechanistic studies using dilute, aqueous solutions containing DNA, reveal that ·OH is the primary water radical responsible for inducing SSBs and DSBs, whereas BDs are due to combined effects of $e^-_{aq}$, $H^+$, and ·OH species [66, 67]. The ·OH radical has a lifetime of about 1 ns in cells due to its high reactivity [39].

#### ·OH radicals and DNA backbone moieties

The mechanism by which ·OH radicals induce SBs is via the abstraction of deoxyribose hydrogen atoms [68]. Abstraction is simply the removal of a chemical group or an atom (H-atom from C-H bonds in this case) from a molecule due to a radical attack. The abstracted H-atom binds with the attacking radical (·OH) to produce a stable compound ($H_2O$), but leaves the source molecule (deoxyribose) with an unstable radical site. As mentioned earlier, radical sites in the sugar-phosphate backbone may lead to SBs. Not only are ·OH radicals highly reactive, they are also non-selective and thus, they most likely attack the immediately accessible deoxyribose hydrogen atoms. Indeed, hydrogen atom abstraction by ·OH radicals (and by

other radical species) is believed to be dictated more by solvent accessibility than by bond dissociation energies [40]. ·OH radicals react with the various hydrogen atoms of deoxyribose molecules according to the following order of preference: C5′-H > C4′-H ≫ C3′-H ≈ C2′-H ≈ C1′-H [40, 68]. This order matches the topological accessibility of the deoxyribose atoms described in Section 3.1.1.

### ·OH radicals and DNA nucleobases

In general, double bonds (found in nucleobases as seen in Figure 3.1-a) are composed of two covalent bonds: a stronger $\sigma$-bond and a weaker $\pi$-bond. The relatively low bonding energy of C-H bonds (held together by $\sigma$-bonds) in nucleobases actually make them the primary sites of interaction for ·OH radicals (∼80% to >90% of ·OH interactions with nucleic acids) [63]. However, instead of hydrogen abstraction, the kinetically-preferred reaction at these sites is the addition reaction of ·OH radicals to nucleobase $\pi$-bonds. Although ·OH radicals are capable of directly attacking glycosidic linkages, the addition reaction of ·OH radicals with the nucleobases serve to weaken the glycosidic bond holding the base to the DNA backbone, resulting in the creation of AP sites [69]. The adducts (i.e., products of addition reactions) of ·OH radicals and nucleobases, as well as nucleobase radical sites (due to the less-preferred hydrogen abstraction by ·OH radicals from nucleobases) may induce further abstraction of H-atoms from nearby (inner) deoxyribose C-H bonds, leading to radical sites in the backbone and eventual SBs [64]. The case of radical site transfer from nucleobase to deoxyribose is via hydrogen abstraction.

### SB-induction efficiency of ·OH radicals

Given that SBs are more implicated in cell killing compared to BDs, the former are more experimentally investigated. Experimental results on the SB-induction capabilities of $^{137}$Cs radiation (low-LET domain where indirect action is dominant) on double-stranded plasmid DNA of various lengths show about a 32-44% SB yield from all ·OH radical interactions with DNA regardless of plasmid length [70]. Meanwhile, experiments on $^{60}$Co irradiation of viral single-stranded DNA places this estimate at about 14-22% [71].

### Further diffusion and mitigation of radical species

Most reactions of radical species take place within their immediate vicinity, but due to the relative stability of superoxides ($O_2^-$) and hydrogen peroxides ($H_2O_2$), they are able to diffuse

to more distant sites before chemically reacting to produce ·OH radicals that can attack other nucleic acids (DNA and RNA) and other macromolecules (carbohydrates, proteins and lipids), potentially resulting in the disruption of protective functions and alterations in structure that may lead to further biological damage [72]. DNA damage due to indirect action may be mitigated by radical scavenging whereby radical species such as ·OH react with other nearby molecules including histone proteins instead of DNA constituent molecules [61, 73]. In general, factors that can influence the presence of radical species in the cell, such as that of radical scavengers, play a part in determining the overall extent of radiation damage in biological systems.

### 3.2.4 Radiation-induced DNA damage

Similar to naturally-occurring sources of DNA damage described earlier, IR (via direct and indirect action) is capable of inducing BDs, SSBs, and DSBs. BDs are estimated to be induced by IR at >1000 lesions per cell per Gy, SSBs at approximately 1000 per Gy, and DSBs at about 20-40 per Gy [39]. What distinguishes radiation-induced DNA damage from that due to endogenous processes is the formation of DNA lesions that are in close spatial proximity with each other (a.k.a. clustered DNA damages). Such clustered damages (a.k.a. locally multiply damaged sites or LMDS [39]) rarely occur endogenously, but are relatively abundant around the trajectory of IR due to its energy deposition mechanisms (discussed in Sections 2.2 to 2.4).

Clustered lesions may be classified as either complex DSB clusters (C-DSBs) or non-DSB clusters (N-DSBs) [8, 52, 53, 74, 75]. C-DSBs are composed of at least one DSB in the vicinity of one or more other lesions, whereas N-DSBs are clusters of SSBs and BDs. The relative proportion of C-DSB cluster formation to N-DSBs has been shown to be LET-dependent [76]. Low-LET radiation is less effective in inducing C-DSBs due to its sparse ionizations and the dominance of indirect action that involves the diffusion of potentially damage-inducing chemical species to more distant sites.

## 3.3 DNA damage and mutagenesis

### 3.3.1 DNA damage response

Cells have evolved complex repair processes for dealing with damage to the genome. These damage response mechanisms involve various proteins, enzymes, and signalling pathways.

Such mechanisms are triggered by abnormalities or damages in the DNA molecule regardless of the cause (i.e., natural or not) and start on the order of a few seconds to a few minutes post-damage induction [77].

### Repair of simple lesions

For isolated simple damages (i.e., SSBs and BDs), the most preferred repair mechanism is base excision repair (BER) that is initiated when certain DNA enzymes detect the presence of an altered nitrogenous base. This damage detection process involves the rotation or "flipping" of the damaged base into a secluded active site pocket where it becomes accessible to enzymatic binding [78]. BER starts with the removal of the affected nucleobase to create a temporary AP site that is followed by the incision of the deoxyribose residue (making a SSB) to give way for the insertion of a new appropriate nucleotide [39]. AP sites and SSBs are repaired according to the appropriate step of the BER repair pathway [52]. BER is a reliable and efficient repair process that acts not only on isolated simple lesions, but also on multiple (2-10) adjacent lesions on a single DNA strand [79]. BER uses the opposite (undamaged) strand as a template to determine the missing nucleotides on the damaged strand.

### Repair of DSBs

DSBs are primarily repaired via two processes: homologous recombination repair (HRR) and non-homologous end-joining (NHEJ) [39]. HRR is a mostly error-free process but is slower [52] and requires the presence of a sister chromatid to serve as a template. In contrast, NHEJ is a faster process that does not require a repair template, but is error-prone because it simply rejoins the separated DNA double strands (each with two ends) and the wrong ends may be fused together. Due to the template requirement, HRR only occurs during the phases of the cell cycle where a sister chromatid is present (i.e., late S and G2 phases), whereas NHEJ may act in all the non-mitotic phases of the cell cycle (i.e., G1, S, and G2 phases) [39]. Due to difficulties in repairing DSBs, they are regarded as the primary culprit for radiation lethality [80].

### Repair of clustered lesions

Naturally, more structurally-complex DNA damages require more complex repair mechanisms. The repair of C-DSBs is usually via HRR and NHEJ mechanisms similar to that of DSBs. However, the additional lesions in the clusters serve to impede the repair process in terms

of speed and accuracy. As such, C-DSBs mainly lead to the deletion mutations of chains of nucleotides with lengths up to a few hundred base pairs [53, 74]. Although N-DSBs are only composed of simple damages, concurrent BER on opposing damaged DNA strands may lead to a DSB, thus the cluster may become a *de novo* C-DSB cluster [52] during the repair process. Similar to the repair of C-DSBs, the presence of other lesions in N-DSBs decelerates BER. The erroneous repair of N-DSBs, compared to that of C-DBSs, results in a more varied set of mutations that include nucleobase substitutions, insertions, and deletions.

### 3.3.2 Isolated vs. clustered DNA damage

As discussed previously, simple lesions in the DNA (even without IR) occur spatially sparsely in great numbers due to endogenously-produced reactive species capable of diffusing in space. These simple lesions are relatively easily detected and mitigated by the BER mechanism with few errors. Although IR acts to increase the overall frequency of mutation events by increasing the overall incidence of DNA lesions, it remains highly unlikely for isolated simple DNA damages to result in detrimental mutations given the repair fidelity of BER and the sheer abundance of non-coding DNA in the human genome. Instead, the prevailing theory is that radiation-induced mutagenic consequences (and subsequent carcinogenesis) stem from the erroneous repair of clustered DNA damages [52, 53, 74, 81, 82]. This belief is based on (i) the effective infliction of clustered DNA lesions by IR (relative to endogenous processes), and (ii) the error-prone repair mechanisms for such lesions.

### 3.3.3 Other mutagenic pathways

Other than direct and indirect action nuclear DNA damage, there exist several pathways by which IR may induce mutagenesis. These pathways include radiation-induced bystander effects (RIBEs) and radiation-induced genomic instability (RIGI). RIBEs are phenomena whereby irradiated cells send out signals or secrete molecules capable of inflicting cellular damage to neighboring cells such as chromosome and chromatid aberrations, mutations, and even apoptosis [39, 83]. RIGI is the case where an increased rate of genetic alterations can be found in the progeny of irradiated cells multiple generations post-exposure to IR [84]. As to which type of radiation-induced DNA damage is most likely to induce mutagenesis is still a matter of ongoing scientific debate [52, 53, 74, 81, 82]. Further, besides endogenous processes and IR, it is important to understand that mutations may also stem from exposure to pollutants, chemical

mutagens, and some viruses. However, the mechanisms by which these cytotoxic agents induce mutagenesis are beyond the scope of this thesis.

## 3.4 Mutagenesis and carcinogenesis

Tissue homeostasis depends largely on the regulated division and self-termination (apoptosis) of cells. When cell division becomes uncontrolled and/or apoptosis fails, a cell may develop into a tumor that could be benign or malignant. According to the most widespread model of carcinogenesis, the somatic mutation theory [21, 85], there are three groups of genes whose genetic alterations or mutations result in the failure of homeostatic mechanisms and eventually, carcinogenesis: (i) proto-oncogenes, (ii) tumor suppressor genes, and (iii) DNA stability genes [39]. Mutations that occur in these genes are referred to as driver mutations.

### 3.4.1 Driver mutations

Proto-oncogenes are the positive growth regulators of cells and help them achieve normal growth. When a mutation in a proto-oncogene occurs, it may become permanently activated thereby causing the cell to grow out of control. A mutation in one copy of a proto-oncogene is sufficient to achieve persistent cell growth. On the other hand, tumor suppressor genes act as negative growth regulators of cells. They control the proliferation and survival of cells by disrupting the biochemical functions of proto-oncogenes or by responding to abnormal growth signals. For loss of function to occur, both copies of tumor suppressor genes must be inactivated in most cases. Lastly, DNA stability genes are involved in the monitoring and maintenance of the DNA's structural integrity. If they become damaged, the detection of lesions and repair of damaged templates become compromised, which then leads to further mutations.

### 3.4.2 Accumulation of genetic mutations

The accumulation of gene mutations in a single cell over an extended period of time, resulting in the disruption and modification of its various regulatory mechanisms, is what eventually transforms a normal cell into a cancer cell. A significantly increased number of mutations, either induced by IR or other vectors, substantially increases the likelihood of occurrence of driver mutations that may lead to carcinogenesis. Thus, the amount of radiation delivered to the body is related to carcinogenic risk.

## 3.5 Absorbed dose and carcinogenic risk

### 3.5.1 Carcinogenic risk at high doses

Epidemiological studies on populations that were exposed to high doses of radiation have allowed us to establish our current understanding of the deterministic and carcinogenic effects of IR [86]. Data from atomic bomb survivor studies show that the incidence of cancer is linear or directly proportional to dose in the high-dose regime [39]. However, for low doses of radiation ($\lesssim$100 mSv), the associated carcinogenic risk is a subject of active research [87–89].

### 3.5.2 Carcinogenic risk at low doses

An internationally-accepted dose-response model used by the ICRP and most health agencies and nuclear regulators to determine radiation protection recommendations is the linear-non-threshold (LNT) model. The LNT model operates on two main assumptions: (i) there exists no minimum dose threshold beyond which stochastic radiobiological effects start to occur (i.e., radiobiological effects may occur regardless of how low the received dose is), and (ii) carcinogenic risk is directly proportional to the dose received [10]. The second tenet of the LNT model is an extrapolation of the linear dose-dependence of cancer incidence to the low-dose regime. While there is evidence to support other dose-response models, the LNT model offers the best overall fit for the purposes of radiation protection [90]. Under the assumptions of the LNT model, it is evident that radiation doses must be kept **a**s **l**ow **a**s **r**easonably **a**chievable (ALARA). Indeed, ALARA is the underlying principle behind the RT practice of maximizing dose to the site of malignancy while sparing healthy tissue as much as possible, although primarily in consideration of deterministic effects during RT.

## 3.6 Summary of the steps implicated in radiation-induced carcinogenesis

Figure 3.3 is a visual summary of the steps leading to carcinogenesis due to IR. In this thesis, we are particularly interested in neutron-induced carcinogenic effects due to indirect action in the context of high-energy EBRT. In this figure, the secondary spectra of neutrons (generated from photon-matter interactions) constitute the IR of interest in this thesis project that induces DNA

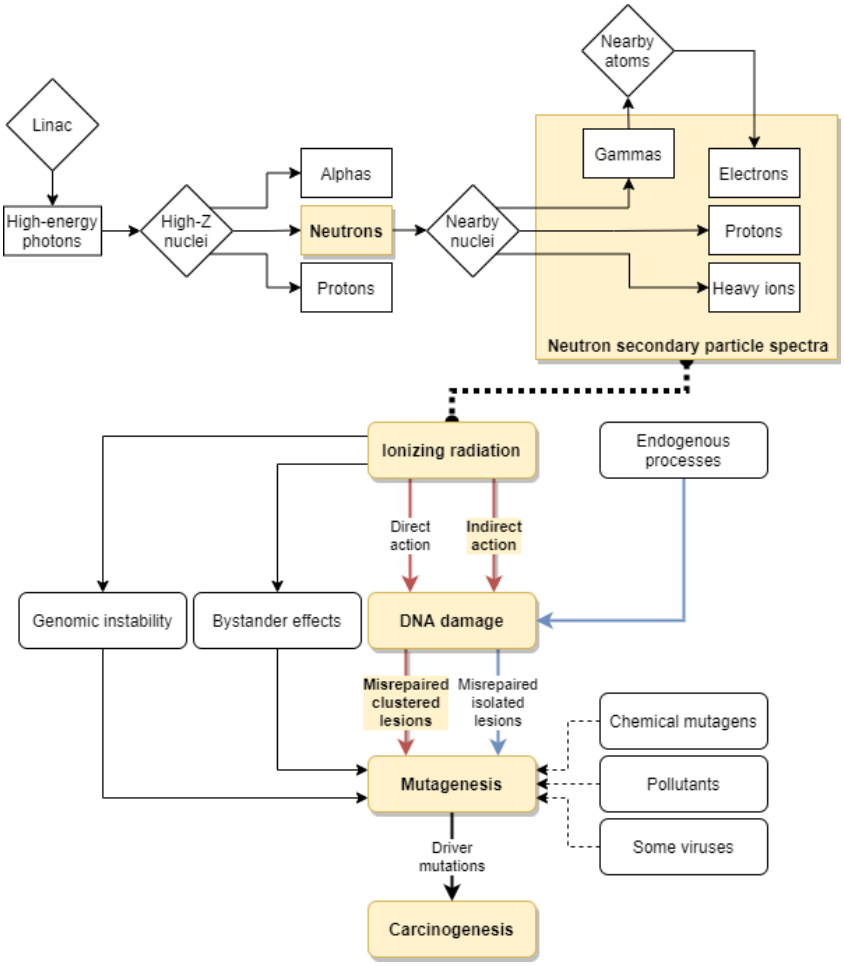


Figure 3.3 A visual summary of the processes involved in radiation-induced carcinogenesis implicating high-energy photons produced by an RT linac. The main topics of this thesis are highlighted in yellow.

damage via direct or indirect action to healthy cells of the patient. Whereas direct damages are due to ionization of DNA atoms with ionizing particles, indirect damages are predominantly due to chemical reactions of ·OH radicals with DNA moieties. Compared to endogenous processes, IR is significantly more effective at inducing clusters of DNA damages that sometimes contain DSBs. The presence of DSBs make the repair of such clusters particularly difficult, resulting in erroneous repairs in the form of mutations. Given enough time, a healthy cell may accumulate enough driver mutations causing it to develop abnormal functionalities characteristic to cancer cells, and eventually transform into one.

# Chapter 4

# Monte Carlo Simulations

Monte Carlo (MC) methods refer to a broad class of algorithms that use repeated stochastic sampling to estimate the deterministic outcomes of probabilistic events. This chapter covers the basic principles of MC methods, how they apply to the simulation of radiation transport, the various requirements for simulating DNA damage action mechanisms using them, and applicable existing software implementations.

## 4.1 Monte Carlo methods

MC methods use a random number $y$ to sample a value $x$ from a normalized probability distribution function (PDF) $f(x)$. To this end, computers are able to generate pseudorandom numbers, which are not truly random due to the deterministic nature of computers. These pseudorandom numbers are generated by random number generators (RNGs) using algorithms that emulate randomness by applying a series of operations on a starting "seed" value, such that the sequence of pseudorandom numbers generated by the given seed value appears statistically uncorrelated. Note that the same seed value always results in the same sequence of pseudorandom numbers.

The calculation of the sampled value $x$ is accomplished by first determining the cumulative probability distribution function (CPD) $F(x)$ of the normalized PDF $f(x)$ using the equation:

$$F(x) = \int_{x_{min}}^{x} f(t)dt \tag{4.1}$$

$F(x)$ is a continuous, monotonic, and increasing function inside the range [0, 1]. By evaluating the integral function and isolating $x$ from the resulting equation, the inverse function $F^{-1}(y)$ is

obtained. Finally, a pseudorandom number $y$ between [0, 1] is inserted into $F^{-1}(y)$ in order to determine the sampled quantity $x$.

## 4.2 Simulating radiation transport

MC methods are well-suited to simulating the transport of IR because particle interactions can be modelled using probability distributions. For instance, (i) the distance travelled by a particle between successive interactions, (ii) the type of interaction that occurs, (iii) the energy transferred within the interaction, and (iv) the direction and energy of the products of the interaction are all governed by PDFs. As such, pseudorandom numbers are generated as each of these situations arise while simulating associated radiation transport.

### 4.2.1 Anatomy of radiation transport simulations

#### Particles in an absorbing medium

MC simulations of physical radiation transport involve one or more initial (a.k.a. primary) particles traversing a geometric volume composed of a particular material (i.e., an absorbing medium). Given the large amount of composing atoms or molecules inside a medium and the processing required to track the motion of each one of them over some period of time, these particles are not modeled individually. Instead, the medium is considered to be a continuum. After some defined *in silico* time interval (not necessarily fixed), the most probable interaction for a traversing particle is determined from the physical cross section model of the particle and material in question.

#### Particle tracks and simulation steps

A primary particle track along with all of the subsequent (a.k.a. secondary) particle tracks it generates via simulated physical interactions constitute an event (a.k.a. history). A particle track can be discretized into smaller segments referred to as steps. Each step has both a geometric starting point and an end point (referred to respectively as the pre-step point and the post-step point) that represent two subsequent interactions separated by the time interval described earlier. Quantities such as the distance travelled (i.e., step size), direction of motion, and energy transferred are contained within each step. Particles are transported from one step point to

another via positional jumps inside the simulated space. The location of the post-step point is calculated using the velocity and direction of the particle that are assumed to be constant in the pre-step point, which results in zig-zag trajectories. The post-step point of one step is the pre-step point of the immediately succeeding step. Interactions of interest are often monitored in the simulation steps and pertinent information are recorded (a.k.a. scored). In general, only steps inside volumes of interest (a.k.a. sensitive volumes) are monitored for efficiency.

Whenever a parent particle track undergoes an interaction that results in the generation of one or more new particles, corresponding daughter particle tracks are created. These daughter tracks are pushed to a stack data structure that records the latest information about the particle such as its position, energy, direction, and type. A particle track is terminated (i.e., no longer considered as a part of the simulation) when one of the following conditions is satisfied: (i) the particle is no longer inside the defined simulation environment (a.k.a. world), (ii) the particle undergoes an interaction where it becomes dissociated or combined with another particle (as is the case with simulated molecule species discussed in Section 4.4.1), (iii) the particle's energy falls below a minimum or cutoff threshold and is thus considered absorbed by the medium, or (iv) the particle track is artificially terminated by the user.

#### Simulation runs

A simulation run is a collection of one or more simulation events. If provided with different seed values, no two runs will proceed identically due to the pseudorandomness associated with each simulation step. However, a particular run can be repeated by using the same seed value, which has a variety of practical uses including debugging.

### 4.2.2 Condensed-history simulations

The simulation of neutral particles such as neutrons and photons is computationally undemanding because the mean step size between interactions for uncharged particles usually falls around the same order of magnitude as the simulation world [91]. In contrast, for charged particles, the mean step size is often significantly smaller than the simulation environment due to multiple soft Coulomb collisions between the incident particle and the medium. Thus, the computational burden and simulation time associated with charged particle transport is higher than neutral particle transport in the same geometric volume.

To mitigate this issue, multiple small soft collisions that are relatively close to each other can be approximated as one larger "condensed-history" step [92]. Such approximations are valid since soft collisions often only involve slight angular deviations with minimal energy transfer. However, in order for condensed-history steps to retain sufficient transport accuracy and offer meaningful improvement in processing time, multiple scattering models must be carefully designed.

### 4.2.3 Parallel processing

Additional improvement in simulation efficiency can be achieved by distributing event simulations across a number of available CPU threads for parallel computation in a process known as multithreading. In most implementations of multithreading, the main thread where a simulation run was initiated acts as a manager thread that assigns simulation events to unused CPU threads (a.k.a. worker threads). Once a worker thread has completed simulating its assigned event, the results are absorbed into the main thread, which keeps track of scored values such as DNA damage from all events. Furthermore, if the simulation framework offers GPU support, the simulation may be loaded into the computer's GPU (hardware specifically designed for repetitive parallel computations such as graphics rendering) instead of the CPU for significantly faster computation [93].

## 4.3 Simulating DNA damage

In order for MC simulations of radiation transport to be meaningful in the context of estimating RBE, a biological endpoint must be established. As previously mentioned in the project objectives, the biological endpoint considered in this thesis project was neutron-induced yields of clustered DNA damage in a geometric DNA model.

### 4.3.1 Geometric DNA models

In practice, geometric DNA models are complex structures composed of basic nanoscopic-scale volumes that are arranged in the structure of the DNA double-helix. Most DNA models that have been developed to date are composed of liquid water (sometimes with varying densities), which act as surrogates for biological macro-molecules [94]. Published DNA models vary in

terms of resolution and sophistication [15, 95, 96]. Some models represent multiple base pairs of the DNA as one cylindrical volume, whereas others represent individual atoms in the DNA. The appropriate scale depends on the nature of the problem being researched. In the case of explicit simulation of SBs and BDs, it suffices to have dedicated volumes representing whole segments of the sugar-phosphate backbone and separate ones for whole nucleobases [15].

A DNA model may include additional structures such as histone proteins or hydration shells that envelope the DNA base pair volumes. Higher-order genetic targets such as plasmids, bacterial DNA, or a full nucleus of a human fibroblast cell can be constructed using appropriate arrangements of replicated DNA volumes. Moreover, by containing such structures inside a liquid water volume, a model for a full bacterial cell (containing bacterial DNA and/or plasmids) or a full human fibroblast cell can be achieved. Human fibroblast cells are frequently modeled in radiation simulations because they are proliferating cells, not overly specialized in form and function (unlike red blood cells and neurons), and present all over the human body.

### 4.3.2 Track-structure simulations

The accurate simulation of DNA damage and other biological effects requires the ability to accurately track the position of ionizing particles at the cellular ($\mu$m) and subcellular (nm) scale. Since condensed-history techniques are necessarily associated with a loss of positional accuracy, they cannot be used when tracking charged particles in the vicinity of DNA constituent structures. Instead, track-structure MC codes are used to explicitly simulate all particle interactions in the vicinity of DNA. Furthermore, particles must be tracked to the minimum energy where ionizations and excitations might still occur, which is approximately 7.5 eV in liquid water as described in Section 3.2.2.

### 4.3.3 Simulating direct action

At this point, we have all the information we need to understand how direct action may be simulated. Similar to the mechanisms of direct action in an actual DNA molecule, simulated direct action involves localized energy depositions onto volumes representing either sugar-phosphate segments or nitrogenous bases. We know that parameters such as particle type, energy deposition, and location are encapsulated in each step of a radiation transport MC simulation. Since each step of a simulation is monitored to assess how subsequent steps are to proceed, it is possible to determine whether or not a direct action hit occurs during each step.

This is accomplished by first checking if the step is inside a DNA volume of interest (backbone or base in the case of volumetric models) and then verifying whether the energy deposition within the step exceeds a user-defined threshold that corresponds to the minimum amount of energy required to induce a lesion (SB or BD). Alternatively, direct damage may be modeled using a damage probability that is linear with the step energy deposition for some specified energy range. Simulating indirect action requires further steps that are discussed below.

## 4.4 Simulating water radiolysis

Before indirect action may be simulated, the processes leading to it (i.e., the interactions involved in the different stages of water radiolysis) must first be simulated.

### 4.4.1 Simulation of physical and chemical interactions

So far, the previous sections of this chapter have focused mostly on discussing the simulation of physical interactions and transport of ionizing particles inside a medium and only considered the physical products of such interactions. For instance, to simulate a proton traversing a water medium, we only need to consider the secondary electrons produced by proton-water ionization interactions. To simulate water radiolysis, however, the reactive molecule products generated by these interactions must also be taken into consideration. The simulation of chemical transport is similar to the transport of IR in that chemical processes are also governed by probabilities.

Simulated physical tracks represent particles (IR) that travel in zig-zag paths as they undergo physical processes inside the medium. On the other hand, simulated chemical tracks represent molecule species propagating via Brownian motion that may enter into a chemical reaction with the molecules of the medium or with other simulated species. As mentioned in Section 4.2.1, the individual particles composing a medium are not explicitly simulated. In the case of a water medium, the water molecules with which physical and chemical species might interact are assumed to be static and in their ground states. In contrast, water molecules at different excited states (and all other reactive species) are tracked separately given that there are differences in their possible reaction pathways.

### 4.4.2 Simulation parameters of water radiolysis

Physical particles may be defined by properties such as mass, charge, and spin. Chemical species can be defined by their mass too but also by parameters such as number of electrons and atoms. The simulation of chemical tracks further differs from that of physical tracks in that the former are governed by parameters such as (i) molecule radius, (ii) electronic configurations, (iii) decay tables, and (iv) diffusion coefficients of molecules [16]. A molecule's radius incorporates its van der Waals radius to spatially determine whether it enters an interaction with world geometries upon volume intersections. Indeed, the electronic configuration determines whether a molecule is in ground state, excited, or ionized. If the molecule is excited or ionized, it follows the predefined dissociating schemes in its decay table. Each of these pathways has an associated probabilistic branching ratio that dictates which pathway is most likely to be processed. Finally, the diffusion coefficient dictates the rate at which a molecule propagates inside the medium.

To simulate the interactions between chemical species, the additional parameter of reaction rate constant is defined for each chemical reaction. This temperature-dependent parameter is implicated in the calculation of the reaction radius between two reactive molecule species. During a simulation step, if the distance between two chemical species with a defined reaction falls under their calculated reaction radius, the reaction is considered to occur. The simulation's time-step resolution also plays a role in determining the incidence of chemical reactions. If the time interval of steps is too high, molecules that would have reacted together would instead "jump through" each other without interacting as they are jump-transported to their calculated post-step positions [97]. Setting the time-step resolution too low causes the simulation to take significantly longer without much benefit in accuracy, thus a good balance between simulation duration and accuracy must be sought.

### 4.4.3 Simulation validation

An important metric that gives credence to the accuracy of water radiolysis simulations is the G-value (discussed in Section 3.2.2). There are several experimental data in the literature for the time-dependent G-values of various species generated via water radiolysis [98–114]. The accuracy of existing MC implementations of water radiolysis have been validated against these experimental values. The closer the the time-dependent G-values are of simulated species to experimental values for a wide range of LET values, the greater the confidence in the simulation.

If the G-values of simulated species are inconsistent with experimental data, this likely results in inaccurate counts of DNA damage yields (DYs) due to indirect action.

## 4.5 Existing implementations

For optimal simulations of irradiated DNA models, we ideally want a combination of condensed-history and track-structure simulations. The transport of IR from the particle source towards sensitive volumes is to be handled by the more computationally-efficient condensed-history techniques. Once particles are close enough to constituent volumes of the DNA model, their transport is to be handled by the more accurate track-structure techniques. With this combination, we are able to accelerate the simulations as much as possible without significant loss in accuracy. Moreover, if we want to incorporate indirect action, we need to be able to simulate the physico-chemical and chemical interactions of water radiolysis.

### 4.5.1 Existing available MC codes

There exist multiple condensed-history MC-based codes and toolkits to simulate radiation transport such as PHITS [115], FLUKA [116], EGS [117], PENELOPE [118], and Geant4 [119]. Each has its own available set of particles that can be simulated at various energy levels [120]. Similarly, there are various implementations of track-structure MC codes developed specifically for radiobiology including PITS [121], PARTRAC [122], KURBUC [123], NOREC [124], PTra [125], TRAX [126], RITRACKS [127], and Geant4-DNA [128].

Despite the number of existing simulation codes, there are several issues at hand that must be considered when selecting one. Firstly, combining any one of the condensed-history codes with any one of the track-structure codes may not be a seamless process due to differences in programming language and overall software architecture. Secondly, not all track-structure implementations readily include code to simulate water radiolysis. Lastly, only a few of these codes are publicly accessible. The pair that was most suitable for use in this thesis project is Geant4 and its low-energy extension, Geant4-DNA.

### 4.5.2 Geant4

Geant4 (**Ge**ometry **an**d **T**racking version **4**) is an open-source condensed-history MC code developed and maintained by the international Geant4 Collaboration. Geant4 uses the object-

oriented programming language C++. This toolkit is used in a wide variety of fields such as high-energy physics and astrophysics, space science, and medical physics because of the variety of physics models it provides [119] capable of handling a wide range of energies (keV to PeV) for multiple particles [15, 129]. Physics models are simply a collection of energy-dependent cross section data or theoretical functions defined for different particle-matter interactions.

One important feature of Geant4 is that it allows users to construct their own simulation scenarios. For a minimal valid simulation scenario, a user needs to define the following simulation components via custom C++ classes: (i) the geometric structure(s) to be irradiated with their corresponding positions and materials, (ii) the source of particle radiation, and (iii) the physics constructor to be used that compiles the required particles, processes, and cross section models. Further, users can define one or more custom scorers that can record various information about the simulation when user-defined conditions are met. Other useful features of the Geant4 toolkit include real-time visualization and multithreading support [119].

#### Geant4-DNA

What makes Geant4 the most suitable MC code for this thesis is its low-energy extension Geant4-DNA developed and maintained by the Geant4-DNA Collaboration [128]. Geant4-DNA comes as part of the Geant4 10.1 release and includes code for radiochemistry simulations. This extension includes physics constructors for low-energy detailed transport (i.e., track-structure simulation) of electrons, protons, and alpha particles [130]. Moreover, Geant4-DNA includes molecule classes and chemistry constructors and accompanying models for the various chemical species and reactions involved in the different stages of water radiolysis that incorporate the parameters discussed in Section 4.4.2 [15, 16]. As such, it allows for the simulation of the generation of reactive species, their diffusion via Brownian motion (random change in direction after each time step [16]), and their various chemical reactions up to the completion of the chemical stage. Furthermore, Geant4-DNA comes with a collection of biological structures readily implemented as geometric volumes that can be included in simulations [15].

Being an extension of Geant4, Geant4-DNA uses practically the same framework. Although this allows for a seamless integration of the features exclusive to each of them, this also means that using Geant4-DNA comes with the same drawbacks as using Geant4. These drawbacks come in the form of various prerequisites for the users including familiarity with Geant4-specific commands and its various classes, functions, and processes, and development proficiency with the C++ language. However, there are accessible frameworks to mitigate these drawbacks.

### 4.5.3 TOPAS

The TOPAS (**To**ol for **Pa**rticle **S**imulation) software project developed by Perl *et al.* (2012) [131] rectifies most of the difficulties associated with using Geant4. TOPAS is essentially an extension to Geant4 that acts as a front-end wrapper to render the latter toolkit more user-friendly and less error-prone by providing a simpler user interface. With TOPAS, the user has access to all the features offered by Geant4 without necessarily having to deal with the drawbacks such as the C++ development overhead. Indeed, the intention for the development of TOPAS was to make MC simulations, in the form of Geant4, more accessible to clinical medical physicists and researchers who may not be familiar with C++ or the many features of Geant4.

```
# Geometric structures
d:Ge/World/HLX= 50 nm # HL = half length
d:Ge/World/HLY= Ge/World/HLX mm
d:Ge/World/HLZ= Ge/World/HLX mm
s:Ge/World/Material = "Vacuum"
b:Ge/World/Invisible = "True"

s:Ge/MyTarget/Parent = "World"
s:Ge/MyTarget/Parent = "TsSphere"
s:Ge/MyTarget/Parent = "G4_WATER"
d:Ge/MyTarget/RMax = 35 nm
s:Ge/MyTarget/Color = "white"
```

```
# Particle source
s:So/MySource/Type = "Beam"
d:So/MySource/BeamEnergy = 10. MeV
u:So/MySource/BeamEnergySpread = 0
s:So/MySource/BeamParticle = "proton"
i:So/MySource/NumberOfHistoriesInRun = 10

# Physics and chemistry constructors
sv:Ph/Default/Modules = 2 "g4em-dna_opt2and4" "TsEmDNAChemistry"
s:Ch/ChemistryName = "TOPASChemistry"
b:Ch/TOPASChemistry/ChemicalStageTransportActive = "True"
d:Ch/TOPASChemistry/ChemicalStageTimeEnd         = 1. ns
dv:Ch/TOPASChemistry/AddTimeStepHighEdge       = 1 999999 ps
dv:Ch/TOPASChemistry/AddTimeStepResolution     = 1 0.5 ps
```

Figure 4.1 Example of a TOPAS parameter text file with the minimum required parameters for a simulation: geometric structures, irradiating particle source, and physics constructor. The chemistry constructor and its settings are optional for a particle irradiation simulation.

To run simulations, TOPAS users need to define the same parameters required by Geant4, albeit in a more user-friendly fashion (i.e., without the need to define custom C++ classes) through the use of an easily-readable text-based parameter file as shown in Figure 4.1. TOPAS offers a wide variety of predefined geometric structures, complex particle sources, scorers, and additional physics constructors and models that the user can easily reference and configure in the parameter file. Users may also reference any other predefined simulation elements and options provided by TOPAS such as electromagnetic fields, timing features, and output formats. The order of the parameters and their corresponding specifications do not matter in the TOPAS parameter file unlike the way source and macro files are prepared in Geant4, which is another potential vector of error that TOPAS eliminates.

If a user needs a structure, a particle source, a physics constructor, and/or a scorer that is currently not available in TOPAS, the necessary custom classes (or extensions in the context of

TOPAS) can be built via the TOPAS extensions framework [132]. However, the development of extensions in this manner requires knowledge of C++ and familiarity with Geant4 functions. Fortunately, the TOPAS extensions framework comes with plenty of helper functions that can facilitate the development of these extensions.

### TOPAS-nBio

Table 4.1 A list of the chemical species available for simulation in TOPAS-nBio and Geant4-DNA [13].

| Chemical species | Name in TOPAS-nBio | In Geant4-DNA? |
|---|---|---|
| $e^-_{aq}$ | SolvatedElectron | ✓ |
| ·OH | Hydroxyl | ✓ |
| H· | Hydrogen | ✓ |
| $H_3O^+$ | Hydronium | ✓ |
| $H_2$ | Dihydrogen | ✓ |
| $OH^-$ | Hydroxide | ✓ |
| $H_2O_2$ | HydrogenPeroxide | ✓ |
| $O_2$ | Oxygen | — |
| $O^-_2$ | SuperoxideAnion | — |
| $HO_2$ | HydroPeroxide | — |
| $HO^-_2$ | Dioxidanide | — |

One of such TOPAS extensions is TOPAS-nBio which is analogous to what Geant4-DNA is to Geant4. TOPAS-nBio was designed to wrap and extend the track-structure and radiation chemistry features of Geant4-DNA [133]. Similar to Geant4-DNA, the radiochemical yield of chemistry models available in TOPAS-nBio are consistent with various experimental data [13, 133]. The TOPAS-nBio extension also comes with not only a greater variety of biological structures available such as chromatin fibre models that can be used to assess radiation-induced DNA damage, but also a greater variety of chemical species as listed in Table 4.1. Various additional parameters that may be modified via the parameter file system include the reaction rates in the chemistry constructor, energy cutoffs, and the time resolution of the simulation (as seen in Figure 4.1). The latest release (version 1.0, released in May 2021) [134] even includes a full DNA and cell model, a damage scorer for direct and indirect action, as well as models for DNA repair: DaMaRiS (**D**NA **M**echa**n**istic **R**epa**i**r **S**imulator) [135] and MEDRAS (**Me**chanistic **D**NA **R**epair **a**nd **S**urvival model) [136].

## 4.6 Simulating indirect action

Using TOPAS and TOPAS-nBio, we get to easily set up a simulation scenario where a DNA model enclosed in a water medium is irradiated by ionizing particles. These particles travel from their source to designated sensitive volumes via condensed-history simulations, and then towards DNA constituent volumes using track-structure simulations. The physical and physico-chemical interactions between the incident particles and the medium are processed to generate secondary ionizing particles and reactive chemical species, then the interactions between the latter species to produce other reactive species. All these simulated chemical species may then diffuse and enter into contact with DNA volumes to simulate indirect action.

### 4.6.1 Simulation parameters of indirect action

As discussed in Section 3.2.3, indirect action involves a multitude of interactions (with varying complexity of mechanisms, some of which are more understood than others) between various chemical species and DNA moieties that is currently impractical to model atomistically. Unlike damage due to direct action (a.k.a. direct damage) that may be modeled by energy depositions exceeding a certain threshold at certain DNA volumes, damage due to indirect action (a.k.a. indirect damage) involves numerous other design choices. Ideally, we want a model complexity that optimizes computation speed and accuracy.

The simulation parameters of indirect action are essentially the quantities that define what an indirect action event is, including the rates of interaction and damage induction between explicitly simulated reactive molecule species and constituent volumes of the geometric DNA model. The model complexity of indirect action is reflected on the kinds of interactions that are considered to induce DNA damage. The more of such interactions are considered, the more complex the indirect action model becomes. Given the significantly higher reactivity of ·OH radicals compared to the rest of the reactive species, only ·OH radical interactions with DNA backbone segments were historically considered to induce SBs at varying damage probabilities as shown in Table 4.2. The model of indirect action (i.e., the nature of *in silico* events defined to be capable of inducing indirect damage) dictates the resulting yield of indirect DNA damage in each run, thus the slightest differences in implementations and simulation scenarios (i.e., DNA model, physics and chemistry modules, chemical stage duration, incident particle type and energy, etc.) may yield significant differences in DNA damage counts.

Table 4.2 A summary of previous simulation studies with indirect action implementation using various simulation codes, physics and chemistry constructors, chemical stage duration ($T_{chem}$), and ·OH damage probability with the DNA backbone ($P_{\cdot OH}^{backbone}$).

| Reference | Code | Physics constructor | Chemistry constructor | $T_{chem}$ | $P_{\cdot OH}^{backbone}$ |
|---|---|---|---|---|---|
| Nikjoo (2001) [137] | PITS | — | — | 1 ns | 0.13[b] |
| Friedland (2003) [138] | PARTRAC | — | — | 10 ns | 0.13[b] |
| Friedland (2011) [139] | PARTRAC | — | — | 2.5 ns | 0.65 |
| Friedland (2017) [140] | PARTRAC | — | — | 100 ns | 0.65 |
| Meylan (2017) [141] | Geant4-DNA | Default | Default | 2.5 ns | 0.4 |
| Lampe (2018) [142] | Geant4-DNA | Opt4 | Default | 1 ns | 0.4 |
| Mokari (2018) [143] | Geant4-DNA | Default | Default | 1 ns | 0.65 |
| Rosales (2018) [4] | Geant4-DNA | Default | Default | 1 ns | 0.65 |
| Sakata (2020) [144] | Geant4-DNA | Opt2, Opt4 | Default | 5 ns | 0.405 |
| Zhu (2020) [30] | TOPAS-nBio | Default[a] | Default[a] | 1 ns | 0.4 |

[a]The default constructors of TOPAS-nBio are not the same as those of Geant4-DNA.
[b]Defined for ·OH interactions with the whole DNA volume.

### 4.6.2 Factors affecting indirect damage yields

Besides how indirect damage is defined, many other simulation parameters and factors affect indirect DYs. As expected, the physics and chemistry constructors of the simulation influence indirect DYs in that they determine which particle and molecule species are simulated and at what quantities. For chemistry constructors specifically, increasing the reaction rates of defined chemical reactions that generate potentially-damaging species increases the number of species capable of inducing indirect damage, thus resulting in higher incidence of indirect damage events. Note also that DYs strictly increase over time (given there is no DNA repair model implemented). Thus, increasing the duration of the chemical stage ($T_{chem}$) only increases the number of damage events. In general, factors that affect the number of damage-inflicting species present in the simulation world influence indirect DNA DYs.

Factors that can negatively affect indirect DYs include track-terminating conditions defined for the simulation world that serve to make the simulations more realistic or computationally more efficient. For instance, previous work simulating indirect action terminate all chemical species generated inside (and certain species diffusing into) histone and DNA volumes [30, 138], which decreases overall yields of species. Some work implement a radical kill radius, a distance

from the DNA model beyond which molecule tracks are terminated [142, 144], which limits the amount of potentially-damaging species that reach vulnerable sites. Moreover, increasing the tracking cutoff energy of particles and molecules will cause them to be terminated prematurely and thus, decrease their likelihood of inducing damage events. Finally, an implemented repair mechanism serves its purpose of reducing simulated DYs (direct or indirect).

### 4.6.3 Previous work on indirect damage simulations

Despite differences in the implementations of indirect action and other simulation components (cell model, radiation source and energy range, damage types considered, etc.) performed by different groups, SBs due to indirect action are consistently shown to occur significantly more frequently (decreases with increasing LET from 0 to 100 keV/$\mu$m) than SBs due to direct action [145, 142, 144]. As discussed in Section 3.3.1, isolated lesions are much easier to repair, thus indirect action being able to induce much more SBs than direct action does not necessarily mean it would be more effective in causing mutagenic consequences.

For studies on proton and alpha irradiation that present a breakdown of the causes of DSBs (direct, indirect, or hybrid), two important results emerge: (i) DSBs due to indirect action occur in significantly greater numbers than DSBs due to direct action for lower-LET radiation, and (ii) hybrid (a.k.a. mixed) DSBs (having both a direct and an indirect SB) make up a significant portion of all counted DSBs [4, 30] as can be seen in Figure 4.2. Zhao *et al.* (2020) [31] even reported that hybrid DSBs constitute more than half of all DSBs produced in their simulations of proton and photon irradiation. These findings are consistent with data showing indirect action to be more effective than direct action in inducing mammalian cell inactivation in the low-LET domain while still significantly affecting in the high-LET domain [29].

From the results of the aforementioned *in silico* experiments, we know that including the mechanisms of indirect action in simulations of cell irradiation significantly increases the overall number of DSBs. Even though these studies did not look into clustered lesions, it makes logical sense that the number of C-DSBs (which require the presence of at least one DSB in close proximity to simple lesions) only increase with an increased overall DSB count. Indeed, Henthorn *et al.* (2019) [146], looking into C-DSB cluster yields of photons and protons, report that including indirect action in their simulations yielded increased counts of complex breaks. Thus, it is important to incorporate indirect action in irradiation simulations.

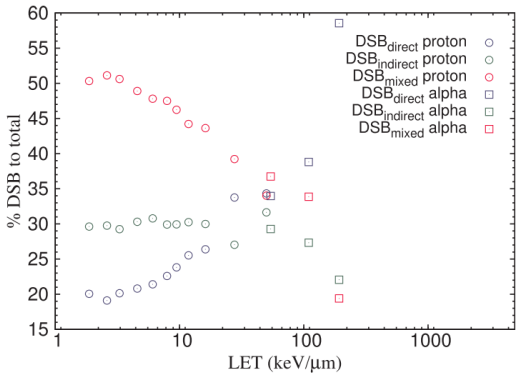


Figure 4.2 DSB contributions per damage cause from the simulations of de la Fuente Rosales *et al.* (2018) [4] using primary protons and alpha particles.

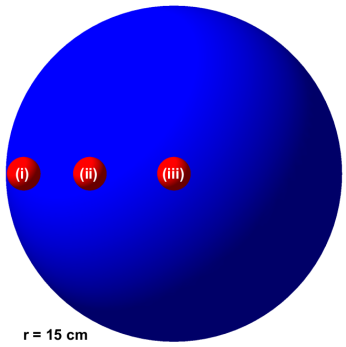


Figure 4.3 ICRU sphere [5] of soft-tissue phantom with various scoring volumes: (i) outer, (ii) intermediate, and (iii) inner. Figure from L. Montgomery [2] with permission.

## 4.7 Previous work on neutron RBE using MC simulations

### 4.7.1 Energy dependence of neutron RBE

An important work upon which the foundational aspects of this thesis is motivated is that of Baiocco *et al.* (2016) [6], who demonstrated, *in silico*, the energy dependence of neutron RBE for stochastic effects. Their study was part of the international ANDANTE project [147, 148] whose objectives revolved around the assessment of neutron RBE using various methods such as MC simulations, radiobiological experiments with stem cells, and epidemiological studies of neutron-induced second malignancies due to proton therapy treatments. Baiocco *et al.* (2016) [6] used the condensed-history MC code PHITS to determine the secondary particle spectra of primary neutrons (with energies ranging from 10 eV to 1 GeV) and of reference X-rays (220 keV) generated at different scoring volumes (with radial depths of 1.5 cm, 7.5 cm, and 15 cm) inside an ICRU sphere (See Figure 4.3). Using these sets of neutron and X-ray secondary particle spectra, two neutron RBE models were developed.

The first model was a microdosimetric model involving the use of PHITS to estimate particle tracks having energies sampled from the previously obtained neutron secondary particle spectra. A microdosimetric quantity known as dose-mean lineal energy ($\bar{y}_D$) was calculated for all tracks associated with a given primary neutron energy and scoring volume. The same calculation was performed for the tracks of the X-ray secondary particles. The value $\bar{y}_D$ describes the spatial distribution of energy depositions of the tracks in a given set. The estimated neutron RBE

models for each scoring volume were simply the respective ratios of the $\bar{y}_D$ values calculated for each initial neutron energy ($E_0^{n^0}$) and the $\bar{y}_D$ for the reference X-rays at each scoring depth. The second model also involves the random sampling of energies from the secondary particle spectra, but instead of estimating tracks using PHITS, the track-structure MC code PARTRAC was used to explicitly simulate particle tracks to irradiate a DNA model. The neutron RBE was calculated by taking the ratio of neutron-induced DYs and X-ray-induced DYs (again, for all $E_0^{n^0}$ in each scoring volume). Specifically, these DYs were those of clusters of direct DNA damage containing at least two DSBs within 25 bp (a.k.a. DSB++ lesions [139]).

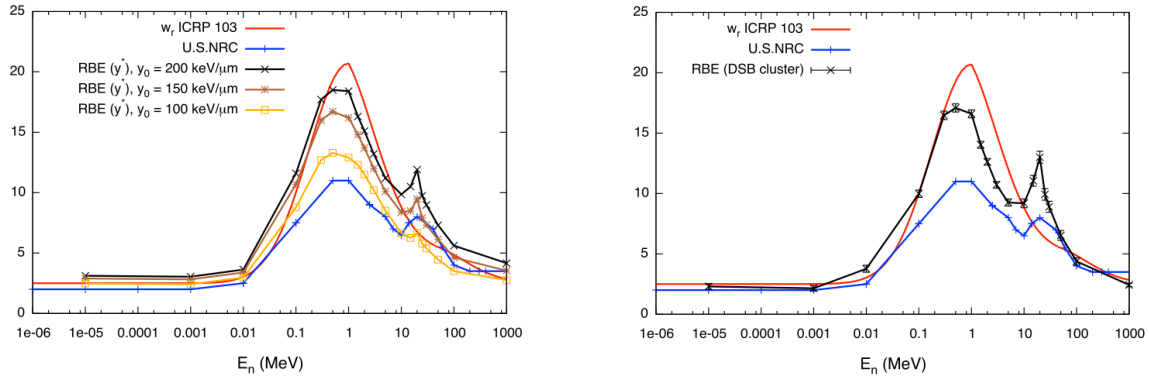


Figure 4.4 Neutron RBE models by Baiocco *et al.* (2016) [6] for the outer scoring volume. (a) Model 1: microdosimetric model of neutron RBE for different values of an empirical tuning parameter used to calculate the $\bar{y}_D$ values. (b) Model 2: neutron RBE for inducing DSB++.

The resulting neutron RBE models are particularly important in that they demonstrate a similar energy dependence as the ICRP neutron radiation weighting factors and the US NRC neutron quality factors as depicted in Figure 4.4. In other words, the work of Baiocco *et al.* (2016) [6] connected the energy dependence of real-world neutron RBE for stochastic effects to fundamental microdosimetric concepts and biophysical mechanisms (i.e., $\bar{y}_D$ and DSB++). However, despite such important results, the work of Baiocco *et al.* (2016) [6] remains challenging to replicate and expand upon to include indirect action effects due to the use of closed-source code. This difficulty specifically comes in the form of the inaccessibility of (i) the PHITS-generated neutron and X-ray secondary particle spectra and (ii) the PARTRAC DNA model used. However, these issues have been addressed and resolved by recent work by our research group [2, 7, 8] as discussed in the next sections. This thesis project aims to further expand upon our recent work by incorporating the damage contribution of indirect action.

### 4.7.2 Simulated neutron secondary particle spectra

To circumvent the issue of publicly-unavailable track data for the secondary particle spectra of different monoenergetic neutrons and reference X-rays, our group (Lund *et al.* (2020) [7]) developed a model similar to the first neutron RBE model of Baiocco *et al.* (2016) [6], but using the open-source toolkits Geant4 and Geant4-DNA. Lund *et al.* (2020) [7] performed explicit neutron particle track simulations inside an ICRU sphere and obtained the secondary particle spectra at different scoring volumes similar to the work of Baiocco *et al.* At the same time, a weighted track-sampling algorithm developed by Famulari *et al.* (2017) [149] was employed to calculate necessary $\bar{y}_D$ values. A notable feature of this algorithm is that it handles the calculation of $\bar{y}_D$ values from the nano up to the micro scale, which correspondingly allows for the assessment of neutron RBE at the scale of base pairs (nano) up to the scale of chromosomes (micro) as shown in Figure 4.5. Neutron RBEs for different $E_0^{n^0}$ values were calculated in the same manner as Baiocco *et al.* in their first model, but with 250 keV X-rays as the reference radiation instead of 220 keV X-rays.

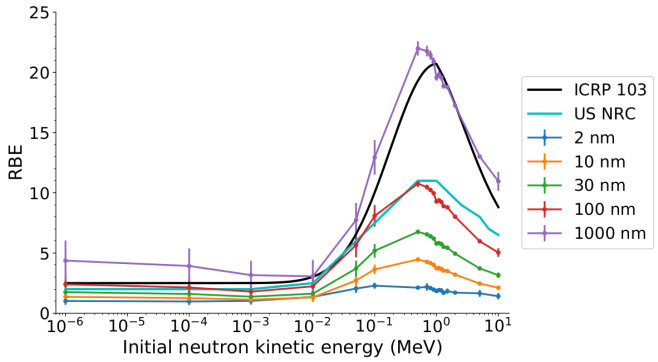


Figure 4.5 Microdosimetric neutron RBE model by Lund *et al.* (2020) [7] in the outer scoring volume using different scales by which to cluster energy depositions to calculate $\bar{y}_D$ values.

With the work of Lund *et al.* (2020) [7], our group has access to data on the secondary particle spectra of different monoenergetic neutrons and 250 keV X-rays that can be used for explicit particle track simulations with a geometric DNA model. These results contain information about what secondary particles are generated, their respective energy ranges, and their proportional contribution to the absorbed dose (relative dose) (see Figure 4.6).

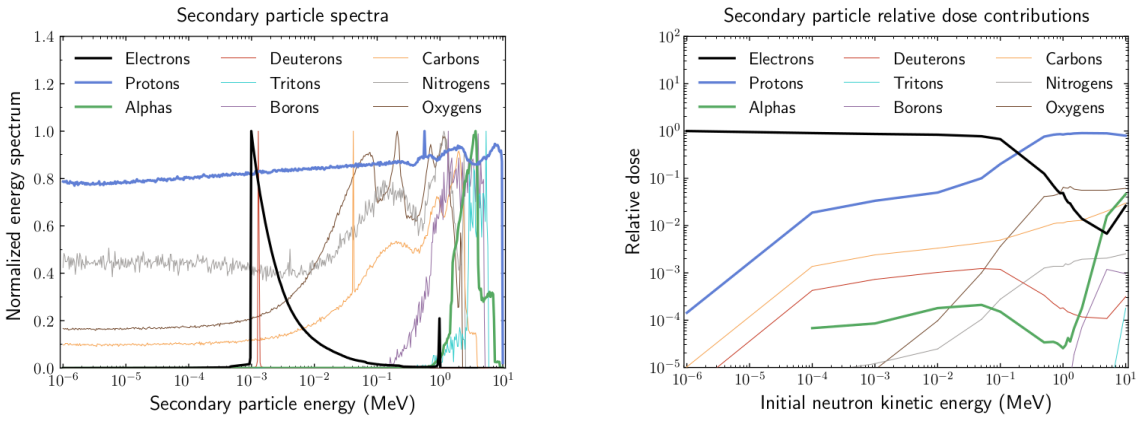


(a) (b)

Figure 4.6 An example of the results obtained by Lund *et al.* (2020) [7]. (a) Secondary particle spectra generated for 10 MeV neutrons in the intermediate scoring volume. (b) Relative dose contributions of secondary particles as a function of initial neutron energy in the intermediate scoring volume. Figures by L. Montgomery [2] using the data reported by C. M. Lund [7].

### 4.7.3 Neutron RBE for clustered direct DNA damage

Another important foundational work for this thesis project to highlight is that of Montgomery *et al.* (2021) [8] from our research group. It involved the development of an RBE model similar to the second one of Baiocco *et al.* (2016) [6]. The former work improves upon the latter in that it provides an accessible full nuclear DNA model and considers other types of clustered lesions.

The development of the full nuclear DNA model by Montgomery *et al.* (2021) [8] was inspired by the lack of available models that were complete and open-source at the time of study (despite the many publicly-unavailable models described in the literature [30, 95, 141, 142, 150]). The DNA model of Montgomery *et al.* (2021) [8] was developed using the TOPAS extensions framework and was based on the chromatin fibre model described by Villagrasa *et al.* (2017) [151] whose source code was included in the beta release of TOPAS-nBio [152]. Details regarding the geometry of the full nuclear model are described in Section 5.2.2. This nuclear DNA model is enclosed in a water sphere to represent a full human fibroblast cell. The neutron and X-ray secondary particle spectra at varying depths obtained by Lund *et al.* (2020) [7] were used by Montgomery *et al.* (2021) [8] to irradiate the cell model. Thus, it was as if the cell model was irradiated at the various scoring volumes inside the ICRU sphere by different monoenergetic neutrons and reference X-rays.

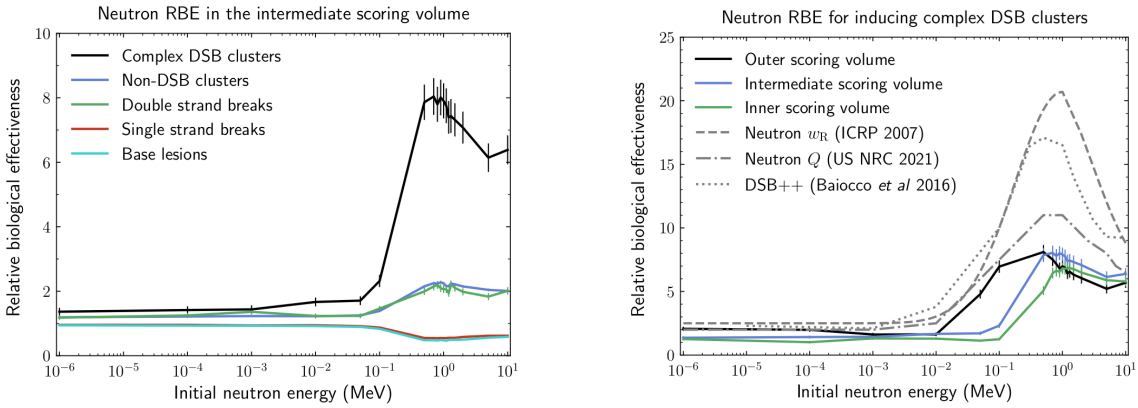


(a) (b)

Figure 4.7 Neutron RBE results of Montgomery *et al*. (2021) [8]. (a) Neutron RBE for different kinds of clustered and isolated lesions in the intermediate scoring volume. (b) Neutron RBE for C-DSBs for different scoring volumes compared with the ICRP weighting factors, US NRC quality factors, and neutron RBE for inducing DSB++ by Baiocco *et al*. (2016) [6].

Montgomery *et al*. (2021) [8] also developed (i) a direct damage scorer that counts the number of direct damage events and (ii) a DNA damage clustering algorithm that groups the scored direct damage hits into their proper clusters. The direct damage scorer and clustering algorithm permitted the quantification of the yields of the different types of simple and clustered DNA lesions (see Figure 4.7-a). By dividing the neutron-induced DYs with their corresponding X-ray-induced DYs, neutron RBE curves for inducing the different types of DNA lesions (by direct action) at different scoring volumes were obtained. It was found that the trend of the neutron RBE for inducing C-DSBs is what is most consistent with the ICRP radiation weighting factors, US NRC quality factors, and the neutron RBE for inducing DSB++ obtained by Baiocco *et al*. (2016) [6] as depicted in Figure 4.7-b. Finally, a custom physics constructor developed by Lund *et al*. (2020) [7] combining the `G4EmDNAPhysics_option2` (opt2) and `G4EmDNAPhysics_option4` (opt4) constructors in Geant4-DNA was imported into TOPAS by Montgomery *et al*. (2021) [8]. This physics constructor combines opt4 and opt2 for better accuracy and energy coverage (see Section 5.2.5). The code for the full nuclear model, direct damage scorer, clustering algorithm, and custom physics constructor have all been released as open-source under the name TOPAS Clustered DNA Damage [32] (hereafter referred to as TOPAS-CDD), and so are not only available to our group but to the community at large.

# Chapter 5

# Methodology

The present chapter begins by elaborating on the objectives of this thesis project before summarizing the existing tools that were used, the additional tools that were developed, and the steps that were undertaken to accomplish the objectives. The methods performed in this project can be broken down into four steps: (i) code implementation of the indirect action simulation pipeline and the damage scorer, (ii) validation and benchmarking of the implemented features, (iii) calculation of the various DYs and corresponding neutron RBE values due to indirect action alone and due to the combined effects of direct and indirect actions (hereafter referred to as combined action), and (iv) comparison of the obtained neutron RBE values with published results. This chapter also describes the various computation resources used to run the simulations.

## 5.1 Project objectives: revisited

This thesis project aimed to expand on the work of Montgomery *et al.* (2021) [8] by performing essentially the same simulations but this time including indirect action to obtain a more comprehensive model of neutron-induced DNA damage. Previously, Montgomery *et al.* (2021) [8] evaluated neutron RBE for inducing clustered DNA lesions (a proxy for carcinogenic risk) as a result of direct action alone. In this work, we aimed to determine neutron RBE for inducing clustered DNA lesions via indirect action alone, as well as combined action. Finally, we sought to compare our obtained neutron RBE with the ICRP neutron weighting factors and the US NRC neutron quality factors.

Our primary objectives, first seen in Section 1.9, are recapitulated as follows:

1. Expand TOPAS-CDD [32] to incorporate indirect action and indirect damage scoring.
2. Validate the implementation of indirect action and indirect damage scoring by comparing indirect DYs with published values.
3. Quantify neutron-induced carcinogenic risk by estimating the RBE of monoenergetic neutrons for inducing simulated clustered DNA damage due to:
   (a) Indirect action alone.
   (b) Combined action.
4. Evaluate the quantification of neutron-induced carcinogenic risk by comparing the energy-dependent neutron RBE curves obtained from primary objective 3 with:
   (a) The neutron RBE for clustered DNA damage due to direct action alone [6, 8].
   (b) The ICRP neutron radiation weighting factors [10].
   (c) The US NRC neutron quality factors [11].

At the time of this study, the full DNA model and damage scorer codes from TOPAS-nBio version 1.0 [134] had not yet been made available. Thus, we developed our own indirect action model and damage scoring algorithm. This development came with the following secondary objectives of primary objective 1:

1. Implement constraints in the chemical stage of simulated water radiolysis to better match reality (e.g. radical scavenging by histone and DNA volumes).
2. Design and develop the implementation of simulated indirect action such that it can be easily used with updated experimental data.
3. Incorporate multithreading into the implemented indirect action simulation pipeline to accelerate the processing time.
4. Extend the damage clustering algorithm in TOPAS-CDD to account for new damage variants (indirect and hybrid lesions).
5. Perform other necessary minor updates in TOPAS-CDD to facilitate the integration of indirect action and damage scoring.

## 5.2 Existing tools

This thesis project was built upon previous work by our research group, published in Lund *et al*. (2020) [7] and Montgomery *et al*. (2021) [8] that were discussed in Sections 4.7.2 and 4.7.3 respectively. This section describes how our previous work was used in the present work.

### 5.2.1 Secondary particle spectra of neutrons and reference photons

Lund *et al*. (2020) [7] used Geant4 to independently simulate (i) monoenergetic primary neutrons with 18 energies between 1 eV and 10 MeV (i.e., the energy range relevant to photon and electron EBRT), and (ii) a reference radiation of 250 keV X-rays. All simulated irradiations were isotropically incident on an ICRU sphere [5] with three scoring volumes at varying radial depths (see Figure 4.3). A total of approximately $10^{10}$ primary particles were simulated in each irradiation. For all the secondary particle tracks generated in each scoring volume, the particle type and energy were recorded and each track was terminated at the point of generation. Thus, the secondary particle energy spectra was obtained for each $E_0^{n^0}$, as well as the 250 keV photons, in each scoring volume. For each set of secondary particle spectra and each scoring volume, the total dose delivered to the volume by a certain particle type was divided by the overall dose delivered to obtain the particle type's relative dose contribution to the volume. In this thesis work, we exposed a custom cell and DNA model to particles stochastically sampled from the neutron and photon secondary particle spectra obtained by Lund *et al*. (2020) [7].

### 5.2.2 Geometric DNA and cell model

In the geometric nuclear DNA model developed by Montgomery *et al*. (2021) [8] in TOPAS-CDD [32], nucleotide base pairs consist of six spheres representing two nucleobases, two deoxyribose sugars, and two phosphate groups (see Figure 5.1-a). These spheres have radii corresponding to those of the respective molecules they represent and are cut at overlapping regions that represent the various covalent bonding sites between adjacent molecules. The volume cutting is necessary for the unique identification of each volume. 154 nucleotide base pairs are chained in a double helix fashion and wrapped around a cylindrical volume (representing a histone protein) to form a nucleosome (see Figure 5.1-b). 90 of such nucleosomes arranged helically around an axis form a cylindrical chromatin fibre (see Figure 5.1-c). 20 of such fibres are organized in a fractal pattern inside a voxel as described by Zhu *et al*. (2020a)

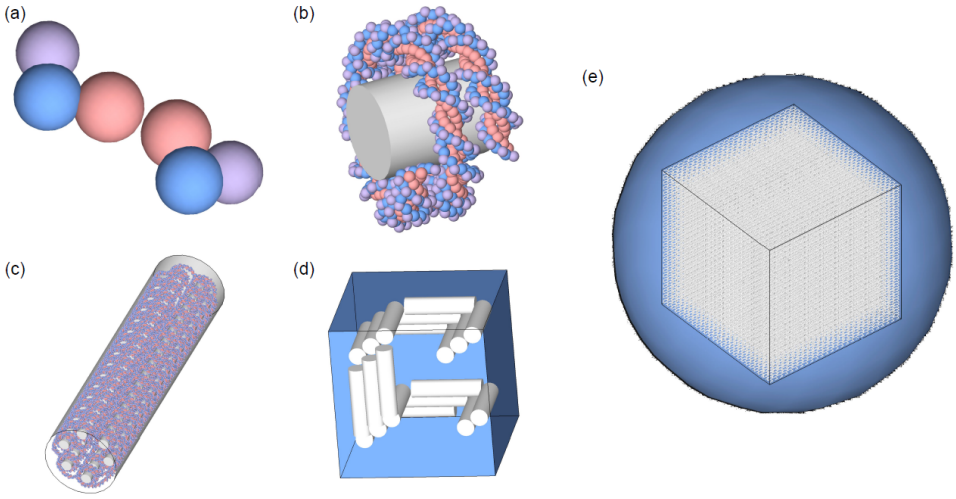


Figure 5.1 The components of the full cell model developed by Montgomery *et al.* (2021) [8]. (a) A nucleotide base pair (red: nucleobases, blue: deoxyribose molecules, purple: phosphate groups). (b) A nucleosome containing 154 base pairs in a double helix around a histone protein. (c) A chromatin fibre containing 90 nucleosomes in a helical pattern. (d) A voxel containing 20 chromatin fibres in a fractal pattern. (e) A full model of a human fibroblast cell with a cubic nucleus containing $26^3$ voxels. Figure from L. Montgomery [2] with permission.

[30] based on chromatin folding analyses by Lieberman-Aiden *et al.* (2009) [153] (see Figure 5.1-d). The full nuclear DNA model consists of $26^3$ cubic voxels placed in a 3D array, resulting in approximately 6.3 Gbp in a cubic volume of 475 $\mu$m$^3$ (density of 13.3 Mbp/$\mu$m$^3$). For reference, a human cellular nucleus with a volume of ~500 $\mu$m$^3$ [154] contains about 6.2 Gbp [42] of nucleotides with a density of approximately 12 Mbp/$\mu$m$^3$. The nuclear DNA is enclosed in a spherical cell volume of 2000 $\mu$m$^3$ to match that of a human fibroblast cell (see Figure 5.1-e) in the $G_0/G_1$ phase of the cell cycle [155].

To determine the location of induced damages, each voxel, chromatin fibre, DNA strand, nucleotide, and base pair molecule are given unique integer identifiers. The entire cell model and all volumes contained within are treated as liquid water with density of 1 g/cm$^3$, however, nucleotide volumes instead have a density of 1.407 g/cm$^3$ [30, 156]. The cubic nuclear DNA model with its enveloping water volume constitutes the full cell model used in all the simulations performed in this project.

Building the full DNA model with all base pair molecules takes some time. For testing purposes, options to modify the number of structures built (base pairs, nucleosomes, fibres, voxels), various structure lengths, and model complexity (i.e., whether to build base pairs inside

the fibres) are available in TOPAS-CDD [32] and may be tweaked in the parameter file. The default parameter values of our cell model are listed in Table 5.1.

Table 5.1 A summary of the parameters describing the full DNA model by Montgomery *et al.* (2021) [8].

| Structure | Parameter | Value |
|---|---|---|
| DNA base pair | Radius of nucleobase | 0.30 nm |
| | Radius of deoxyribose | 0.29 nm |
| | Radius of phosphate group | 0.27 nm |
| Nucleosome | Bp count per nucleosome | 154 bp (+ 46 bp of linker DNA) |
| | Radius of histone | 2.4 nm |
| | Length of histone | 5.72 nm |
| Chromatin fibre | DNA content per fibre | 90 nucleosomes (18 kbp) |
| | Radius of fibre | 17 nm |
| | Length of fibre | 136 nm |
| Voxel | Fibre count per voxel | 20 fibres |
| | Dimensions of voxel | 0.3 $\mu$m $\times$ 0.3 $\mu$m $\times$ 0.3 $\mu$m |
| Nucleus | Voxel count | 17 576 voxels ($26 \times 26 \times 26$ grid) |
| | Volume | 475 $\mu m^3$ |
| | Bp count | 6.3 Gbp |
| | Density of DNA | 13.3 Mbp/$\mu m^3$ |
| Cell | Volume | 2000 $\mu m^3$ |

### 5.2.3 Direct action implementation and damage scorer

#### Direct action events

The physics modules of TOPAS and TOPAS-nBio permit the simulation of radiation transport of various ionizing particles. To score the direct action of IR on DNA it is first necessary to define the characteristics of the simulation steps where direct action is considered to have occurred. In TOPAS-CDD [32], a direct action event was considered to have occurred whenever all of the following conditions for a given simulation step were true:

- The current track was that of an ionizing particle.
- The pre-step point position was inside a volume of a nucleotide base pair molecule.
- The energy deposition of the step was greater than 0.

### Direct damage scoring

The energy depositions inside each unique nucleobase volume and sugar-phosphate volume pair (two volumes considered as one) were accumulated until the end of a simulation run. For each volume with an energy deposition exceeding a defined threshold, direct damage was considered to have occurred (BD for a nucleobase volume or SSB for a sugar-phosphate pair). For SSBs, this threshold is commonly set at 17.5 eV in the literature [157–159] and is based on the results of a study on the potency of Auger electrons emitted from $^{125}$I to induce SSBs [160]. As discussed in Section 3.2, BDs come in a variety of forms so there is no existing consensus as to what constitutes a BD in simulated irradiated DNA scenarios [141]. Nevertheless, previous studies have applied the same damage criteria for both SSBs and BDs [137, 157, 158].

SSBs from opposing DNA strands that were within 10 bp of each other (i.e., within about one turn of the DNA double helix) [30, 141, 142, 144, 157–159] were counted as one DSB and thus, two SSB counts were removed for each DSB formed. The basis for this separation distance stems from experiments on bacterial DNA [161]. The TOPAS-CDD direct damage scorer was designed such that the energy deposition thresholds for defining a SSB and a BD, as well as the maximum separation distance defining a DSB may be modified easily by the user from the TOPAS parameter text file. The default value used for both was 17.5 eV.

### Other features of the direct damage scorer

Since the custom scorer class of TOPAS-CDD kept track of the energy depositions to the various DNA volumes, it was also designed to track the dose delivered to the sensitive volumes in each simulation run. Tracking the total dose delivered in our irradiation simulations was necessary given that our RBE values are essentially ratios of DYs induced by neutrons and X-rays at the same dose. As such, a dose threshold was implemented as an optional stopping criterion for the simulations (instead of simply reaching a specified number of primary particles). Since each simulation event stochastically delivers a unique amount of dose, the exact user-specified dose threshold is improbable to achieve. Thus, the total dose delivered in a simulation run likely exceeds the specified dose.

### 5.2.4 DNA damage clustering algorithm

The DNA damage clustering algorithm is technically part of the direct damage scorer and is optionally executed alongside the DSB-counting step described in Section 5.2.3. All lesions that are within 40 bp of each other are considered to be part of the same cluster [52, 53, 74]. Cluster grouping starts with two lesions fitting the distance separation criterion and more lesions are added to the cluster until there are no more lesions in the next 40 bp beyond the two ends of the formed cluster [32]. The appropriate counts of simple lesions and isolated DSBs are deducted as they are added to a cluster. If a cluster contains at least one DSB, it is considered a C-DSB cluster. If the cluster only has simple lesions, it is considered a N-DSB cluster. From the parameter file, the user can modify the separation distance that defines clusters, and enable or disable the clustering of lesions.

### 5.2.5 Hybrid physics constructor

The opt4 physics constructor of Geant4-DNA uses models with more recent values than those of the opt2 constructor but can only track electrons from 10 keV down to 8 eV, whereas the opt2 constructor works for track-structure electron transport from 1 MeV down to 7.4 eV [130]. The TOPAS-compatible physics constructor in TOPAS-CDD combining the opt2 and opt4 models (aptly named `G4EmDNAPhysics_hybrid2and4` [32]) for improved transport accuracy and energy coverage was used for all irradiation simulations in this thesis project. The energy cutoff for our simulated electrons was set at 10 eV (recommended by the TOPAS collaboration [174]). Since Geant4-DNA only offers one set of physics models for protons (10 eV to 100 MeV [4]) and alpha particles (1 keV to 400 MeV [4]) [130], the hybrid constructor uses these same models. These models are listed in Table 5.2.

## 5.3 Step 1: Code implementation

This step aimed to accomplish primary objective 1 which involved the software design and development of our indirect action simulations and indirect damage scoring. All the development performed in this step was done via the TOPAS extensions framework and all the code (written in C++) was appended to the appropriate custom classes in TOPAS-CDD [32]. The TOPAS version used in this project was version 3.6.1, which was built upon Geant4 version 10.06.p03.

Table 5.2 The various physical processes in liquid water and their respective physics models employed by the hybrid physics constructor used in this work [7, 8, 14, 15].

| Primary particle | Physical process | Model | Energy range |
|---|---|---|---|
| Electron | Excitation | Emfietzoglou dielectric model [162] | 10 keV – 1 MeV |
| | | Emfietzoglou–Kyriakou dielectric model [163] | 10 eV – 10 keV |
| | Ionization | Emfietzoglou dielectric model [162] | 10 keV – 1 MeV |
| | | Emfietzoglou–Kyriakou dielectric model [163] | 8 eV – 10 keV |
| | Elastic scattering | Champion partial wave model [164] | 10 keV – 1 MeV |
| | | Uehara screened Rutherford model [165] | 9 eV – 10 keV |
| | Vibrational excitation | Michaud-Sanche data [166] | 2 eV – 100 eV |
| | Electron attachment | Melton data [167] | 4 eV – 13 eV |
| Proton | Excitation | Born-Bethe model [168] | 500 keV – 100 MeV |
| | | Miller-Green electron speed scaling model [169] | 10 eV – 500 keV |
| | Ionization | Born-Bethe model [168] | 500 keV – 100 MeV |
| | | Rudd model [170, 171] | 100 eV – 500 keV |
| | Electron capture/loss | Dingfelder dielectric formalism [169] | 100 eV – 10 MeV |
| | Elastic scattering | Tran classical model [172] | 100 eV – 1 MeV |
| $\alpha$ particle | Excitation | Miller-Green electron speed scaling model [169] | 1 keV – 400 MeV |
| | Ionization | Rudd model [170, 171] | 1 keV – 400 MeV |
| | Electron capture/loss | Dingfelder model [173] | 1 keV – 10 MeV |
| | Elastic scattering | Tran classical model [172] | 100 eV – 10 MeV |

### 5.3.1 Indirect action implementation and damage scorer

The development of the indirect action implementation and indirect damage scoring required familiarity with various Geant4 functions to access information such as the molecule type and the locations of the step points. The pertinent code in this section was written as an update to the `ProcessHits` method of the TOPAS-CDD DNA damage scorer class. The `ProcessHits` method is executed at every step of the simulation that falls within designated sensitive volumes.

#### Indirect action events

The physics and chemistry constructors available in TOPAS-nBio handle the condensed-history simulation of primary ionizing particles and the track-structure simulation of secondary particles and hydrolytic chemical species. Thus, implementing indirect action involved defining the interactions of the various reactive chemical species with the DNA volumes. In this thesis project, indirect action was considered to occur in a given simulation step if all of the following conditions were met:

- The track of the current step is that of a reactive molecule.
- The pre-step point position is **not** inside a nucleotide base pair molecule volume.
- The pre-step point position is **not** inside a histone volume.
- The post-step point position is inside a nucleotide base pair molecule volume.

#### Indirect damage scoring

Following the precedent of previous work described in Section 4.6.3, only a certain proportion of simulated indirect action events are considered to damage the corresponding DNA volumes. In practice, a pseudorandom number $x$ is generated when a simulated reactive molecule $A$ undergoes an indirect action event with DNA moiety volume $B$. Given that some reactive molecules are more potent at damage induction, DNA damage is only considered to be inflicted if $x < P_A^B$, the given damage probability for the indirect action event between $A$ and $B$.

Consistent with previous simulations of indirect damage (as mentioned in Section 4.6.3), we only scored damage resulting from interactions between highly reactive ·OH radicals and the sugar-phosphate backbone. For indirect SBs, we set a damage probability of 40% for indirect action events between ·OH radicals and pairs of deoxyribose and phosphate volumes. This value

was chosen for two reasons: (i) in consideration of findings discussed in Section 3.2.3 showing that 2 out of 5 C-H bonds ($\frac{2}{5} = 0.4$) in the deoxyribose molecules are more accessible to ·OH radicals and, as such, are more prone to damage [68, 141], and (ii) to maintain consistency with similar work using Geant4-DNA [141, 142, 144] and TOPAS-nBio [30] in order to facilitate DY comparisons. In our DNA model, $\frac{4}{6}$ spherical volumes in a nucleotide base pair represent backbone molecules. Considering the overall availability and exposure of our DNA backbone volumes to simulated ·OH radicals, we estimate that about 27% of all ·OH interactions with DNA volumes result in a SB, which is in between the experimental estimates presented in Section 3.2.3. Given the current lack of published data for simulated BDs due to indirect action, ·OH interactions with nucleobases in the present work were simulated to induce BDs at the same probability of 40% (analogous to how our direct SBs and BDs use the same damage threshold [8]), but were never considered to result in additional SBs (discussed earlier in Section 3.2.3). The damage probabilities of all other interactions between reactive species and DNA volumes were set to zero.

### 5.3.2 Constraints in the chemical stage of water radiolysis

The parameter $T_{chem}$ as well as the time-step resolution of the simulation can be configured from the options of the chemistry constructor. For all simulations of indirect damage performed in this project, $T_{chem}$ was set to 1 ns which is approximately the lifetime of ·OH radicals in cells [39], with a time-step resolution of 1 ps. Thus, only early DNA damage (well in advance of the activation of DNA repair mechanisms discussed in Section 3.3.1) was considered. The chemistry constructor used was `TsEmDNAChemistry` (the default chemistry constructor of TOPAS-nBio), which offers revised reaction parameters over its Geant4-DNA counterpart `G4EmDNAChemistry` [13]. Although it is possible to simulate additional chemical species in TOPAS-nBio as presented in Table 4.1, we opted to limit our simulations to the chemical species available in Geant4-DNA for benchmarking with previously-published work. The simulation parameters defining water radiolysis (discussed in Section 4.4.2) that were applied in this work are presented in Tables 5.3 to 5.5.

The following additional constraints (hereafter referred to as constraints 1 to 3) were implemented to make the chemical stage of the water radiolysis simulations more realistic (secondary objective 1), similar to the constraints described by Zhu *et al.* (2020a) [30]:

1. ·OH radical tracks were terminated after an indirect action event (whether or not DNA damage was inflicted, i.e., with 40% probability as described in Section 5.3.1) since they would have been rendered stable after reacting with a DNA moiety.
2. Radical tracks (·OH, $e^-_{aq}$, and H· specifically [30]) were terminated immediately upon diffusion into a histone volume, because histone proteins are radical scavengers (discussed in Section 3.2.3).
3. The generation of reactive chemical species was not permitted inside of DNA and histone volumes because these volumes are not made of liquid water in reality. In practice, this constraint amounted to immediately terminating all chemical tracks originating in a DNA or histone volume.

Table 5.3 The diffusion coefficients and reaction radii defaults of TOPAS-nBio [13] for the chemical species simulated in this thesis project.

| Chemical species | Diffusion coefficients ($10^{-9}$ m$^2$/s) | Reaction radius (nm) |
|---|---|---|
| $e^-_{aq}$ | 4.9 | 0.5 |
| ·OH | 2.2 | 0.22 |
| H· | 7.0 | 0.19 |
| $H_3O^+$ | 9.46 | 0.25 |
| $H_2$ | 4.8 | 0.14 |
| $OH^-$ | 5.3 | 0.33 |
| $H_2O_2$ | 2.3 | 0.21 |

Table 5.4 The reactions considered in this thesis project with their respective default reaction rate constants in TOPAS-nBio [13].

| Reaction | Reaction rate constant ($10^{10}$ per Ms) |
|---|---|
| $e^-_{aq} + e^-_{aq} \rightarrow H_2 + 2OH^-$ | 0.636 |
| $e^-_{aq} + \cdot OH \rightarrow OH^-$ | 2.95 |
| $e^-_{aq} + H\cdot \rightarrow H_2 + OH^-$ | 2.5 |
| $e^-_{aq} + H_3O^+ \rightarrow H\cdot$ | 2.11 |
| $e^-_{aq} + H_2O_2 \rightarrow OH^- + \cdot OH$ | 1.10 |
| $\cdot OH + \cdot OH \rightarrow H_2O_2$ | 0.550 |
| $\cdot OH + H\cdot \rightarrow H_2O$ | 1.55 |
| $H\cdot + H\cdot \rightarrow H_2$ | 0.503 |
| $H_3O^+ + OH^- \rightarrow H_2O$ | 11.3 |

### 5.3.3 Modifiable simulation parameters

Simulation parameters specific to the implementation of indirect action and damage scoring in this thesis such as damage probabilities of indirect action events and molecule types scavenged by histones were designed to be user-configurable from the TOPAS parameter file to address secondary objective 2. The default implementations of indirect action, damage determination

Table 5.5 The dissociation schemes and their respective branching ratios of a water molecule in Geant4-DNA [16] and TOPAS-nBio [13] used in this thesis project. The various processes listed in this table are further discussed elsewhere [17].

| Process | | | Probability |
|---|---|---|---|
| Ionization | Dissociative decay | $H_3O^+ + \cdot OH$ | 1 |
| $A^1B_1$ | Dissociative decay | $\cdot OH + H\cdot$ | 0.65 |
| | Relaxation | $H_2O + \Delta E$ | 0.35 |
| $B^1A_1$ | Auto-ionization | $H_3O^+ + \cdot OH + e^-_{aq}$ | 0.55 |
| | Auto-ionization | $\cdot OH + \cdot OH + H_2$ | 0.15 |
| | Relaxation | $H_2O + \Delta E$ | 0.30 |
| Rydberg, diffuse bands | Auto-ionization | $H_3O^+ + \cdot OH + e^-_{aq}$ | 0.50 |
| | Relaxation | $H_2O + \Delta E$ | 0.50 |

and scoring, and corollary restrictions were described in the previous section. The following are the possible modifications that may be evoked by the user in the parameter text file to override the default implementations:

- Whether or not to score direct damage.
- Whether or not to score indirect damage.
- Damage probabilities for molecule-base and molecule-backbone interactions.
- Whether or not histones can scavenge molecule species.
- Molecule species scavenged by the histone volumes.
- Molecule species scavenged by the DNA volumes.

### 5.3.4 Updated multithreading support

One crucial difference between simulations involving only direct action and those incorporating indirect action is simulation time. Direct action simulations using TOPAS-CDD last on the order of tens of minutes or less, whereas indirect action simulations (depending on the set $T_{chem}$, time-step resolution, hardware capabilities, etc.) last for hours or even days due to the sheer amount of molecules to track. Given the large amount of indirect action simulations involved in this project (multiple scoring volumes, neutron energies, and secondary particle species), it

was essential to extend the existing multithreading capabilities of TOPAS-CDD to account for indirect action (secondary objective 3).

### 5.3.5 Updated DNA damage clustering algorithm

To accomplish secondary objective 4, the DNA damage clustering algorithm in TOPAS-CDD was modified and extended to score the indirect and hybrid versions of the different damage types presented in Table 5.6. Hybrid DSBs are defined as DSBs with one direct SSB and one indirect SSB, whereas hybrid C-DSBs and hybrid N-DSBs are clusters containing both direct and indirect lesions. The DSB(s) in hybrid C-DSBs are not necessarily individually hybrid.

Table 5.6 Damage types scored by the original implementation of the TOPAS-CDD DNA damage clustering algorithm alongside those scored by the updated algorithm.

| Original implementation | New implementation |
|---|---|
| Direct SSBs | Direct, indirect, and total SSBs |
| Direct BDs | Direct, indirect, and total BDs |
| Direct DSBs | Direct, indirect, hybrid, and total DSBs |
| Direct C-DSBs | Direct, indirect, hybrid, and total C-DSBs |
| Direct N-DSBs | Direct, indirect, hybrid, and total N-DSBs |

### 5.3.6 Updated DNA model

Only minor updates were performed in the DNA model code of TOPAS-CDD as part of secondary objective 5. These changes concerned the unique identification of histone proteins and their accessibility at the level of the simulation steps and were achieved by assigning them their own identifiable material. In our simulations, the location of an interaction in a given simulation step was identified by checking the material information of the step points. Thus, assigning histone complexes their own material (still liquid water of 1 g/cm$^3$ but with a unique identifier) facilitates the localization of interactions within them.

## 5.4 Step 2: Feature verification and model benchmarking

Step 2 of the methodology involved using the newly extended TOPAS-CDD application to perform multiple simulations designed to primary objective 2. In this step, we first verified the

functionality of the implemented features and then benchmarked the DNA DY results obtained with TOPAS-CDD by running simulations with a similar setup to other published studies and comparing the results. Each unique simulation scenario performed in this work was repeated 100 times for statistical credence. All data analysis and plotting were accomplished using the open-source Python libraries Numpy [175], Pandas [176], and Matplotlib [177].

### 5.4.1 Irradiation scenarios

The simulated irradiations of the full cell model performed in this thesis project used either monoenergetic protons (for benchmarking purposes) or monoenergetic neutrons and photons (for neutron RBE estimations). The incident ionizing particles were generated in a specified region with a given direction until the total amount of dose delivered to the medium exceeded a specified threshold. The proton irradiations (as was also the case for other directly ionizing particles) were more straightforward in that they were explicitly simulated as monoenergetic particles whose delivered dose was relatively simple to track.

Table 5.7 The simulation parameters specific to our benchmarking simulations and neutron RBE simulations for ease of distinction. Both use the rest of the parameters listed in Table 5.8.

| Irradiation purpose | Parameter | Value |
|---|---|---|
| Benchmarking | Source particles | Monoenergetic protons (0.5, 1, 5, 10, 20 MeV) |
| | Origin of particles | Randomly throughout the surface of the cell nucleus. Directed inwards. |
| Neutron RBE estimation | Source particles | Electrons, protons, and/or alpha particles. Energies sampled from neutron or X-ray secondary particle spectra. |
| | Origin of particles | Randomly throughout the entire volume of the cell (including the nucleus). Directed isotropically. |

The neutron and photon irradiations, on the other hand, were not explicitly simulated. Each neutron RBE irradiation in a given scoring volume had (i) associated secondary particle spectra, and (ii) corresponding electron, proton, and alpha radiation components according

to the particle type's relative dose contribution. We only used the electron, proton, and alpha radiation components of each set of secondary particle spectra from the work of Lund *et al.* (2020) [7] because, at the time of the present study, Geant4-DNA did not offer ionization models for the other relevant physical particles (i.e., heavier ions) [130]. In our neutron RBE irradiation scenarios, the energies of the generated particles (electron, proton, and alpha) were stochastically sampled from the appropriate secondary particle spectrum. Each particle type was assigned a maximum dose threshold that was the product of (i) the user-specified neutron (or photon) dose threshold in the TOPAS parameter file (1 Gy for all our simulations) and (ii) the particle type's corresponding relative dose contribution. In brief, our neutron and photon irradiations of the full cell model were actually separate irradiations of electrons, protons, and alpha particles with respective target doses totalling close to 1 Gy.

Our benchmarking simulation scenario most closely matches that of Zhu *et al.* (2020a) [30] that also used the same chemistry constructor to facilitate indirect DNA DY comparisons, while our neutron RBE simulation scenario is identical to that used by Montgomery *et al.* (2021) [8]. The differences in scenario setup for our benchmarking and neutron RBE irradiations are presented in Table 5.7, while the default settings common to both scenarios are in Table 5.8.

### 5.4.2 Verifying direct damage yields

To ensure the independent processing between direct and indirect action and to verify the functionality of the toggles for including direct and indirect damage scoring, simulations using only direct action were performed. The simulation scenario in this verification step was a neutron RBE irradiation setup for all 18 monoenergetic neutron sources (see Section 5.2.1) and reference 250 keV X-ray photons for the inner, intermediate, and outer scoring volumes. The toggle for scoring clustered lesions was activated and the resulting DYs and relevant RBE values of these simulations were compared to the results of Montgomery *et al.* (2021) [8].

### 5.4.3 Verifying multithreading functionality

To verify the functionality of the programmed multithreading support and to measure the efficiency improvement of its use, the cell model was irradiated using our benchmarking simulation scenario using the various thread counts of 1, 5, and 10 for a single proton energy. The proton energy used for these simulations was 10 MeV because the simulation of lower energy protons (higher LET) involved significantly more interactions and thus, they were much

Table 5.8 The default simulation parameters used in this work.

| Parameter | Value |
|---|---|
| Target geometry | Nuclear DNA (see Table 5.1 and Table 5.1) |
| Target material | Liquid water<br>Density of sensitive DNA volumes: 1.407 g/cm$^3$,<br>elsewhere: 1 g/cm$^3$. |
| Physics constructor | `G4EmDNAPhysics_hybrid2and4` (see Table 5.2) |
| Chemistry constructor | `TsEmDNAChemistry` (see Tables 5.3 to 5.4)<br>Chemical stage duration ($T_{chem}$): 1 ns, time-step resolution: 1 ps |
| Additional constraints in the chemical stage | DNA molecules are scavengers of ·OH radicals. |
| | Histones are scavengers of ·OH, $e^-_{aq}$, and H· radicals. |
| | Reactive chemical species are not allowed to be generated inside DNA and histone volumes. |
| Induction of SSB and BD[a] | Direct: 17.5 eV of cumulative energy deposition<br>SSB: in a sugar-phosphate volume pair,<br>BD: in a nucleobase volume. |
| | Indirect[b]: 0.4[c] damage probability for ·OH radical<br>SSB: with a sugar-phosphate volume pair,<br>BD: with a nucleobase volume. |
| Induction of DSB | Two SSBs on opposite strands within 10 bp (direct, indirect or hybrid). |
| Induction of clustered DNA damage[a] | Aggregation of DNA lesions within 40 bp of each other.<br>C-DSB or N-DSB (direct, indirect, or hybrid). |
| Simulation cutoff | 1 Gy of cumulative dose to the nuclear DNA volume. |
| Number of histories | Variable (1 – 10 000 per simulation) |
| Number of runs | 100 |
| Number of threads | 10[b,d] |

[a]No base lesion and clustered damage scoring for benchmarking simulations.
[b]This setting was disabled for the neutron RBE simulations in Step 2 (see Section 5.4.2).
[c]This value was varied in Step 2 (see Section 5.4.5): 0.4 and 0.65.
[d]This value was varied in Step 2 (see Section 5.4.3): 1, 5, 10.

longer to simulate using a single thread. These runs incorporated both direct and indirect action but cluster scoring was disabled. The resulting indirect and direct DYs, and the average duration of simulations were compared.

### 5.4.4 General functionality verification

The functionality verification of most implemented features such as indirect damage scoring, constraints 1 to 3 of the chemical stage, modifiable simulation parameters, and the unique identification of histone proteins were performed via manual inspection of the printed event logs of our test simulations and simulation visualizations provided by TOPAS-nBio. The printed logs show information (volumes and particles involved, materials involved, energy transfer, thread number, whether a track was killed, etc.) about point events in the simulation, while the visualizations permitted the spatial manipulation of simulation snapshots and color-coding of physical and chemical tracks, allowing for the visual verification of events. Damage type counting verification was accomplished by feeding the updated clustering algorithm manually-fabricated lists of damaged base pair IDs with expected counts for each damage type. Features were deemed to be functional if expected outcomes were observed in the printed output logs and/or in visualizations. Simpler geometries (spheres, cubes, and cylinders) were used during test simulations (instead of the full nuclear geometry) for efficiency.

### 5.4.5 SSB and DSB yields comparison with published data

The publications of Friedland *et al.* (2003) [138], Meylan *et al.* (2017) [141], de la Fuentes Rosales *et al.* (2018) [4], Sakata *et al.* (2020) [144], and Zhu *et al.* (2020a) [30], on the irradiation of a DNA model by monoenergetic ionizing particles offered a breakdown of direct and indirect DYs and were used to validate and benchmark our indirect action model. Among these publications, there are differences in the simulation scenarios such as the implementation of indirect action, the structure of the DNA model, the particles used, and the doses delivered. To make the ionizing particles and their resulting DNA DYs as comparable as possible, the particles were expressed in terms of their LET (instead of particle type and energy) and their respective DYs were normalized to the dose delivered and to the total number of base pairs in the DNA model (i.e., in units of per Gy per Gbp).

The benchmarking irradiation scenario was simulated using all proton energies in Table 5.7. These energy values were converted to LET by interpolation from the energy and LET ranges

reported by Sakata *et al*. (2020) [144] that used a similar physics constructor combining opt2 and opt4. For a parameter sensitivity analysis, the damage probabilities of 0.40 and 0.65 were used for ·OH interactions with the sugar-phosphate volume pairs. The resulting DYs (SSBs and DSBs) for each proton energy and damage probability were compared against the yields of the mentioned publications with reported damage-cause contributions. The DSB yields were additionally compared to various other published simulated [137, 139, 140, 142, 143] and experimental [178–181] data. Comparisons of SSB to DSB ratios were also performed.

### 5.4.6 The influence of doubly-damaged sites

Our simulation code contains logic to prevent multiple damage counts (in a unique DNA volume) induced by the same action mechanism (direct or indirect). However, due to the independence of direct and indirect action in our simulations, it is possible for a unique DNA volume to be damaged twice (separately by both direct and indirect action). The incidence of these doubly-damaged events was expected to be rare but was ultimately scored in our benchmarking simulations to determine their relative influence in DYs.

## 5.5 Step 3: Neutron RBE estimation

This step involved simulating the neutron and photon irradiations (i.e., neutron RBE simulation scenario) required to obtain the yields of the different DNA damage types needed to generate the energy-dependent neutron RBE curves listed in primary objective 3.

### 5.5.1 Required simulations

The simulations previously performed by Montgomery *et al*. (2021) [8] described in Section 5.4.2 were repeated, but this time incorporating our implementation of indirect action and damage scoring (i.e., combined action simulations of monoenergetic neutrons and reference X-rays). The secondary particle spectra of all 18 monoenergetic neutron beams and the 250 keV photon beams for the three scoring volumes were used. Since our updated DNA damage clustering algorithm distinguished direct from indirect DNA lesions, we simply isolated the DYs due to indirect action alone from the performed neutron RBE simulations to achieve the values required by primary objective 3-a. To accomplish primary objective 3-b, we simply

considered the totality (direct, indirect, and hybrid) of the respective damage types (SSBs, BDs, DSBs, C-DSBs, and N-DSBs).

### 5.5.2 Damage yields and RBE

For DYs obtained from irradiations using monoenergetic and monospecific directly-ionizing particles (such as those in our benchmarking simulation scenario), it sufficed to divide the obtained DYs by the dose absorbed by the sensitive volumes to normalize according to dose. However, for our neutron RBE irradiations, the DYs $[Y_i^{j,k}(E)]_l$ specific to each secondary particle species $i$, damage type $j$, damage cause $k$, scoring volume $l$, and energy $E$ were first multiplied by their respective correction factors $[D_i(E)/d_i(E)]_l$ (where $D$ is the relative target dose and $d$ is the actual dose received) and summed together to obtain the appropriate neutron and reference X-ray DYs ($[Y_{n^0}^{j,k}(E)]_l$ and $[Y_X^{j,k}]_l$ respectively):

$$[Y_{n^0}^{j,k}(E)]_l = \sum_{i=e^-,\ p^+,\ \alpha} [Y_i^{j,k}(E)]_l \cdot \left[\frac{D_i(E)}{d_i(E)}\right]_l \tag{5.1}$$

$$[Y_X^{j,k}]_l = [Y_{e^-}^{j,k}(250\ \text{keV})]_l \cdot \left[\frac{D_{e^-}(250\ \text{keV})}{d_{e^-}(250\ \text{keV})}\right]_l \tag{5.2}$$

The DYs of the reference 250 keV X-ray photons did not need to be summed over different particle species since they only have electrons as secondary particles. The resulting "corrected" yields were used to calculate the corresponding RBE values:

$$[\text{RBE}^{j,k}(E)]_l = \frac{[Y_{n^0}^{j,k}(E)]_l}{[Y_X^{j,k}]_l} \tag{5.3}$$

All reported values of DYs and RBE for given $i$, $j$, $k$, $l$ and $E$ values were averages obtained from 100 independent simulation runs and were determined along with their respective standard uncertainties of the mean. The different neutron $E$ values ($E_0^{n^0}$) permitted the plotting of energy-dependent neutron DYs and RBE curves. The neutron RBE curves required by primary objective 3 are those pertaining to the induction of N-DSB and C-DSB clusters for each scoring volume $l$ and for $k$ values indirect and total.

## 5.6 Step 4: Neutron RBE comparisons

The appropriate curves of energy-dependent neutron RBE for inducing clustered lesions at various scoring volumes for indirect and combined action were plotted alongside the results of Montgomery *et al.* (2021) [8] and Baiocco *et al.* (2016) [6], the ICRP neutron radiation weighting factors [10], and the US NRC neutron quality factors [11]. A subsequent similarity analysis was performed to accomplish primary objective 4. In addition to the RBE comparisons of primary objective 4, the magnitude of total DYs of our simulations (indirect action alone and combined action) were compared with that of Montgomery *et al.* (2021) [8] (direct action alone) for a more comprehensive assessment of neutron-induced carcinogenic effects.

## 5.7 Hardware used

All simulations performed in this work were processed using the Cedar cluster of Compute Canada [182]. Submitted jobs to the cluster were assigned in either of the following similarly-performing Intel CPU of various architectures: E5 and E7 v4 Broadwell, Platinum Skylake, and Silver/Platinum Cascade Lake running at clock rates of 2.1 to 2.4 GHz. These CPU cores are assigned in nodes of various sizes with varying memory capacity ranging from 125 GB to 3022 GB. Although the Cedar cluster has GPU support for faster repetitive processing, this feature was not used because of current incompatibility with TOPAS.

## 5.8 Simulation hyperparameters

### 5.8.1 Number of independent runs

Although only 100 runs were considered in the data analysis of each unique simulation scenario, an original batch of 125 independent simulation runs were submitted to the cluster, because it was found that some runs (especially for higher-LET particles) would crash upon encountering an intermittent and unsolvable memory error (segmentation fault) present in the version of Geant4 upon which TOPAS and TOPAS-nBio were built [183].

### 5.8.2 Thread count, memory allocation, and simulation time limit

Simulation hyperparameters including the amount of threads to be used, allocated memory, and simulation time limit were specified for each job submission to the cluster, where they were then scheduled for processing. Whenever an aborted simulation was encountered either due to insufficient memory or a specified time-limit that was too short, the appropriate settings were adjusted, and the simulation was rerun as necessary.

As mentioned in Section 5.2.3, the last event considered by our scorer to deliver a dose is the first event that brings the absorbed dose of the sensitive volume(s) past the specified dose threshold. With multithreading, it was possible that multiple events were still being processed while only one last event was necessary to complete the simulation. Since only the main thread had the information about the total amount of dose delivered, the other threads processing unnecessary simulated events could not be aborted prematurely. Thus, using an excessive number of threads could significantly slow down a simulation. As such, we chose the thread count of 10 for the rest of the simulations for satisfactory efficiency without suffering much drawback from the dose threshold stopping condition.

Another reason for this thread count choice was that the duration of a simulation varied with the particle type's relative dose contribution and LET. Certainly, the more particles to be simulated and the more interactions per event, the longer the simulation. Also, since each thread processed a single simulation event, higher-LET particles required more memory to store more information from the greater number of ensuing interactions. Given that all of the threads assigned for a simulation run shared the same amount of memory specified in the batch job submission, more threads meant less memory allotted per simulation event, which risked causing the simulation of higher-LET particles to abort due to insufficient memory. Thus, the amount of memory and time limit assigned for an irradiation simulation were made proportional to the irradiating particle's relative dose contribution and LET, and in consideration of the set number of threads. The thread count of 10 was found to work well with the memory allocations for each simulation run ranging from 2 GB to 16 GB, resulting in simulation times between <5 min and $\sim$12 h (electrons: <5 min to $\sim$1.5 h, protons: >3 h to $\sim$12 h, alphas: >1 h to >3 h).

# Chapter 6

# Results

This chapter presents the results obtained for each of the four steps of the methodology described in the previous chapter.

## 6.1 Step 1: Code implementation

All the code written in this step permitted the expansion of TOPAS-CDD [32] to incorporate indirect action and damage scoring (i.e., primary objective 1).

### 6.1.1 Summary of expansions to TOPAS-CDD

The updates to the C++ custom classes in TOPAS-CDD may be summarized as follows:

- `ScoreClusteredDNADamage.cc` (DNA damage scorer):
  - Added: simulation of indirect action events.
  - Added: indirect damage scoring.
  - Added: simulation constraints 1 to 3 in the chemical stage (secondary objective 1).
  - Added: user-modifiable simulation parameters listed in Section 5.3.3 (secondary objective 2). Figure 6.1 shows the various additional variables and toggles listed in Section 5.3.3 implemented as modifiable simulation features in a parameter text file.
  - Updated: multithreading feature to support indirect action and damage scoring (secondary objective 3).

  - Updated: DNA damage clustering algorithm to account for indirect and hybrid lesions (secondary objective 4).

- `VoxelizedNuclearDNA.cc` (DNA model):
  - Added: unique identification of histone volumes via their composing material (secondary objective 5).

```
# Parameters defining indirect DNA damage
u:Sc/ClusterScorer/DamageProbabilityOnInteraction/SSB/OH = 0.4
u:Sc/ClusterScorer/DamageProbabilityOnInteraction/BD/OH = 0.4
u:Sc/ClusterScorer/DamageProbabilityOnInteraction/SSB/OHm = 0.0
u:Sc/ClusterScorer/DamageProbabilityOnInteraction/BD/OHm = 0.0
u:Sc/ClusterScorer/DamageProbabilityOnInteraction/SSB/e_aq = 0.0
u:Sc/ClusterScorer/DamageProbabilityOnInteraction/BD/e_aq = 0.0
u:Sc/ClusterScorer/DamageProbabilityOnInteraction/SSB/H2 = 0.0
u:Sc/ClusterScorer/DamageProbabilityOnInteraction/BD/H2 = 0.0
u:Sc/ClusterScorer/DamageProbabilityOnInteraction/SSB/H3Op = 0.0
u:Sc/ClusterScorer/DamageProbabilityOnInteraction/BD/H3Op = 0.0
u:Sc/ClusterScorer/DamageProbabilityOnInteraction/SSB/H = 0.0
u:Sc/ClusterScorer/DamageProbabilityOnInteraction/BD/H = 0.0
u:Sc/ClusterScorer/DamageProbabilityOnInteraction/SSB/H2O2 = 0.0
u:Sc/ClusterScorer/DamageProbabilityOnInteraction/BD/H2O2 = 0.0

# Parameters defining direct DNA damage
d:Sc/ClusterScorer/EnergyThresholdForHavingSSB = 17.5 eV
d:Sc/ClusterScorer/EnergyThresholdForHavingBD = 17.5 eV

# Parameters to define DSBs and clustered DNA damage
i:Sc/ClusterScorer/BasePairDistanceForDefiningDSB = 10
i:Sc/ClusterScorer/BasePairDistanceForDefiningCluster = 40

# Additional constraints to the chemical stage
sv:Sc/ClusterScorer/SpeciesToKillByDNAVolumes = 1 "OH"
sv:Sc/ClusterScorer/SpeciesToKillByHistones = 3 "OH" "e_aq" "H"
b:Sc/ClusterScorer/HistoneAsScavenger = "True"

# Options to modify how damage yields are recorded
b:Sc/ClusterScorer/IncludeDirectDamage = "True"
b:Sc/ClusterScorer/IncludeIndirectDamage = "True"
b:Sc/ClusterScorer/ScoreClusters = "True"
```

Figure 6.1 The different modifiable parameters affecting DNA damage scoring and counting in our simulations as they appear in the TOPAS parameter file. In blue: existing TOPAS-CDD parameters. In green: additional parameters from the current project.

## 6.2 Step 2: Feature verification and model benchmarking

All the verification, benchmarking, and detailed comparison performed in this step permitted the accomplishment of primary objective 2: to validate the implementation of indirect action and indirect damage scoring.

### 6.2.1 Verifying direct damage yields

Figure 6.2 shows the resulting direct DNA DYs and neutron RBE curves obtained using our updated TOPAS-CDD simulation code with direct damage scoring but no indirect damage scoring. Our results are compared with those of Montgomery *et al.* (2021) [8] using the original TOPAS-CDD code [32].

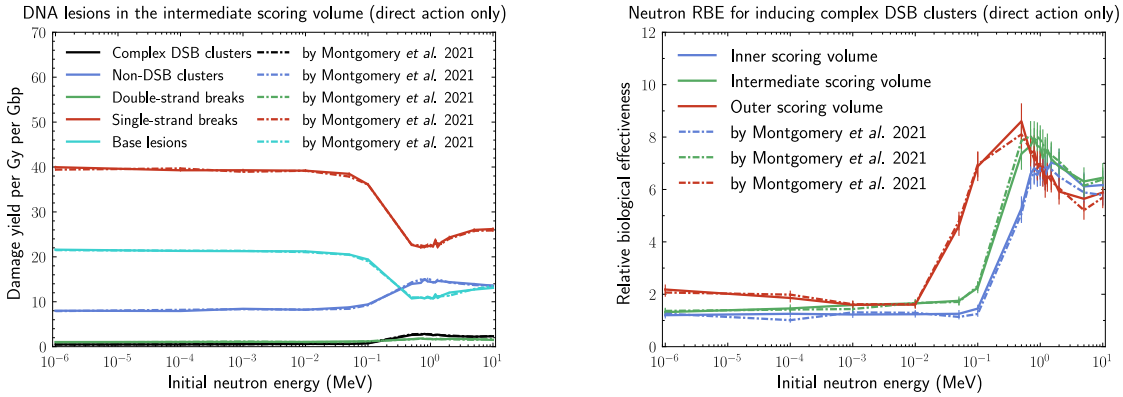


(a) (b)

Figure 6.2 Comparison between the direct damage types obtained by Montgomery *et al.* (2021) [8] using TOPAS-CDD and this work using the extended simulation code but with indirect damage scoring deactivated. (a) Yields of DNA lesions in the intermediate scoring volume. (b) Neutron RBE for inducing complex DSB clusters in all three scoring volumes.

### 6.2.2 Verifying multithreading functionality

Table 6.1 shows the SB yields (SBYs) and duration of our benchmarking irradiations as a function of the number of computing threads (1, 5, and 10). The standard uncertainties of the mean are reported with each calculated value.

Table 6.1 A summary of the SB yields ($Y_{p^+}^{SB,\,k}$) obtained from our benchmarking scenario simulations performed using 10 MeV protons at various thread counts, with their respective duration.

| Thread count | $Y_{p^+}^{SB,\,total}$ (per Gy per Gbp) | $Y_{p^+}^{SB,\,direct}$ (per Gy per Gbp) | $Y_{p^+}^{SB,\,indirect}$ (per Gy per Gbp) | Simulation duration (h) |
|---|---|---|---|---|
| 1 | 148±4 | 46±2 | 101±3 | 11.4±0.1 |
| 5 | 150±4 | 47±2 | 103±3 | 2.74±0.05 |
| 10 | 149±4 | 46±2 | 103±3 | 1.21±0.02 |

### 6.2.3 SSB and DSB yields comparison with published data

Figure 6.3 shows the resulting SBYs of our benchmarking irradiation simulations using two $P_{.OH}$ values in comparison with published values. Similar to other presented work, $P_{.OH}$ in our

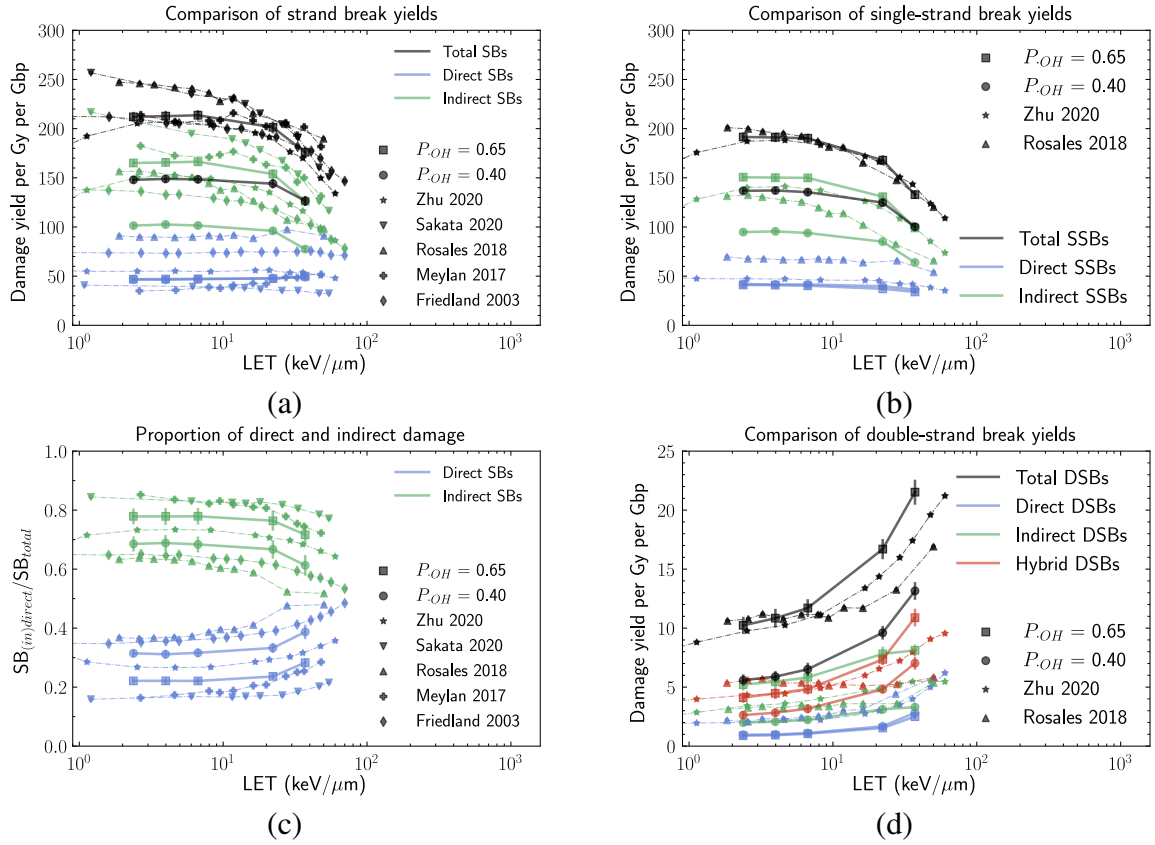


Figure 6.3 Comparison of our SB yields obtained using $P_{OH}$ values of 0.40 and 0.65 in a benchmarking simulation scenario with published data presenting a breakdown according to damage-inducing action. (a) SB yields. (b) SSB yields. (c) Proportion of direct and indirect SBs. (d) DSB yields.

simulations only resulted in lesions to the sugar-phosphate backbone, i.e., base lesions were not counted. On the other hand, Figure 6.4 presents a comparison of our DSB yields with other simulation and experimental results, and a comparison of SSB/DSB yields of several work.

### 6.2.4 The influence of doubly-damaged sites

Doubly-damaged sites (volumes of DNA moieties affected by both direct and indirect action) were found to be infrequent but increasing with LET (due to the more clustered nature of lesions). In the LET range of our monoenergetic protons, this incidence range from 1.0±0.2% to 1.9±0.2% (relative to the total amount of SBs) for $P_{OH} = 0.40$, and from 1.1±0.2% to 2.1±0.2% for $P_{OH} = 0.65$.

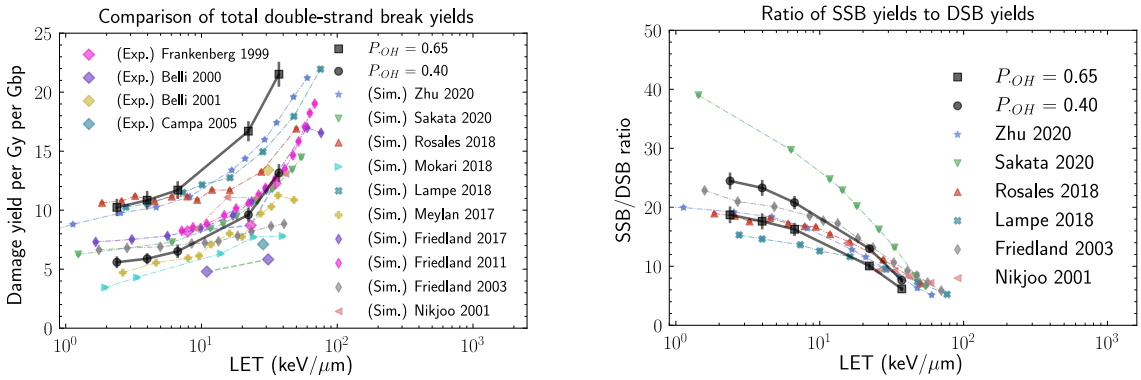


(a) (b)

Figure 6.4 (a) Comparison of our DSB yields using two $P_{OH}$ values with published experimental (Exp.) and a wider range of simulation (Sim.) data. (b) Comparison of our SSB/DSB ratios with published data.

## 6.3 Step 3: Neutron RBE estimation

The various DYs due solely to indirect action and those induced by the compounding effects of direct and indirect action (i.e., combined action) are presented in Figure 6.5, while their corresponding neutron RBE curves (required by primary objective 3) are shown in Figure 6.6. Figure 6.7 shows a damage-cause breakdown of Figure 6.5-b2 (DYs in the intermediate scoring volume due to combined action), while Figure 6.8 does the same for Figure 6.6-b2 (RBEs in the intermediate scoring volume due to combined action).

### 6.3.1 Damage yields in each scoring volume

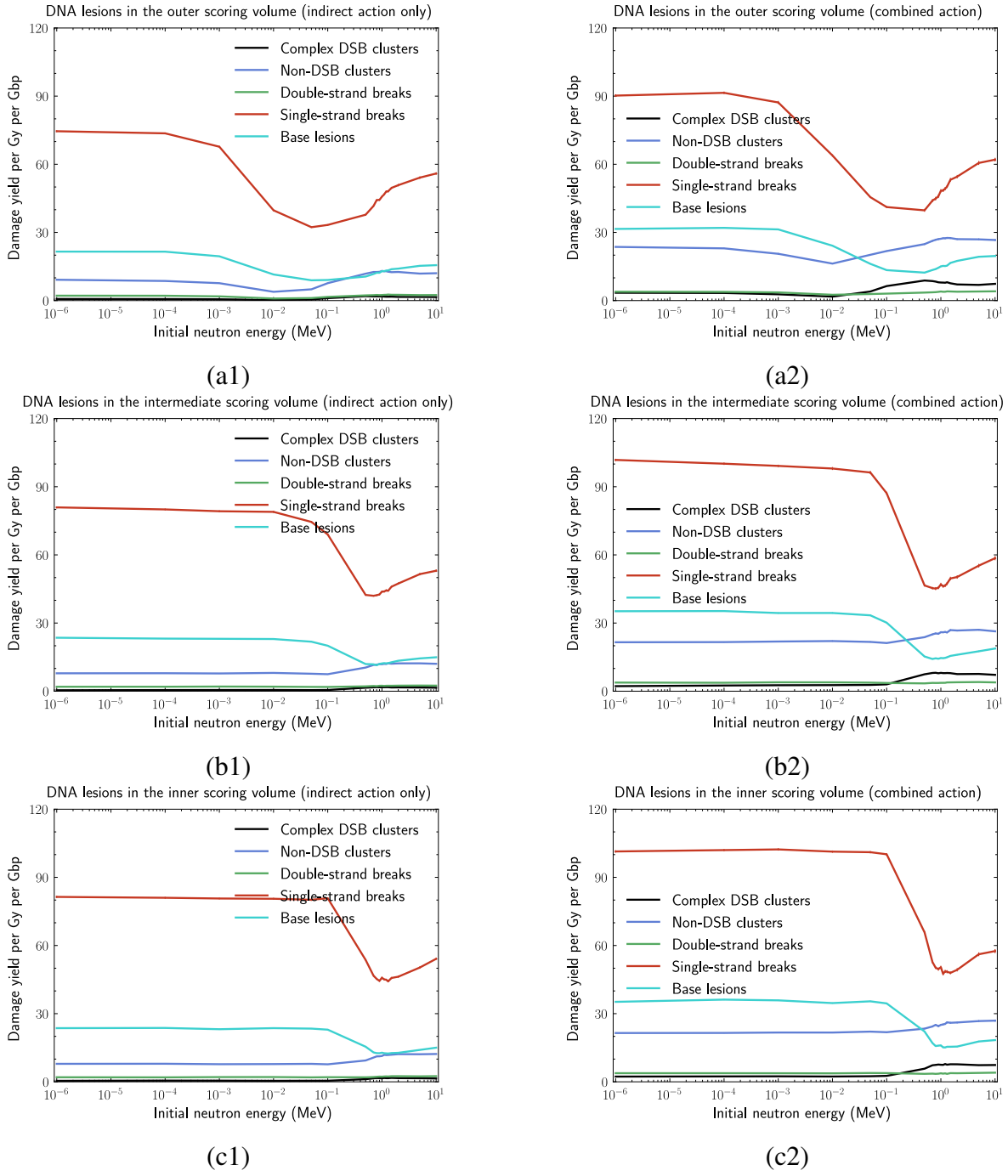


Figure 6.5 Different DYs due to (1, left) indirect action only and (2, right) combined action in the (a) outer, (b) intermediate, and (c) inner scoring volumes.

### 6.3.2 RBEs in each scoring volume

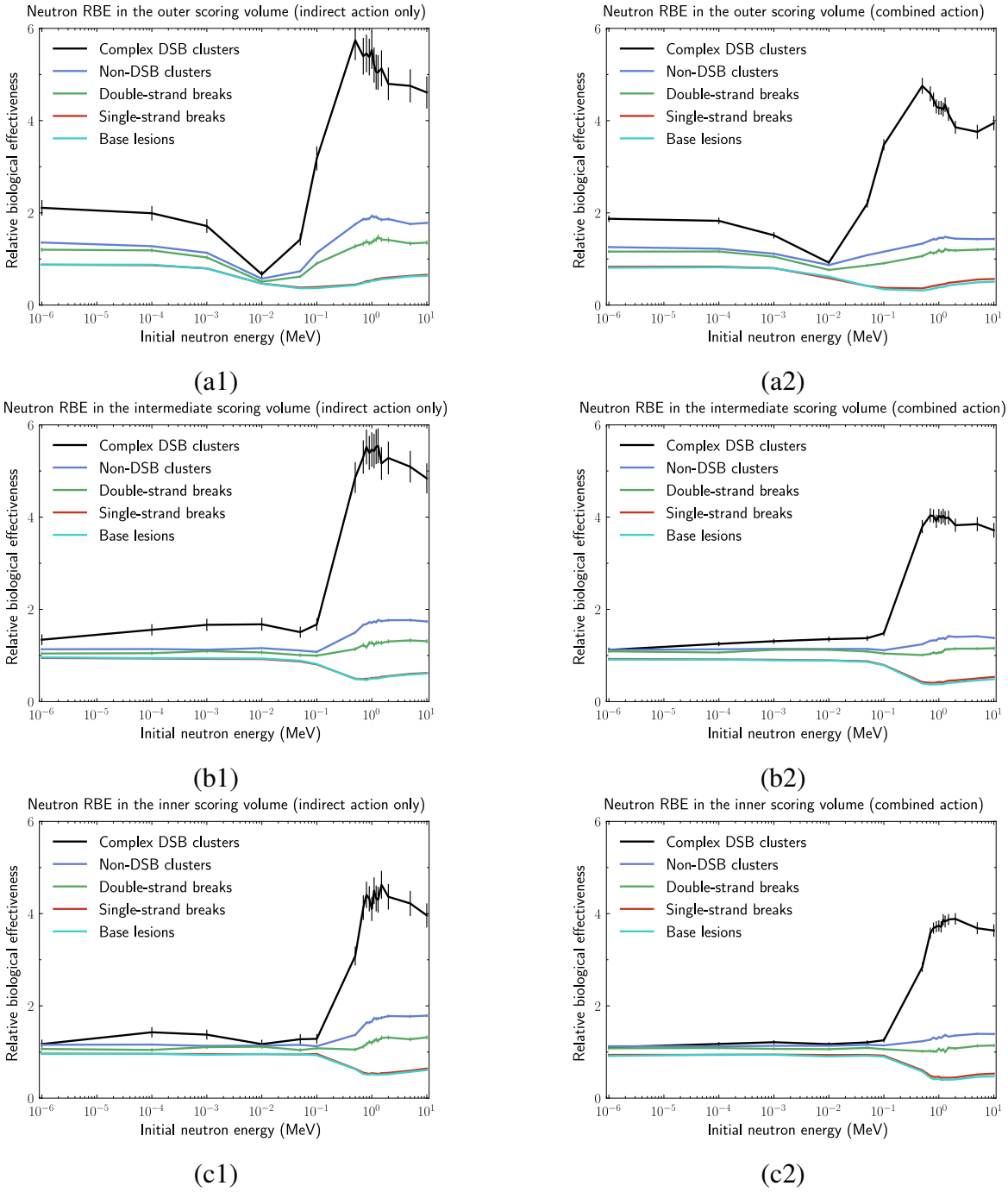


Figure 6.6 Neutron RBE for inducing various lesion types due to (1, left) indirect action only and (2, right) combined action in the (a) outer, (b) intermediate, and (c) inner scoring volumes.

### 6.3.3 Damage contributions in combined action

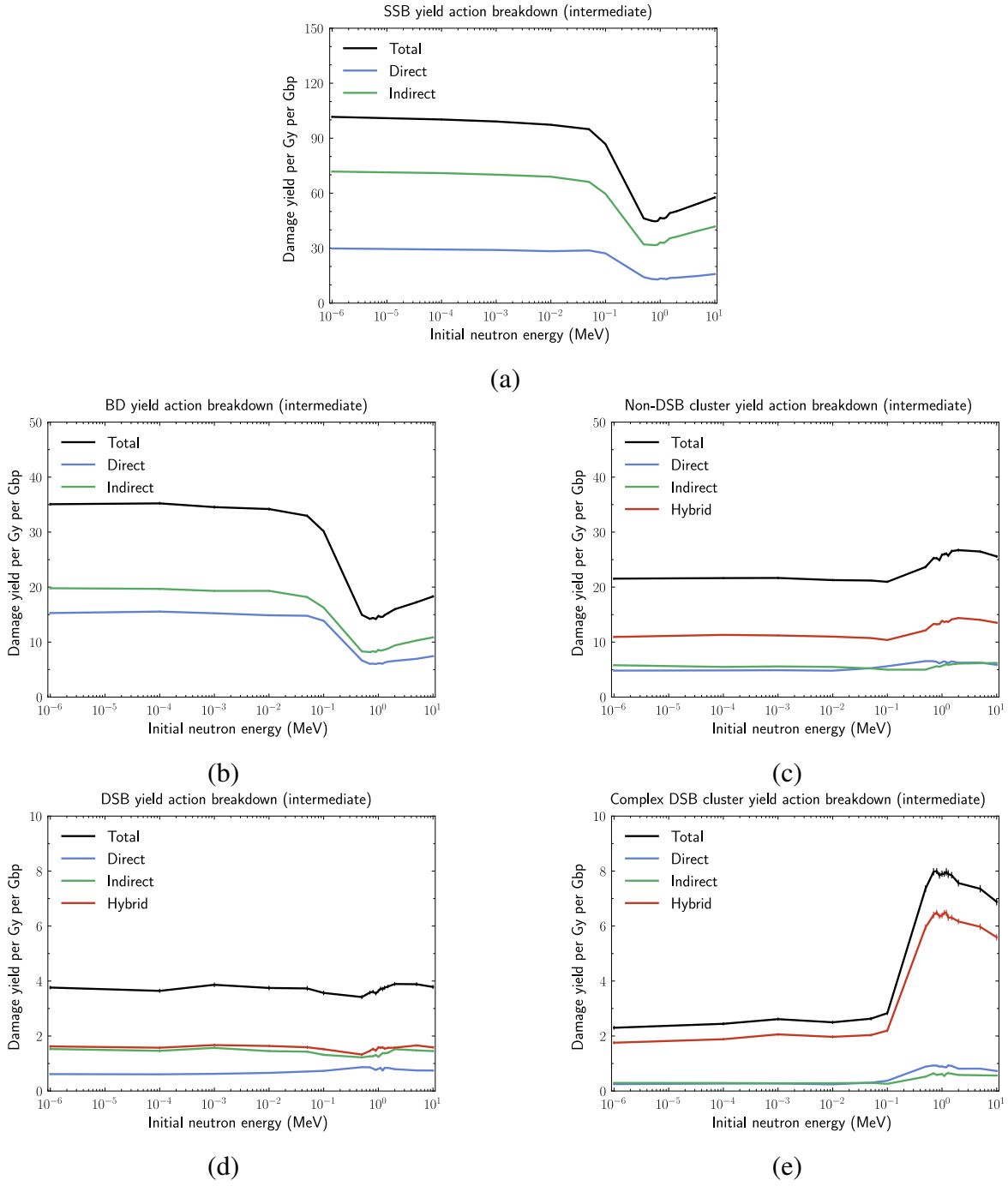


Figure 6.7 Action breakdown of neutron-induced DYs in the intermediate scoring volume (see Figure 6.5-b2): (a) SSBs, (b) BDs, (c) N-DSBs, (d) DSBs, and (e) C-DSBs.

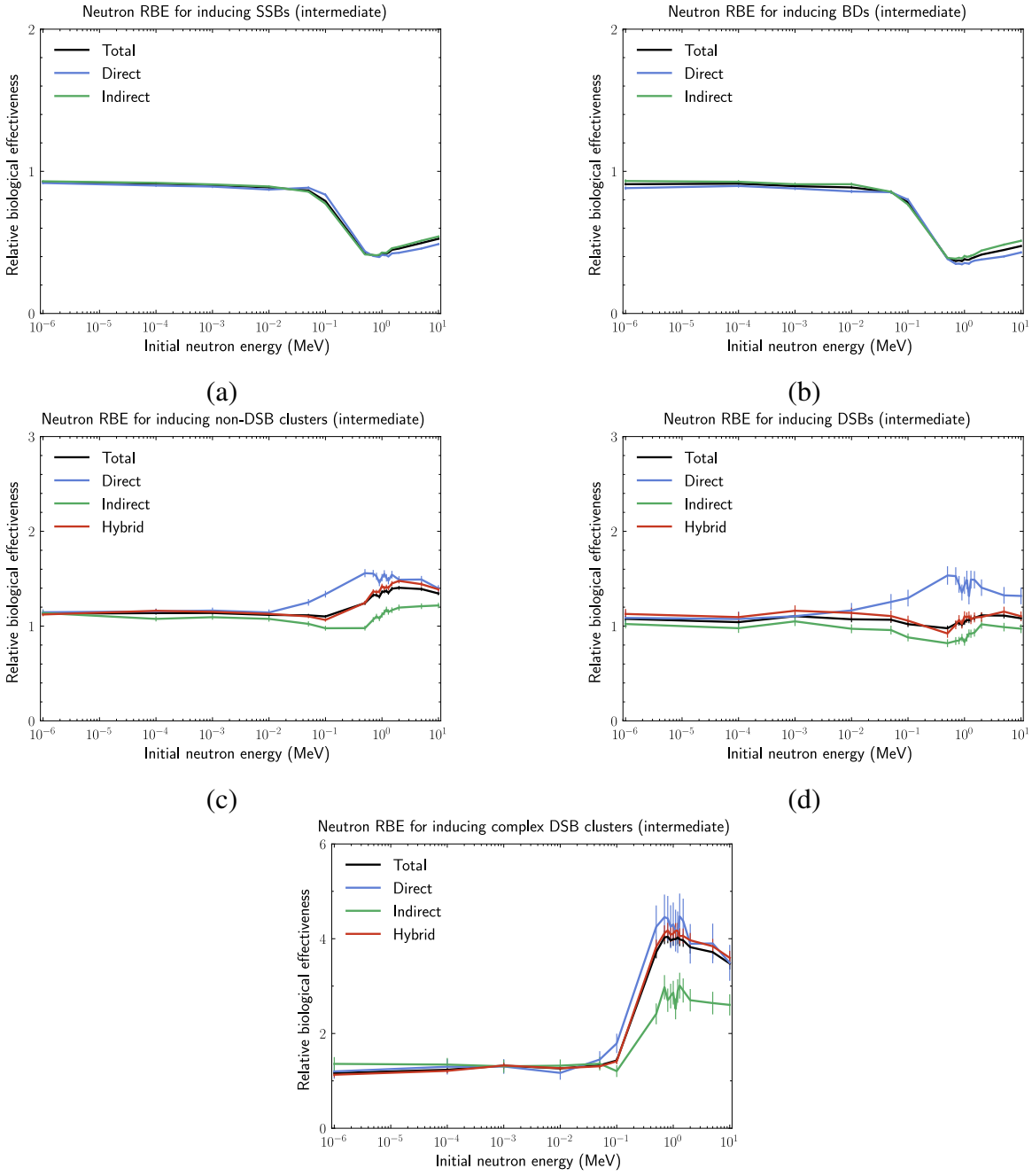


Figure 6.8 Action breakdown of neutron RBE for inducing different types of DNA lesions in the intermediate scoring volume (see Figure 6.6-b2): (a) SSBs, (b) BDs, (c) N-DSBs, (d) DSBs, and (e) C-DSBs.

## 6.4 Step 4: Neutron RBE comparisons

From the neutron RBE curves we have produced in Step 3 for indirect action only and combined action, we remark that the RBE curves for C-DSB clusters resemble those produced by Montgomery *et al*. [8] that simulated direct action exclusively.

In accordance with primary objective 4, we also compared our RBE curves to that of Baiocco *et al*. (2016) [6], the US NRC neutron quality factors [11], and the ICRP neutron radiation weighting factors [10].

### 6.4.1 Indirect action alone

Figure 6.9-a shows our neutron RBE curves for inducing C-DSBs due to indirect action alone plotted against mentioned comparison data. Figure 6.9-b is a comparison of DYs due to indirect action alone and those due to direct action alone.

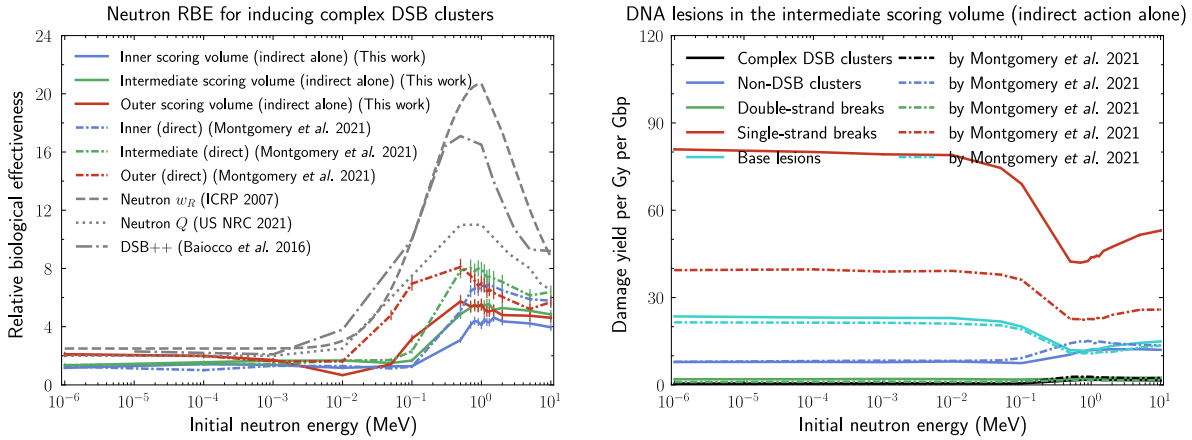


(a) (b)

Figure 6.9 (a) Neutron RBE for inducing C-DSBs via indirect action alone in the various scoring volumes compared with various published results. (b) Neutron-induced DYs due to indirect action alone in the intermediate scoring volume compared with those due to direct action alone by Montgomery *et al*. (2021) [8].

### 6.4.2 Combined action

Figure 6.10 depicts similar plots as Figure 6.9, but with DY and RBE data due to combined action instead of indirect action alone.

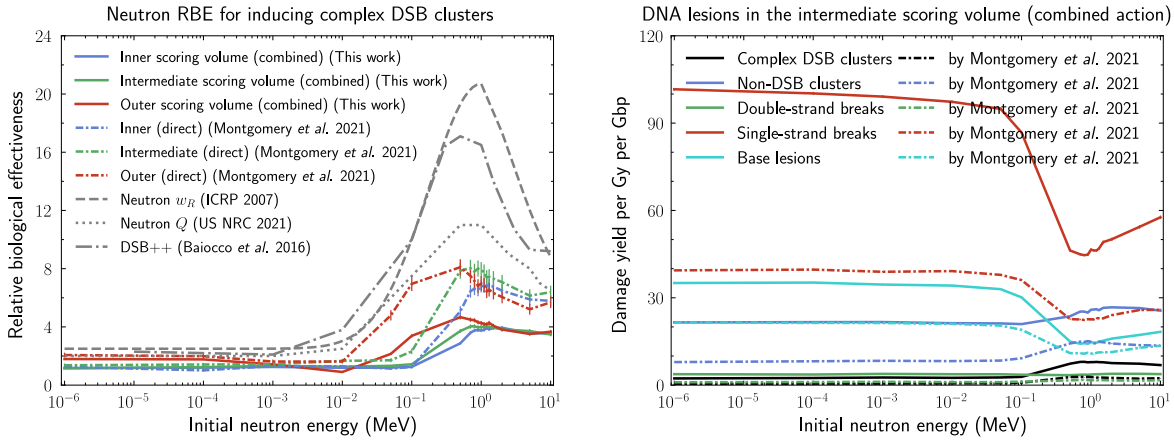


(a) (b)

Figure 6.10 (a) Neutron RBE for inducing C-DSBs via combined action in the various scoring volumes compared with various published results. (b) Neutron-induced DYs due to combined action in the intermediate scoring volume compared with those due to direct action alone by Montgomery *et al.* (2021) [8].

# Chapter 7

# Discussion

In this chapter, the significance of the results presented in the previous chapter are discussed. This chapter also explores the limitations of the project and offers suggestions for future developments based on the findings of our analyses.

## 7.1 Step 1: Code implementation

Similar to the TOPAS-CDD code [32] of Montgomery *et al.* (2021) [8], all the expansion code written for this thesis project (summarized in Section 6.1.1) is to be released open-source with updated TOPAS parameter text file examples and necessary documentation in support of open science and to allow other researchers to validate and possibly expand upon our work. This anticipated release will occur upon completion of the accompanying documentation and in conjunction with a manuscript submission to a scientific journal in the near future.

## 7.2 Step 2: Feature verification and model benchmarking

### 7.2.1 Verifying direct damage yields

The simulation results obtained by Montgomery *et al.* (2021) [8] were successfully replicated using our expanded code with the toggle for indirect action deactivated. Figure 6.2 demonstrates the statistical agreement between the results obtained in this study and the results of Montgomery *et al.* (2021) [8], for both DYs and neutron RBE for inducing C-DSBs. Although not shown, the DYs for the other scoring volumes and the RBE for inducing other damage types obtained

in our simulations were also consistent with the reference work. These results serve as evidence that our updates to the TOPAS-CDD application did not impact the original functionality.

### 7.2.2 Verifying multithreading functionality

As shown in Table 6.1, varying the number of threads did not have any significant effect on the DYs, which means that the direct and indirect DYs obtained from the independently simulated events across multiple worker threads were tallied properly as they were absorbed into the main thread. Table 6.1 also demonstrates the substantial improvement in the duration of the simulations using multithreading. Thus, the multithreading feature was deemed functional and appropriate for use in the remaining simulations with indirect action.

### 7.2.3 SSB and DSB yields comparison with published data

The comparisons in this section serve to validate and benchmark our simulation model. To facilitate our DY comparisons, Table 7.1 provides an inter-study comparison of the simulation parameters we believe to be most implicated in the induction of SBs.

#### Direct damage yields: notable trends

Given the agreement of our results (see Figure 6.2), it stands to reason that the results of the benchmarking analysis performed by Montgomery *et al.* (2021) [8] relevant to direct DYs apply equally well to this present work. In this section, we briefly discuss the key findings of Montgomery *et al.* (2021) [8] regarding the effect of various simulation parameters on direct DYs. We also provide relevant additional observations from the benchmarking of our direct DYs (see Figure 6.3).

A denser DNA model increases the likelihood of simulated particles to encounter sensitive DNA volumes, while a lower direct damage threshold permit lower energy depositions in DNA volumes to be counted as damage events. Thus, both lead to an increase in direct DYs [8]. This effect can be observed from the direct DYs of de la Fuentes Rosales *et al.* (2018) [4] that used the densest nuclear model and lowest direct damage threshold. The use of the linear damage probability from 1-37.5 eV has been shown to increase direct SSBs by about 40% compared to our fixed damage threshold of 17.5 eV [142, 184]. Hydration shells effectively increase sensitive DNA volumes and thus increase direct DYs [8]. Half of the cited work in

Table 7.1 A summary of key simulation parameters used in the publications cited in Figure 6.3 in comparison to our study. The references are partitioned according to simulation code used: PARTRAC, Geant4-DNA, and TOPAS-nBio (from top to bottom). Unless otherwise stated, each study effectively used the default physics and chemistry constructors of their respective simulation framework.

| Reference | Nucleus bp density (Mbp/$\mu$m$^3$) | DNA per nucleosome (kbp) | Direct damage threshold (eV) | $P_{.OH}$ | Chemical stage length (ns) |
|---|---|---|---|---|---|
| Friedland (2003) [138] | 6.8[a,b] | 16.7 | 5 – 37.5 | 0.7 | 10 |
| Meylan (2017) [141] | 8.7[b] | 0.22 | 17.5 | 0.4 | 2.5 |
| Rosales (2018) [4] | 170[a] | 0.15 | 8 | 0.65 | 1 |
| Sakata (2020) [144][c] | 12.1[b] | 0.19 | 5 – 37.5 | 0.405 | 5 |
| Zhu (2020) [30] | 14.4[b] | 0.20 | 17.5 | 0.4 | 1 |
| This work[c] | 13.3 | 0.15 | 17.5 | 0.4 | 1 |

[a] Atomistic DNA models. Unlabeled models are volumetric.
[b] Model has an implemented hydration shells.
[c] Model used opt2 and opt4 physics constructors.

Table 7.1 effectively used the opt2 physics constructor of Geant4 [30]. Compared to opt2, our hybrid constructor has been shown to increase direct DYs while preserving qualitative trends [8]. Lastly, taking competing factors into account, the significantly higher estimation of the direct DYs of Friendland *et al.* (2003) [138] in Figure 6.3-a compared to other simulations may be attributed to their model's significantly higher base pair count per nucleosome (see Table 7.1), which suggests that although their chromatin fibres are relatively disperse (hinted by the low nuclear DNA density or $\rho_{DNA}$), they incur significantly higher numbers of direct damage hits when direct action events occur. Therefore, it may be of value to consider DNA densities at the scale of secondary ionizing particle tracks (nano-scale) when building DNA models for simulated irradiation studies, instead of only looking at the full nuclear model (micro-scale).

### Indirect damage yields: general trends

For indirect lesions presented in Figure 6.3, SSB yields decrease more significantly with increasing LET compared with direct counterparts, while indirect DSB yields increase less and they eventually converge with direct DSB yields for $P_{.OH} = 0.40$. This convergence and the

consistent dominance of hybrid lesions can also be observed from the reference data in Figures 6.3-a, b, and d, but not with our results using $P_{\cdot OH} = 0.65$, hinting at a possible overestimation of indirect SBs using this damage probability. Indications of the eventual convergence of direct and indirect DYs can also be remarked in the SB and SSB yields, affirming our expectation that beyond some LET threshold, direct action becomes the dominant damage-inducing mechanism. Although indirect DYs greatly outnumber direct DYs in the lower LET domain, the relatively low proportion of indirect DSBs support the idea that indirect lesions are likely sporadically distributed. Denser ionizations of higher-LET radiation within the nucleus lead to radiolytic species that are generated in closer proximity with each other. This closer proximity serves to favor reactions between radiolytic species instead of their reactions with DNA moieties. As such, the observed diminishing indirect DNA DYs in Figures 6.3-a to c is expected.

Although our indirect SB and SSB yields using $P_{\cdot OH} = 0.65$ appear to be more consistent with other simulation data, our resulting proportion of indirect damage lesions for low-LET radiation using $P_{\cdot OH} = 0.40$, estimated to be $\lesssim$70% (see Figure 6.3-c), matches experimental estimates at around 65-71% [27, 59] (see Section 3.2.1). These estimates, however, are for the indirect action of all radiolytic species to the DNA. The value specific to ·OH radicals is estimated to be ∼62% [65] (see Section 3.2.3). This estimate is still consistent with our results but matches best with the estimates of Friedland *et al.* (2003) [138] and de la Fuentes Rosales *et al.* (2018) [4] in the low-LET domain of Figure 6.3-c.

#### Indirect damage yields: damage probability of ·OH radicals

Certainly, the higher the $P_{\cdot OH}$, the more indirect action events lead to DNA damage. As expected from increasing $P_{\cdot OH}$ from 0.40 to 0.65, our indirect DYs increased by ∼63% (which corresponds to an increase of ∼42% in total SB yields) as shown in Figure 6.3-a. These results are consistent with a parameter sensitivity analysis conducted by Zhu *et al.* (2020b) [184]. With the increased damage probability, ·OH radicals became much more likely to inflict damage immediately (i.e., diffuse shorter distances), which then leads to higher counts of spatially-dense SBs in the form of indirect DSBs, as shown in Figure 6.3-d.

#### Indirect damage yields: chemical stage duration, scavenging histones, and DNA density

The longer $T_{chem}$ is, the more indirect lesions accumulate. The parameter sensitivity analysis of Zhu *et al.* (2020b) [184] showed an increase of about 50% in indirect SB yields by increasing

$T_{chem}$ from 1 ns to 2.5 ns. Interestingly, the simulations of Friedland *et al.* (2003) [138] that used $P_{\cdot OH} = 0.7$ and a $T_{chem}$ of 10 ns, yielded the least indirect lesions (but the most direct lesions) among our comparison data (see Figure 6.3-a). A reasonable explanation on why the results of Friedland *et al.* (2003) [138] may have a relatively low indirect SB yield despite having a large $T_{chem}$ is that they used relatively large histone volumes ($\sim$380 nm$^3$ compared to our volume of $\sim$100 nm$^3$) designed to scavenge ·OH radicals (similar to our constraint 2). It has been shown that removing the scavenging properties of histone volumes can increase DYs by approximately 50% to 70% [144].

$\rho_{DNA}$ at the micro-scale has the same influence on direct and indirect DYs: a denser (and more homogeneous) nuclear DNA model increases the likelihood of damage events for IR and radiolytic species alike. This effect can be observed from the DYs of de la Fuentes Rosales *et al.* (2018) [4] in Figure 6.3-a. However, whereas the high nano-scale $\rho_{DNA}$ of the model of Friedland *et al.* (2003) [138] served to increase their direct DYs (discussed in Section 7.2.3), this is not the case with their indirect DYs. This is because simulated ionizing particles with enough energy are capable of traversing and damaging multiple DNA volumes (more lesions for DNA-denser nucleosomes), while simulated ·OH radicals (in their case and in ours) can only inflict damage once before getting terminated due to implemented DNA scavenging features (similar to our constraint 1). Again from Figure 6.3-a, we see a relative overestimation by Sakata *et al.* (2020) [144] that may be attributed to their nuclear DNA model that is not overly dense (most similar to the density of an actual human fibroblast cell), small scavenging histones ($\sim$65 nm$^3$), and 5 ns of $T_{chem}$.

**Indirect damage yields: histone distribution, "dead zones", and chemistry constructor**

Despite the significantly denser DNA model of de la Fuentes Rosales *et al.* (2018) [4] compared to other models, their indirect DYs remain in the same order of magnitude likely due to two counteracting effects: (i) scavenger histones that are also densely-distributed over the nucleus (i.e., more likely to encounter radiolytic species), and (ii) the implementation of "dead zones" inside DNA and histone volumes from which reactive molecules were forbidden to originate (similar to our constraint 3). By artificially terminating molecule tracks in these "dead zones", the number of reactive species that may induce indirect damage is essentially reduced.

As for the influence of chemistry model, de la Fuentes Rosales *et al.* (2018) [4] simulated more chemical species and reactions than other studies, but it is difficult to ascertain whether this led into more or less ·OH radicals. The indirect DYs of Zhu *et al.* (2020a) [30] from simulations

using a moderately dense DNA model and a chemistry model (`TsEmDNAChemistry`) that has been shown to increase indirect DYs by approximately 20% compared to `G4EmDNAChemistry` [184], were found to be comparable to those of Meylan *et al.* (2017) [141] that used a less denser DNA model with `G4EmDNAChemistry`. We suspect that the indirect DYs of Zhu *et al.* (2020a) [30] may have been impeded by their relatively large scavenging histones ($\sim$200 nm$^3$).

Our simulation scenario and DNA model most closely match those of Zhu *et al.* (2020a) [30], however our simulations yielded significantly less indirect damage counts despite our smaller scavenging histone volumes ($\sim$100 nm$^3$). We suspect this may be due to our implementation of "dead zones" that might have severely limited the occurrence of indirect damage events in our simulations. Although their group also reported a similar implementation, the indirect damage scorer code released with TOPAS-nBio version 1.0 was found to implement this feature incorrectly. This bug has been acknowledged since by J. Schuemann of the TOPAS-nBio collaboration when our group brought this anomaly to their attention (personal communication).

### Comparison of DSB yields

Although our DSB yields using $P_{\cdot OH} = 0.40$ appear lower than published simulated estimates with available damage-cause breakdown (see Figure 6.3), considering a larger set of *in silico* and *in vitro* results in Figure 6.4-a show that our DSB yields using $P_{\cdot OH} = 0.40$ are in agreement with previous work. In contrast, using $P_{\cdot OH} = 0.65$ resulted in total SB and SSB yields that are similar to reference work in Figure 6.3-a, but with apparently overestimated DSB counts. Given that DSBs are the key feature of our clustered lesion of interest (i.e., C-DSB clusters), our preference for $P_{\cdot OH} = 0.40$ in our neutron simulations (neutron RBE irradiation scenario) is justified. The various experimental results presented are of Belli *et al.* (2000, 2001) [179, 180] on V-79 Chinese hamster cells with $\rho_{DNA}$ $\sim$15 Mbp/$\mu$m$^3$ [144], and of Frankenberg *et al.* (1999) [178] and Campa *et al.* (2005) [181] on human skin cells with $\rho_{DNA}$ $\sim$12 Mbp/$\mu$m$^3$ [144]. The DSB estimations of Frankenberg *et al.* (1999) [178] and of Belli *et al.* (2001) [180] are similar to our DSB yields (as well as those of other simulation work), whereas those of Belli *et al.* (2000) [179] and Campa *et al.* (2005) [181] are lower than *in silico* yields.

### Comparison of SSB yield to DSB yield ratios

The quantity of SSB to DSB ratio describes how much more often SSBs occur relative to DSBs and can also be an indication of the spatial distribution of SSBs. If the SSBs tend to be close in

proximity, they are more likely to form DSBs and thus, decrease the SSB/DSB ratio. Our results in Figure 6.4-b show comparable SSB/DSB values with other publications (reporting both SSB and DSB values) except with those of Sakata *et al.* (2020) [144] who obtained relatively larger SSB yields (indirect SSBs specifically) than the other studies presented in Figure 6.3-a. The higher SSB/DSB ratios of our simulations using $P_{\cdot OH} = 0.40$ compared to those using $P_{\cdot OH} = 0.65$ support the notion that a higher damage probability result in more clustered DNA lesions (discussed in Section 7.2.3). Given the consistency of our DSB yields with most other *in silico* experiments and the comparable nature of our SSB/DSB ratios over the LET range considered, it follows that the amount of our SSB yields are reasonable.

### 7.2.4 The influence of doubly-damaged sites

The number of doubly-damaged sites (affected by both direct and indirect action) were counted because these sites could have inflated the SSB and DSB yields of our benchmarking irradiations (and yields of other types of damage had they been scored). Consistent with expectation, our values reported in Section 6.2.4 show that doubly-damaged sites account for a small amount of lesions relative to the total SB count. The marked increase of doubly-damaged site occurrence with higher LET was anticipated due to the more clustered nature of lesions.

## 7.3 Step 3: Neutron RBE estimation

### 7.3.1 Damage yields and RBEs across initial neutron energies

With increasing $E_0^{n^0}$, a pronounced decrease of SSB and BD yields was observed in all scoring volumes in Figure 6.5. The $E_0^{n^0}$ value where the decline begins ($\sim 10^{-3}$ MeV for the outer and $\sim 10^{-1}$ MeV for both intermediate and inner scoring volumes) is the energy around which the dominant contributor to neutron dose switches from electrons to protons, as demonstrated in the results of Lund *et al.* (2020) [7]. This energy is shown for the intermediate scoring volume near the crossover point between the blue and black curves in Figure 4.6-b. As anticipated, the increased dose contribution of higher-LET protons at higher $E_0^{n^0}$ around 1 MeV resulted in increased cluster formation (most notably in C-DSBs due to combined action in Figure 6.5) and decreased incidence of isolated lesions. The apparent constancy of simple DSB yields across

energy contrasted with the increase in C-DSB yields at higher $E_0^{n^0}$ suggest that when DSBs occur at these energies, they are likely accompanied by other lesions, thereby forming C-DSBs.

The RBE curves in Figure 6.6 are the DYs in Figure 6.5 but divided by the corresponding DYs of 250 keV reference X-rays. All RBE curves for C-DSB cluster induction have a remarkable surge at higher $E_0^{n^0}$ followed by a slight decline. This RBE surge is an indication of the increased clustering of lesions due to the presence of higher-LET particles described earlier. On the other hand, the ensuing RBE decrease matches the $E_0^{n^0}$ range where the yields of simple lesions increase in Figure 6.5, both of which are indications of an elevated influence of low-LET radiation. Although protons are still the primary dose contributors at higher $E_0^{n^0}$ where these declines occur [7], higher-energy protons at this range actually correspond to lower-LET particles as we have seen in Step 2. In Figures 6.6-a1 and a2, a minimum in neutron RBE for inducing C-DSBs in the outer scoring volume at $E_0^{n^0}$ around $10^{-3}$-$10^{-2}$ MeV may be observed. Given that this minimum coincides with the significant decrease in simple lesions in Figure 6.5, and is much more pronounced in the case where only indirect lesions were considered, we suspect the cause to be the tapering off of electron dose contribution in this $E_0^{n^0}$ range, with the proton dose contribution remaining relatively low [7]. In our simulations, this phenomenon likely manifested as a substantial decrease in electron histories, but only an increase of a few proton histories that delivered dose but did not induce much lesions.

### 7.3.2 Damage yields and RBEs across depth

As we go deeper from the outer to the inner scoring volume, we observe that the trends discussed in the previous section are shifted towards higher $E_0^{n^0}$. From the outer to the inner region, we see an increase in SSB and BD yields, a slight decrease in C-DSB counts, and a slight decrease and apparent flattening of N-DSB yields. The DSB counts appear constant across depth. Higher-energy neutrons have higher penetrating capabilities due to lower neutron capture cross-sections, and are capable of liberating higher-energy protons and higher-energy $\gamma$-rays that can trigger a greater number of tertiary electron emissions. Thus, at deeper regions, we expect an increased presence of low-LET particles with sparsely-distributed ionizations (i.e., low likelihood of cluster formation). Indeed, this phenomenon manifests in Figure 6.5 as the remarked increasing amounts of simple lesions yet decreasing amounts of clustered lesions from the outer towards the inner scoring volume.

Since the only secondary particles of our reference X-rays are electrons, we generally expected them to induce more basic lesions than clustered ones as compared to neutrons. Our resulting neutron RBE curves are in agreement with this expectation in that RBE values corresponding to clustered lesions are mostly >1,while those corresponding to isolated lesions are consistently <1. The qualitative trends in RBE closely follow those of their respective DYs. The slight trends in C-DSB yields become magnified in the RBE domain. The elevated neutron RBE levels for inducing C-DSBs even at lower $E_0^{n^0}$ in the outer scoring volume is indicative of the relatively high proton dose contribution in this region compared to the deeper scoring volumes [7].

### 7.3.3 Damage yields and RBEs across damage type

The damage conditions of SSBs and BDs in our simulations were similar for both direct (energy deposition of 17.5 eV) and indirect action (·OH interaction damage probability of 0.4). However, $\frac{4}{6}$ volumes in our nucleotide base pair model are subject to a SSB event, whereas only $\frac{2}{6}$ volumes can lead to a BD. We thus expected the amount of SSB yields to be about twice as much that of BD yields, and this was indeed demonstrated in our direct DYs in Figure 6.2-a. However, in the case of indirect DYs alone, we see in Figure 6.5 that SSB yields consistently dominate BD yields by approximately three times. This difference likely stems from the fact that ·OH tracks are terminated upon interaction with a DNA volume (constraint 1), and are thus likely to only damage topologically accessible target volumes, unlike ionizing particles that can traverse and damage multiple ones. Simply put, SSBs were favored over BDs primarily due to the higher abundance of sugar-phosphate volumes and their increased exposure to ·OH species due to the coiling of our DNA model.

The presence of alpha radiation at $E_0^{n^0}$ of 5 MeV and 10 MeV does not seem to have a detectable signature in clustered DYs, likely due to its relatively low dose contribution compared to protons that already have relatively high LET. The fact that our DYs count no more than 100 per Gy per $10^9$ bp reveals the rarity of radiation-induced DNA damage.

### 7.3.4 Damage yields and RBEs: indirect action alone vs. combined action

Going from DYs caused by independent indirect action to those caused by the combined effects of direct and indirect action in Figure 6.5, we observe an expected overall increase in counts

due to the inclusion of the damage contribution of direct action. In general, the trends of the different damage types in the case of indirect action alone are less pronounced than those found in the case of combined action, but are mostly still detectable. This similarity in DY trends highlights the influence of indirect action in neutron radiation. A significant presence of C-DSB clusters can only be found in the DYs due to combined action (at higher $E_0^{n^0}$), indicating that the great majority of these clustered lesions are due to the direct action of higher-LET particles. The points of significant decline in SSB and BD yields match with the increase in N-DSB (and C-DSB in the case of combined action) cluster yields, which hints at the grouping of simple lesions into clusters (aside from the already expected decrease in occurrence of indirect lesions due to the dominant proton influence) at higher $E_0^{n^0}$ values.

The neutron RBE for inducing simple lesions across damage-inducing action in Figure 6.6 was found to be similar, but RBE values corresponding to DSBs, N-DSBs, and C-DSBs were counter-intuitively found to be more pronounced if only indirect lesions were considered. Despite the higher incidence of these types of damages in the case of combined action, we observe a decrease in corresponding RBE, which means that the relative increase in clustered DYs of 250 keV X-rays is greater than those of neutrons when direct lesions are considered. This is possible considering the more clustered nature of neutron-induced DNA damage that may result in more lesions being counted into a single cluster, thereby limiting the absolute increase in total counts of C-DSB clusters. The larger uncertainties of neutron RBE values related to C-DSBs in the case of independent indirect action indicate the larger fluctuations of C-DSB cluster formation across independent simulation runs. The similar energy range at which the RBE for C-DSBs peak for both action cases suggests that the composition of neutron secondary particles around this energy range provide maximum LET that then maximizes the clustering potential of the inflicted lesions.

### 7.3.5 Damage contributions in combined action

Figure 6.7 presents a breakdown of the combined action DYs for all types of DNA damage from Figure 6.5-b2, in terms of the contributions of direct, indirect, and hybrid lesions. The difference between DYs due to combined action and hybrid lesions is depicted in Figure 7.1-b. For SSBs and BDs in Figures 6.7-a and b, we observe greater counts of indirect lesions due to their tendency to be sparsely distributed. For DSBs in Figure 6.7-d, there is a comparable proportion of indirect and hybrid damages that both dominate direct DSB yields. This demonstrates that

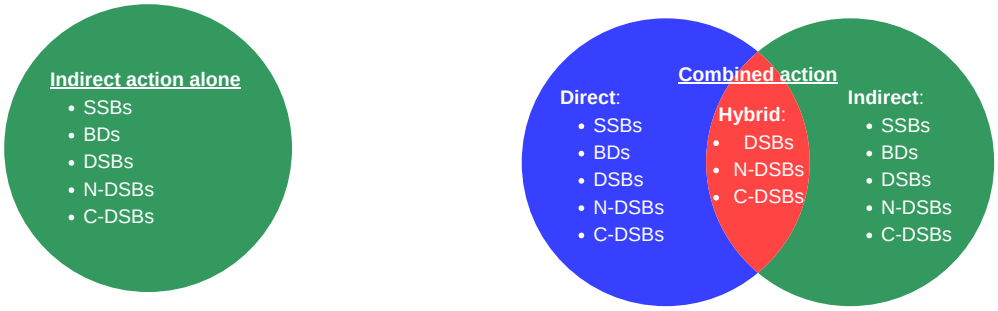


(a) (b)

Figure 7.1 Diagram showing the difference between lesions included in the case of (a) indirect action alone and (b) combined action.

even though direct lesions are likely to be more clustered (see Figure 6.7-e), the sheer amount of indirect SBs and the immediate formation of indirect lesions around direct ones are important factors in DSB formation. In Figures 6.7-c and e, we see the clear effect of combined action in clustered damage formation from the dominant counts of hybrid N-DSBs and C-DSBs. Additional N-DSBs due to independent direct and indirect action appear comparable with each other (with one type slightly dominating the other in expected energy regions).

From the neutron RBE plots in Figure 6.8, we observe a similar effectiveness of direct and indirect action in inflicting SSBs and BDs. For DSBs and clustered lesions (see Figures 6.8-c to e), we see the bias towards direct action at higher $E_0^{n^0}$ (the opposite effect for indirect action). The comparability of hybrid RBE to total RBE suggests that in the case of combined action, considering only hybrid damages may be sufficient to predict total RBE. It is important to note that the indirect component presented in Figure 6.8-e is only that of the neutron RBE for C-DSB induction in Figure 6.5-b2 (only the green portion in Figure 7.1-b), and is thus smaller than the analogous RBE in Figure 6.8-b1 (all of the green portion in Figure 7.1-a). In the case of combined action, some of the damages induced separately by direct and indirect action are counted as hybrid lesions. Thus, the indirect component of combined action has less DYs (and corresponding RBE) compared to the case of indirect action alone.

## 7.4 Step 4: Neutron RBE comparisons

### 7.4.1 Indirect action alone

In Figure 6.9-a, we see that the RBE of neutron indirect action for inducing C-DSB clusters fall below that of neutron direct action by both Baiocco *et al.* (2016) [6] and Montgomery *et al.* (2021) [8]. This was anticipated given the higher tendency of direct damage lesions to form clusters as explored in Step 2. This tendency can also be seen in the comparison between the different DYs of independent direct and indirect action in Figure 6.9-b where indirect lesions are greater in numbers for SSBs and BDs, while direct action, particularly around 1 MeV where we suspect the effective neutron LET to be maximized, resulted in more N-DSBs and C-DSBs. Indirect DSBs outnumber direct DSBs by about two times, which is the same ratio as their SSB counts in the lower energy domain. Similar to observations in Section 3, our RBE peaks match those of Montgomery *et al.* (2021) [8] that only considered direct action, supporting the idea that the observed maximum clustering of DNA lesions is due to the maximum effective LET of monoenergetic neutrons. Our RBE curves related to indirect C-DSBs also fall below the ICRP and US NRC neutron factors.

### 7.4.2 Combined action

Considering the combined effects of direct and indirect action, we once again see the lower neutron RBE values for inducing C-DSB clusters for all scoring volumes compared to homologous RBE curves due to independent direct (and indirect) action (see Figure 6.10-a). Our RBE values for the different scoring volumes appear to converge at around the RBE value of $\lesssim 4$ with little decrease from their respective peaks. Looking at differences in DYs in Figure 6.10-b, however, we see that C-DSB cluster yields due to combined action substantially outnumber those due to direct action only. Thus, similar to our earlier reasoning in Step 3, we suspect that the consistent relative underestimation of our neutron RBE values compared to cited references is primarily due to the even more clustering of DNA lesions due to combined action (compared to direct action alone) that results in more lesions per cluster, but less relative increase of cluster count compared to 250 keV X-rays. Assuming this is the case, C-DSBs due to combined action are potentially more difficult to repair due to the increased density of lesions that include DSBs, and correspondingly may be more likely to result in mutagenesis. However, in contrast, looking

at RBE alone for inducing C-DSBs, it would appear that direct action alone is more detrimental than combined action.

We suspect that using a biological endpoint or developing a metric that combines the information of C-DSB cluster counts and density of lesions per cluster may provide better insight regarding the relative mutagenic (and carcinogenic) effectiveness of the combined action of neutrons. Such factors, along with a simulated model for DNA repair that would theoretically reduce DYs, must be incorporated in future developments before drawing any firm conclusions about how clustered DNA damage may lead to macroscopic stochastic effects encapsulated by the ICRP and US NRC neutron radiation protection factors.

## 7.5 Limitations and future work

### 7.5.1 Physical factors

Given that this project used the same physics constructor as the work of Montgomery *et al.* (2021) [8], it follows that this present work inherits the limitations in physical modeling of the previous work. These limiting physical factors raised in the previous work include (i) the limited variety of simulated IR species (only electrons, protons, and alpha particles) and the non-inclusion of heavy ions such as oxygen and carbon that offer substantial contribution to neutron dose [7] and (ii) the capping of electron simulations at 1 MeV due to the opt2 physics model of Geant4 (secondary electrons generated with higher energies were considered as uncorrelated lower energy tracks). Once these heavier ions and higher energy electrons become available in Geant4 and TOPAS, likely in a new physics constructor, updating our simulation parameter files to import this new constructor would be relatively simple via the TOPAS parameter file system [8].

### 7.5.2 Chemical factors

As for the chemistry part, our simulations only considered seven chemical species (see Table 5.3). Future work regarding this subject involves using the extended chemistry constructor available in TOPAS-nBio (`TsEmDNAChemistryExtended`), which offers four more species: $HO_2\cdot$, $HO_2^-$, $O_2$, and $O_2\cdot^-$. Oxygen species are of particular interest because their presence

have been demonstrated to influence the detrimental effects of radiation-induced indirect DNA damage [65], often measured via a metric known as oxygen enhancement ratio (OER).

In our simulations, only ·OH radicals were considered to induce SSBs (similar to previously-published studies) and BDs, and the set probability of damage induction for both lesion types was 40%. From cited values in Sections 3.2.1 and 3.2.3, we can estimate that about 3-9% of radiation-induced DNA lesions in the low-LET domain are due to indirect action by non-·OH reactive species. Moreover, from Section 3.2.3, we know that about 80-90% of ·OH interactions with the DNA molecule involve a nucleobase [63]. Thus, it would be interesting to explore the effect in overall DYs of simulating the damaging effects of other radiolytic products and increasing $P_{\cdot OH}^{nucleobase}$ to favor BD yields.

Another chemistry-related limitation of our simulations is that the simulated chemical species were assumed to propagate in pure liquid water at neutral pH and 25°C [13]. Indeed, cells are not made of pure water as seen in Section 3.1.4, intracellular pH ranges from 4.5-8.0 depending on the cell organelle [185, 186], and the normal human body temperature is around 36-37°C [187]. There are currently no chemistry models in Geant4-DNA or TOPAS-nBio accounting for these factors, thus their various effects on DNA DYs and RBE are difficult to ascertain. Again, once such models become available, implementing them in our simulations is a matter of editing our TOPAS parameter files.

### 7.5.3 Biological factors

Due to the same DNA model used, the limitations related to the DNA model discussed in the work of Montgomery *et al.* (2021) [8] apply in this present work. The nucleus of a human fibroblast is generally ellipsoidal in shape [155], but was modeled as cubic in our simulations. Despite this inaccuracy, the size of our sensitive DNA volumes and the $\rho_{DNA}$ of our model, factors we have seen to be of high importance in Step 2, were sufficiently realistic.

Another limitation of our DNA model came in the form of disjoints between adjacent chromatin fibres which entailed the non-trivial union of neighboring damage clusters from different fibres. As such, our DNA damage clustering was limited to lesions in the same fibre. However, the parameter sensitivity analysis performed by Montgomery *et al.* (2021) [8] using our DNA model showed that the mean length of direct damage clusters was approximately 10 bp. Although a similar analysis was not performed in this work for indirect and combined action, the rare occurrence of DNA lesions (in the order of $10^3$ per Gy of irradiation compared

to the total base pair count of about $6.3 \times 10^9$) suggests that these fibre disjoints likely did not have any significant effect in the clustering of our simulated DYs [8].

Lastly, we did not simulate DNA repair mechanisms and the non-targeted effects of IR (RIBEs and RIGI) in this present work. Repair models implemented in TOPAS-nBio that came with the latest version would likely be considered in future developments of this project. Given that RIBEs would require the simulation of multiple cells and RIGI, the simulation of cellular reproduction, the inclusion of sophisticated models for these effects in this project would likely occur much further into the future.

### 7.5.4 Other important factors to consider

Similar to the parameter sensitivity analysis performed by Montgomery *et al.* (2021) [8] for direct action only, we can investigate the effects of modifying factors such as dose delivered and cluster length in DNA DYs and neutron RBE. A study similar to that of Zhu *et al.* (2020b) [184] that looked into the effects of physics and chemistry constructors, $T_{chem}$, and indirect damage probability may also be accomplished for neutron irradiations instead of protons (the effect of changing $P_{OH}$ has been explored in this project but only using monoenergetic protons). Such kind of analysis may also be extended to the several modifiable parameters (see Figure 6.1) of our indirect action simulations.

Although we cannot easily modify our DNA model, we would be able to determine the relative effects of implementing "dead zones", and the radical scavenging of DNA molecules and histones by adjusting constraints 1 to 3 via the parameter file. Isolating the effect of these constraints might allow us to shed better light on the effect of nano-scale and micro-scale $\rho_{DNA}$ on direct and indirect DNA damage, which could guide future standardization efforts in constructing and using DNA models in the context of simulated irradiations.

Indeed, having estimated values of the effective LET of monoenergetic neutrons will further solidify our findings of where the peak RBE for inducing C-DSB clusters occurs in the energy range considered. Lastly, as mentioned earlier, further expansion of this project involves inspecting the density of DNA lesions in cluster formations to better quantify the mutagenic and carcinogenic properties of the combined effects of direct and indirect action of neutrons. A similar analysis has already been performed for neutron direct action by Montgomery *et al.* (2021) [8] and thus, our group has an existing procedure that will facilitate the extension of this analysis to neutron combined action.

# Chapter 8

# Summary and Conclusions

Neutrons are ionizing particles associated with elevated biological risk [10, 11]. In this thesis project, we have explored the risk of iatrogenic second cancer emergence due to the whole-body and non-therapeutic secondary neutron exposure of patients undergoing high-energy photon EBRT. Although this dose is insufficient to cause immediate observable effects, damage to the DNA inflicted by these neutrons may lead to mutations that can accumulate over long periods of time and transform a healthy cell into a detrimental neoplasm. Our investigation centered around the capacity of neutrons to induce difficult-to-repair clustered DNA lesions, which is widely believed to be a main pathway by which radiation-induced mutagenesis occurs. More specifically, our study focused on determining the role of indirect action (demonstrated to be a significant damage-inflicting mechanism in our energy range of interest [27–29]) in neutron-induced clustered DNA damage formation. To quantify related carcinogenic risk, we used the RBE of neutrons for inducing such lesions compared to 250 keV X-rays. Building upon previous work by our research group [7, 8], our investigations were performed using condensed-history and track-structure Monte Carlo simulations of neutrons irradiating a geometric DNA model. The methods undertaken in this thesis project consisted of four distinct steps.

Step 1 aimed to expand the existing simulation code of our group for direct action (TOPAS-CDD [32]) to account for indirect action as well. Here, the direct damage scorer of Montgomery *et al*. (2021) [8] was updated to track indirect action and damage events in a simulation geometry that was rendered in a chemically-realistic manner by applying constraints in the chemical stage. The DNA damage clustering algorithm in this scorer code was also extended to distinguish new classes of damages emerging from indirect action and the combined effects of direct and indirect action (referred to as combined action in this work). The expansion of the

TOPAS-CDD code was written in the TOPAS format to allow users to easily configure their simulation parameters. This configurability and the implemented multithreading feature serve to facilitate future developments of the project.

Step 2 involved (i) the verification of the functionality of our new simulation features and (ii) the validation and benchmarking of our indirect action simulations and damage scoring via DY comparison with previous work using monoenergetic proton irradiations. Our simulations tended to underestimate the amount of indirect SB yields compared to published data [4, 30, 138, 141, 144]. However, we deemed our implementation to be justified given that (i) our DYs are quantitatively comparable (in terms of order of magnitude) and qualitatively similar (in terms of exhibited trends) to published data, (ii) our estimated indirect and direct damage contributions of approximately 70% and 30% respectively match experimental data [27, 59], and (iii) our experimentally validated [178, 180] DSB counts and SSB/DSB yields ratio were found to be consistent with other simulation results. In our comparison analysis, we found that predicting quantitative differences in DNA DYs of simulated irradiations using easily-configurable simulation parameters (such as direct damage energy thresholds and indirect damage probabilities of radicals) is generally feasible given their demonstrated influence in direct and indirect action [184]. Although the track-killing capabilities of DNA and histone volumes, and the innate geometric properties of DNA models such as their nuclear (micro-scale) and nucleosomal (nano-scale) DNA densities may be used to qualitatively explain apparent inconsistencies in DYs across different simulation models, it remains difficult to accurately estimate their independent influence because of multiple competing factors in simulation scenarios (from the lack of model standardization in the field).

In step 3, our geometric DNA model was irradiated with particle tracks that were stochastically sampled from neutron-induced secondary particle spectra in human tissue at varying depths. This step aimed to quantify the neutron-induced carcinogenic risk of indirect action alone and combined action, via the estimation of their corresponding RBE for inducing DSB-containing clustered lesions (i.e., C-DSBs). Our simulation results showed that the majority of the DYs from neutron combined action are sparsely-distributed simple lesions due to indirect action. Significant formation of clustered lesions were found to emerge once direct action was considered and these lesions were mostly hybrid in nature. Our DYs also revealed that sporadic simple lesions were most prominent at $E_0^{n^0} \lesssim 100$ keV where the dominant dose-contributing particles are low-LET electrons [7], while the formation of clustered lesions correlated with the presence of high-LET protons for $E_0^{n^0} > 100$ keV [7]. Our calculated energy-dependent RBE

values for neutron indirect action alone to induce C-DSB clusters (peaking at around 4.5 to $\lesssim$6) were found to be greater than those of neutron combined action (peaking at around 4 to <5), despite the significantly higher C-DSB cluster counts due to combined action. The notable RBE peaks occur for both indirect and combined action at $E_0^{n^0}$ between 500 keV and 2 MeV (increasing with depth), followed by a slight decrease that we attributed to the decrease in LET of dose-dominant higher-energy protons.

Lastly, Step 4 took the neutron RBE curves for inducing C-DSB clusters obtained in Step 3 to evaluate the neutron-induced carcinogenic risk of indirect action and combined action by comparison with related RBE curves of Montgomery *et al*. (2021) [8] and Baiocco *et al*. (2016) [6] that only considered direct action, and the ICRP neutron radiation weighting factors [10] and US NRC neutron quality factors [11] that serve to quantify the risk associated with the stochastic effects of neutron radiation. We found that the peaks of our RBE curves (for both indirect and combined action) occurred at $E_0^{n^0}$ values that are in agreement with those of Montgomery *et al*. (2021) [8], suggesting that the composition of the dose-inducing secondary particles at such $E_0^{n^0}$ values give a maximum effective LET. Our RBE curves for indirect action alone were found to be lower than those of Montgomery *et al*. (2021) [8] and Baiocco *et al*. (2016) [6] (both already lower than the ICRP and US NRC neutron risk curves respectively) as expected due to the clustering proclivity of direct lesions. Again, our RBE curves for combined action were found to be even lower compared to direct counterparts despite the former's significant dominance in yields of C-DSB clusters.

To conclude, the DYs obtained from our validated neutron irradiation simulations show that indirect action significantly amplifies the ability of direct action to inflict clusters of DNA lesions believed to be majorly implicated in the emergence of radiation-induced malignancies. Although our neutron RBE results suggest that independent direct and indirect action are both more effective in inflicting C-DSB clusters than combined action, their respective clustered DYs (which instead measure absolute effectiveness) suggest otherwise. We suspect that this was due to a substantial increase in lesion density of the damage clusters inflicted by combined action which limited the overall increase in C-DSB cluster yields. Thus, a more appropriate representation of neutron RBE, and by extension, neutron-induced mutagenic and carcinogenic risk, would likely be achieved using a metric that factors in both C-DSB induction rate and lesion density per cluster. Finally, the inclusion of oxygen species, DNA repair mechanisms, and neutron-induced non-targeted effects (RIBEs and RIGI) in the simulations would likely provide a more complete representation of the actual carcinogenic risk of neutrons.

# References


[1] H. Patrick, "Development of a dvh registry for plan evaluation, dose accumulation, and cohort analysis," Master's thesis, McGill University, 2018.

[2] L. Montgomery, "Spectral measurements and carcinogenic effects modeling of secondary neutrons in radiation therapy," Ph.D. dissertation, McGill University, 2021.

[3] Lumen, "Microbiology." [Online]. Available: https://courses.lumenlearning.com/microbiology/chapter/structure-and-function-of-dna/

[4] L. D. L. F. Rosales, S. Incerti, Z. Francis, and M. A. Bernal, "Accounting for radiation-induced indirect damage on dna with the geant 4-dna code," *Physica Medica*, vol. 51, p. 108–116, 2018.

[5] D. R. White, J. Booz, R. V. Griffith, J. J. Spokas, and I. J. Wilson, "Report 44," *Journal of the International Commission on Radiation Units and Measurements*, vol. os23, no. 1, 1989.

[6] G. Baiocco, S. Barbieri, G. Babini, J. Morini, D. Alloni, W. Friedland, P. Kundrát, E. Schmitt, M. Puchalska, L. Sihver, and et al., "The origin of neutron biological effectiveness as a function of energy," *Scientific Reports*, vol. 6, no. 1, 2016.

[7] C. Lund, G. Famulari, L. Montgomery, and J. Kildea, "A microdosimetric analysis of the interactions of mono-energetic neutrons with human tissue," *Physica Medica*, vol. 73, p. 29–42, 2020.

[8] L. Montgomery, C. M. Lund, A. Landry, and J. Kildea, "Towards the characterization of neutron carcinogenesis through direct action simulations of clustered dna damage," *Physics in Medicine  Biology*, 2021. [Online]. Available: http://iopscience.iop.org/article/10.1088/1361-6560/ac2998

[9] E. B. Podgoršak, *Radiation Physics for Medical Physicists*. Springer International Publishing, 2016.

[10] ICRP, "ICRP Publication 103: The 2007 recommendations of the International Commission on Radiological Protection," *Annals of the ICRP*, vol. 37, no. 2-4, 2007.

[11] USNRC, "Units of radiation dose," *Code of Federal Regulations*, vol. 10, no. 20.1004, p. 298–300, 2021.

[12] I. Plante, "Radiation chemistry and oxidative stress," 2010. [Online]. Available: https://three.jsc.nasa.gov/multimedia/RadiationChemistry2.pdf

[13] J. Ramos-Méndez, J. Perl, J. Schuemann, A. McNamara, H. Paganetti, and B. Faddegon, "Monte carlo simulation of chemistry following radiolysis with topas-nbio," *Physics in Medicine amp; Biology*, vol. 63, no. 10, p. 105014, 2018.

[14] S. Incerti, A. Ivanchenko, M. Karamitros, A. Mantero, P. Moretto, H. N. Tran, B. Mascialino, C. Champion, V. N. Ivanchenko, M. A. Bernal, and et al., "Comparison of geant4 very low energy cross section models with experimental data in water," *Medical Physics*, vol. 37, no. 9, p. 4692–4708, 2010.

[15] S. Incerti, M. Douglass, S. Penfold, S. Guatelli, and E. Bezak, "Review of geant4-dna applications for micro and nanoscale simulations," *Physica Medica*, vol. 32, no. 10, p. 1187–1200, 2016.

[16] M. Karamitros, A. Mantero, S. Incerti, W. Friedland, G. Baldacchino, P. Barberet, M. Bernal, R. Capra, C. Champion, Z. E. Bitar, and et al., "Modeling radiation chemistry in the geant4 toolkit," *Progress in Nuclear Science and Technology*, vol. 2, p. 503–508, 2011.

[17] M. Rubio, L. Serrano-Andrés, and M. Merchán, "Excited states of the water molecule: Analysis of the valence and rydberg character," *The Journal of Chemical Physics*, vol. 128, no. 10, p. 104305, 2008.

[18] C. C. Society, "Cancer statistics." [Online]. Available: https://cancer.ca/en/research/cancer-statistics

[19] ——, "Cancer statistics at a glance." [Online]. Available: https://cancer.ca/en/research/cancer-statistics/cancer-statistics-at-a-glance

[20] L. M. Morton, K. Onel, R. E. Curtis, E. A. Hungate, and G. T. Armstrong, "The rising incidence of second cancers: Patterns of occurrence and identification of risk factors for children and adults," *American Society of Clinical Oncology Educational Book*, no. 34, 2014.

[21] D. Hanahan and R. A. Weinberg, "Hallmarks of cancer: The next generation," *Cell*, vol. 144, no. 5, p. 646–674, 2011.

[22] M. B. Barton, S. Jacob, J. Shafiq, K. Wong, S. R. Thompson, T. P. Hanna, and G. P. Delaney, "Estimating the demand for radiotherapy from the evidence: A review of changes from 2003 to 2012," *Radiotherapy and Oncology*, vol. 112, no. 1, p. 140–144, 2014.

[23] F. M. Khan and J. P. Gibbons, *Khans the Physics of Radiation Therapy (5th Edition)*. LWW (PE), 2014.

[24] H. Owen, A. Lomax, and S. Jolly, "Current and future accelerator technologies for charged particle therapy," *Nuclear Instruments and Methods in Physics Research Section A: Accelerators, Spectrometers, Detectors and Associated Equipment*, vol. 809, p. 96–104, 2016.

[25] T. Grantzau and J. Overgaard, "Risk of second non-breast cancer after radiotherapy for breast cancer: A systematic review and meta-analysis of 762,468 patients," *Radiotherapy and Oncology*, vol. 114, no. 1, p. 56–65, 2015.

[26] S. F. Kry, B. Bednarz, R. M. Howell, L. Dauer, D. Followill, E. Klein, H. Paganetti, B. Wang, C.-S. Wuu, X. G. Xu, and et al., "Aapm tg 158: Measurement and calculation of doses outside the treated volume from external-beam radiation therapy," *Medical Physics*, vol. 44, no. 10, 2017.

[27] R. Roots and S. Okada, "Estimation of life times and diffusion distances of radicals involved in x-ray-induced dna strand breaks or killing of mammalian cells," *Radiation Research*, vol. 64, no. 2, p. 306, 1975.

[28] R. Roots, A. Chatterjee, P. Chang, L. Lommel, and E. Blakely, "Characterization of hydroxyl radical-induced damage after sparsely and densely ionizing irradiation," *International Journal of Radiation Biology and Related Studies in Physics, Chemistry and Medicine*, vol. 47, no. 2, p. 157–166, 1985.

[29] A. Ito, H. Nakano, Y. Kusano, R. Hirayama, Y. Furusawa, C. Murayama, T. Mori, Y. Katsumura, and K. Shinohara, "Contribution of indirect action to radiation-induced mammalian cell inactivation: Dependence on photon energy and heavy-ion let," *Radiation Research*, vol. 165, no. 6, p. 703–712, 2006.

[30] H. Zhu, A. L. Mcnamara, S. J. Mcmahon, J. Ramos-Mendez, N. T. Henthorn, B. Faddegon, K. D. Held, J. Perl, J. Li, H. Paganetti, and et al., "Cellular response to proton irradiation: A simulation study with topas-nbio," *Radiation Research*, vol. 194, no. 1, p. 9, 2020.

[31] X. Zhao, R. Liu, T. Zhao, and F. J. Reynoso, "Modeling double-strand breaks from direct and indirect action in a complete human genome single cell geant4 model," *Biomedical Physics  Engineering Express*, vol. 6, no. 6, p. 065010, 2020.

[32] L. Montgomery, C. M. Lund, J. Manalad, A. Landry, , and J. Kildea, "Topas clustered dna damage," *GitHub repository*, 2021. [Online]. Available: https://doi.org/10.5281/zenodo.5090104

[33] E. M. A. Hussein, *Radiation mechanics: principles and practice*. Elsevier, 2007.

[34] K. H. Beckhurts and K. Wirtz, *Neutron Physics*. Springer-Verlag Berlin Heidelberg, 1964.

[35] T. C. S. E. W. Group, "Report bnl-ncs-44945," Tech. Rep., 1995.

[36] I. Shuryak, A. J. Fornace, K. Datta, S. Suman, S. Kumar, R. K. Sachs, and D. J. Brenner, "Scaling human cancer risks from low let to high let when dose-effect relationships are complex," *Radiation Research*, vol. 187, no. 4, p. 486–492, 2017.

[37] ICRP, "ICRP 92: Relative Biological Effectiveness (RBE), Quality Factor (Q), and Radiation Weighting Factor (wR)," *Annals of the ICRP*, vol. 33, no. 4, 2003.

[38] ——, "ICRP 60: The 1990 Recommendations of the International Commission on Radiological Protection," *Annals of the ICRP*, vol. 21, no. 1-3, 1991.

[39] E. J. Hall and A. J. Giaccia, *Radiobiology for the radiologist*. Wolters Kluwer Health/Lippincott Williams Wilkins, 2012.

[40] M. M. Greenberg, "Reactivity of nucleic acid radicals," *Advances in Physical Organic Chemistry*, p. 119–202, 2016.

[41] P. F. Little, "Structure and function of the human genome," *Genome Research*, vol. 15, no. 12, p. 1759–1766, 2005.

[42] A. Annunziato, "Dna packaging: Nucleosomes and chromatin," 2008. [Online]. Available: https://www.nature.com/scitable/topicpage/dna-packaging-nucleosomes-and-chromatin-310/

[43] T. D. Pollard, W. C. Earnshaw, J. Lippincott-Schwartz, and G. T. Johnson, *Cell biology*. Elsevier, 2017.

[44] G. Elgar and T. Vavouri, "Tuning in to the signals: noncoding sequence conservation in vertebrate genomes," *Trends in Genetics*, vol. 24, no. 7, p. 344–352, 2008.

[45] E. Perenthaler, S. Yousefi, E. Niggl, and T. S. Barakat, "Beyond the exome: The noncoding genome and enhancers in neurodevelopmental disorders and malformations of cortical development," *Frontiers in Cellular Neuroscience*, vol. 13, 2019.

[46] B. A. Pierce, *Genetics: a conceptual approach*. W.H. Freeman, 2012.

[47] R. D. Bont, "Endogenous dna damage in humans: a review of quantitative data," *Mutagenesis*, vol. 19, no. 3, p. 169–185, 2004.

[48] L. J. Marnett, "Oxyradicals and dna damage," *Carcinogenesis*, vol. 21, no. 3, p. 361–370, 2000.

[49] B. Alberts, A. Johnson, and J. Lewis, *Molecular biology of the cell*. Garland Science, 2002.

[50] A. L. Jackson and L. A. Loeb, "The contribution of endogenous sources of dna damage to the multiple mutations in cancer," *Mutation Research/Fundamental and Molecular Mechanisms of Mutagenesis*, vol. 477, no. 1-2, p. 7–21, 2001.

[51] L. A. Rowe, N. Degtyareva, and P. W. Doetsch, "Dna damage-induced reactive oxygen species (ros) stress response in saccharomyces cerevisiae," *Free Radical Biology and Medicine*, vol. 45, no. 8, p. 1167–1177, 2008.

[52] K. Magnander and K. Elmroth, "Biological consequences of formation and repair of complex dna damage," *Cancer Letters*, vol. 327, no. 1-2, p. 90–96, 2012.

[53] A. G. Georgakilas, P. Oneill, and R. D. Stewart, "Induction and repair of clustered dna lesions: What do we know so far?" *Radiation Research*, vol. 180, no. 1, p. 100–109, 2013.

[54] J. G. Bazan, Q.-T. Le, and D. Zips, "Radiobiology of lung cancer," *IASLC Thoracic Oncology*, 2018.

[55] B. N. Ames, M. K. Shigenaga, and T. M. Hagen, "Oxidants, antioxidants, and the degenerative diseases of aging." *Proceedings of the National Academy of Sciences*, vol. 90, no. 17, p. 7915–7922, 1993.

[56] T. Lindahl, "Instability and decay of the primary structure of dna," *Nature*, vol. 362, no. 6422, p. 709–715, 1993.

[57] K. W. Caldecott, "Single-strand break repair and genetic disease," *Nature Reviews Genetics*, vol. 9, no. 8, p. 619–631, 2008.

[58] M. M. Vilenchik and A. G. Knudson, "Endogenous dna double-strand breaks: Production, fidelity of repair, and induction of cancer," *Proceedings of the National Academy of Sciences*, vol. 100, no. 22, p. 12871–12876, 2003.

[59] R. Roots and S. Okada, "Protection of dna molecules of cultured mammalian cells from radiation-induced single-strand scissions by various alcohols and sh compounds," *International Journal of Radiation Biology and Related Studies in Physics, Chemistry and Medicine*, vol. 21, no. 4, p. 329–342, 1972.

[60] H. Nikjoo, C. E. Bolton, R. Watanabe, M. Terrissol, P. Oneill, and D. T. Goodhead, "Modelling of dna damage induced by energetic electrons (100 ev to 100 kev)," *Radiation Protection Dosimetry*, vol. 99, no. 1, p. 77–80, 2002.

[61] J. F. Ward, "Nature of lesions formed by ionizing radiation," *DNA Damage and Repair*, p. 65–84, 1998.

[62] L. F. Povirk, "Dna damage and mutagenesis by radiomimetic dna-cleaving agents: bleomycin, neocarzinostatin and other enediynes," *Mutation Research/Fundamental and Molecular Mechanisms of Mutagenesis*, vol. 355, no. 1-2, p. 71–89, 1996.

[63] M. M. Greenberg, "Pyrimidine nucleobase radical reactivity in dna and rna," *Radiation Physics and Chemistry*, vol. 128, p. 82–91, 2016.

[64] M. Dizdaroglu and P. Jaruga, "Mechanisms of free radical-induced damage to dna," *Free Radical Research*, vol. 46, no. 4, p. 382–419, 2012.

[65] J. D. Chapman, A. P. Reuvers, J. Borsa, and C. L. Greenstock, "Chemical radioprotection and radiosensitization of mammalian cells growing in vitro," *Radiation Research*, vol. 56, no. 2, 11 1973. [Online]. Available: https://www.osti.gov/biblio/4387536

[66] C. v. Sonntag, *The chemical basis of radiation biology*. Taylor Francis, 1989.

[67] P. Oneill, "Radiation-induced damage in dna," *Radiation Chemistry - Present Status and Future Trends Studies in Physical and Theoretical Chemistry*, p. 585–622, 2001.

[68] B. Balasubramanian, W. K. Pogozelski, and T. D. Tullius, "Dna strand breaking by the hydroxyl radical is governed by the accessible surface areas of the hydrogen atoms of the dna backbone," *Proceedings of the National Academy of Sciences*, vol. 95, no. 17, p. 9738–9743, 1998.

[69] M. Talpaert-Borlè, "Formation, detection and repair of ap sites," *Mutation Research/-Fundamental and Molecular Mechanisms of Mutagenesis*, vol. 181, no. 1, p. 45–56, 1987.

[70] J. R. Milligan, J. A. Aguilera, and J. F. Ward, "Variation of single-strand break yield with scavenger concentration for plasmid dna irradiated in aqueous solution," *Radiation Research*, vol. 133, no. 2, p. 151, 1993.

[71] K. Van Rijn, T. Mayer, J. Blok, J. Verberne, and H. Loman, "Reaction rate of oh radicals with x174 dna: Influence of salt and scavenger," *International Journal of Radiation Biology and Related Studies in Physics, Chemistry and Medicine*, vol. 47, no. 3, p. 309–317, 1985.

[72] P. Riley, "Free radicals in biology: Oxidative stress and the effects of ionizing radiation," *International Journal of Radiation Biology*, vol. 65, no. 1, p. 27–33, 1994.

[73] M. Ljungman, S. Nyberg, J. Nygren, M. Eriksson, G. Ahnström, and G. Ahnstrom, "Dna-bound proteins contribute much more than soluble intracellular compounds to the intrinsic protection against radiation-induced dna strand breaks in human cells," *Radiation Research*, vol. 127, no. 2, p. 171, 1991.

[74] E. Sage and N. Shikazono, "Radiation-induced clustered dna lesions: Repair and mutagenesis," *Free Radical Biology and Medicine*, vol. 107, p. 125–135, 2017.

[75] J. A. Nickoloff, N. Sharma, and L. Taylor, "Clustered dna double-strand breaks: Biological effects and relevance to cancer radiotherapy," *Genes*, vol. 11, no. 1, p. 99, 2020.

[76] M. Hada and B. M. Sutherland, "Spectrum of complex dna damages depends on the incident radiation," *Radiation Research*, vol. 165, no. 2, p. 223–230, 2006.

[77] K. Ledingham, P. Bolton, N. Shikazono, and C.-M. Ma, "Towards laser driven hadron cancer radiotherapy: A review of progress," *Applied Sciences*, vol. 4, no. 3, p. 402–443, 2014.

[78] J. I. Friedman and J. T. Stivers, "Detection of damaged dna bases by dna glycosylase enzymes," *Biochemistry*, vol. 49, no. 24, p. 4957–4967, 2010.

[79] Y. Liu, R. Prasad, W. A. Beard, P. S. Kedar, E. W. Hou, D. D. Shock, and S. H. Wilson, "Coordination of steps in single-nucleotide base excision repair mediated by apurinic/apyrimidinic endonuclease 1 and dna polymerase ," *Journal of Biological Chemistry*, vol. 282, no. 18, p. 13532–13541, 2007.

[80] K. Datta, R. D. Neumann, and T. A. Winters, "Characterization of complex apurinic/apyrimidinic-site clustering associated with an authentic site-specific radiation-

induced dna double-strand break," *Proceedings of the National Academy of Sciences*, vol. 102, no. 30, p. 10569–10574, 2005.

[81] D. Goodhead, "Initial events in the cellular effects of ionizing radiations: Clustered damage in dna," *International Journal of Radiation Biology*, vol. 65, no. 1, p. 7–17, 1994.

[82] J. F. Ward, "Radiation mutagenesis: The initial dna lesions responsible," *Radiation Research*, vol. 142, no. 3, p. 362, 1995.

[83] S. Lehnert, *Biomolecular Action of Ionizing Radiation*. CRC Press, 2007.

[84] L. Huang, A. R. Snyder, and W. F. Morgan, "Radiation-induced genomic instability and its implications for radiation carcinogenesis," *Oncogene*, vol. 22, no. 37, p. 5848–5854, 2003.

[85] D. Hanahan and R. A. Weinberg, "The hallmarks of cancer," *Cell*, vol. 100, no. 1, p. 57–70, 2000.

[86] J. B. Little, "Radiation carcinogenesis," *Carcinogenesis*, vol. 21, no. 3, p. 397–404, 2000.

[87] W. F. Morgan and W. J. Bair, "Issues in low dose radiation biology: The controversy continues. a perspective," *Radiation Research*, vol. 179, no. 5, p. 501–510, 2013.

[88] L. Mullenders, M. Atkinson, H. Paretzke, L. Sabatier, and S. Bouffler, "Assessing cancer risks of low-dose radiation," *Nature Reviews Cancer*, vol. 9, no. 8, p. 596–604, 2009.

[89] R. W. Harbron, "Cancer risks from low dose exposure to ionising radiation – is the linear no-threshold model still relevant?" *Radiography*, vol. 18, no. 1, p. 28–33, 2012.

[90] N. R. C. of the National Academies, "Health risks from exposures to low levels of ionizing radiation: Beir vii phase 2," *The National Academics Press*, 2006.

[91] M. Fippel, *Basics of Monte Carlo Simulations*. CRC Press, 2013.

[92] M. Berger, *Monte Carlo calculation of the penetration and diffusion of fast charged particles*. Academic Press Inc., 1963, vol. 1, p. 135–215.

[93] M. Tsai, Z. Tian, N. Qin, C. Yan, Y. Lai, S. Hung, Y. Chi, and X. Jia, "A new open-source gpu-based microscopic monte carlo simulation tool for the calculations of dna damages caused by ionizing radiation — part i: Core algorithm and validation," *Medical Physics*, vol. 47, no. 4, p. 1958–1970, 2020.

[94] H. Nikjoo, S. Uehara, D. Emfietzoglou, and F. Cucinotta, "Track-structure codes in radiation research," *Radiation Measurements*, vol. 41, no. 9-10, p. 1052–1074, 2006.

[95] A. Zabihi, J. Tello, S. Incerti, Z. Francis, G. Forozani, F. Semsarha, A. Moslehi, and M. A. Bernal, "Determination of fast neutron rbe using a fully mechanistic computational model," *Applied Radiation and Isotopes*, vol. 156, p. 108952, 2020.

[96] H. N. S. U. W. E. W. M. Ho, "Track structure in radiation biology: theory and applications," *International Journal of Radiation Biology*, vol. 73, no. 4, p. 355–364, 1998.

[97] R. N. Hamm, J. E. Turner, and M. G. Stabin, "Monte carlo simulation of diffusion and reaction in water radiolysis - a study of reactant 'jump through' and jump distances," *Radiation and Environmental Biophysics*, vol. 36, no. 4, p. 229–234, 1998.

[98] J. A. Laverne, "Oh radicals and oxidizing products in the gamma radiolysis of water," *Radiation Research*, vol. 153, no. 2, p. 196–200, 2000.

[99] J.-P. Jay-Gerin and C. Ferradini, "A new estimate of the radical yield at early times in the radiolysis of liquid water," *Chemical Physics Letters*, vol. 317, no. 3-5, p. 388–391, 2000.

[100] C. D. Jonah and J. R. Miller, "Yield and decay of the hydroxyl radical from 200ps to 3ns," *The Journal of Physical Chemistry*, vol. 81, no. 21, p. 1974–1976, 1977.

[101] M. S. Kreipl, W. Friedland, and H. G. Paretzke, "Time- and space-resolved monte carlo study of water radiolysis for photon, electron and ion irradiation," *Radiation and Environmental Biophysics*, vol. 48, no. 1, p. 11–20, 2008.

[102] A. K. E. Omar, U. Schmidhammer, P. Jeunesse, J.-P. Larbre, M. Lin, Y. Muroya, Y. Katsumura, P. Pernot, and M. Mostafavi, "Time-dependent radiolytic yield of oh• radical studied by picosecond pulse radiolysis," *The Journal of Physical Chemistry A*, vol. 115, no. 44, p. 12212–12216, 2011.

[103] H. Shiraishi, Y. Katsumura, D. Hiroishi, K. Ishigure, and M. Washio, "Pulse-radiolysis study on the yield of hydrated electron at elevated temperatures," *The Journal of Physical Chemistry*, vol. 92, no. 10, p. 3011–3017, 1988.

[104] T. Sumiyoshi and M. Katayama, "The yield of hydrated electrons at 30 picoseconds," *Chemistry Letters*, vol. 11, no. 12, p. 1887–1890, 1982.

[105] R. K. Wolff, M. J. Bronskill, J. E. Aldrich, and J. W. Hunt, "Picosecond pulse radiolysis. iv. yield of the solvated electron at 30 picoseconds," *The Journal of Physical Chemistry*, vol. 77, no. 11, p. 1350–1355, 1973.

[106] J. W. Hunt, R. K. Wolff, M. J. Bronskill, C. D. Jonah, E. J. Hart, and M. S. Matheson, "Radiolytic yields of hydrated electrons at 30 to 1000 picoseconds after energy absorption," *The Journal of Physical Chemistry*, vol. 77, no. 3, p. 425–426, 1973.

[107] G. V. Buxton, "Nanosecond pulse radiolysis of aqueous solutions containing proton and hydroxyl radical scavengers," *Proceedings of the Royal Society of London. A. Mathematical and Physical Sciences*, vol. 328, no. 1572, p. 9–21, 1972.

[108] Y. Muroya, M. Lin, G. Wu, H. Iijima, K. Yoshii, T. Ueda, H. Kudo, and Y. Katsumura, "A re-evaluation of the initial yield of the hydrated electron in the picosecond time range," *Radiation Physics and Chemistry*, vol. 72, no. 2-3, p. 169–172, 2005.

[109] A. K. Pikaev, S. A. Kabakchi, and A. A. Zansokhova, "Yields and reactions of hydrogen ions on radiolysis of water and aqueous solutions," *Faraday Discussions of the Chemical Society*, vol. 63, p. 112, 1977.

[110] B. Cercek and M. Kongshaug, "Hydrogen ion yields in the radiolysis of neutral aqueous solutions," *The Journal of Physical Chemistry*, vol. 73, no. 6, p. 2056–2058, 1969.

[111] R. F. Anderson, B. Vojnovic, and B. D. Michael, "The radiation-chemical yields of h3o and oh- as determined by nanosecond conductimetric measurements," *Radiation Physics and Chemistry (1977)*, vol. 26, no. 3, p. 301–303, 1985.

[112] K. H. Schmidt and S. M. Ander, "Formation and recombination of the hydronium ion (h3o ) and hydroxide in irradiated water," *The Journal of Physical Chemistry*, vol. 73, no. 9, p. 2846–2852, 1969.

[113] Z. D. Draganić and I. G. Draganić, "Formation of primary hydrogen atom yield (gh) in the .gamma. radiolysis of water," *The Journal of Physical Chemistry*, vol. 76, no. 19, p. 2733–2737, 1972.

[114] Z. Draganić and I. Draganić, "Formation of primary reducing yields (geaq- and gh2) in the radiolysis of aqueous solutions of some positive ions," *International Journal for Radiation Physics and Chemistry*, vol. 7, no. 2-3, p. 381–386, 1975.

[115] K. Niita, T. Sato, H. Iwase, H. Nose, H. Nakashima, and L. Sihver, "Phits—a particle and heavy ion transport code system," *Radiation Measurements*, vol. 41, no. 9-10, p. 1080–1090, 2006.

[116] A. Ferrari, *Fluka: a multi-particle transport code*, 2005.

[117] W. R. Nelson, H. Hirayama, and D. W. Rogers, "Egs4 code system," 12 1985. [Online]. Available: https://www.osti.gov/biblio/6137659

[118] J. Baró, J. Sempau, J. Fernández-Varea, and F. Salvat, "Penelope: An algorithm for monte carlo simulation of the penetration and energy loss of electrons and positrons in matter," *Nuclear Instruments and Methods in Physics Research Section B: Beam Interactions with Materials and Atoms*, vol. 100, no. 1, p. 31–46, 1995.

[119] S. Agostinelli, J. Allison, K. Amako, J. Apostolakis, H. Araujo, P. Arce, M. Asai, D. Axen, S. Banerjee, G. Barrand, and et al., "Geant4—a simulation toolkit," *Nuclear Instruments and Methods in Physics Research Section A: Accelerators, Spectrometers, Detectors and Associated Equipment*, vol. 506, no. 3, p. 250–303, 2003.

[120] N. Schetakis, R. Crespo, J. L. Vázquez-Poletti, M. Sastre, L. Vázquez, and A. Di Iorio, "Overview of main radiation transport codes," 2020.

[121] W. E. Wilson, D. J. Lynch, K. Wei, and L. A. Braby, "Microdosimetry of a 25 kev electron microbeam," *Radiation Research*, vol. 155, no. 1, p. 89–94, 2001.

[122] M. Dingfelder, D. Hantke, M. Inokuti, and H. G. Paretzke, "Electron inelastic-scattering cross sections in liquid water," *Radiation Physics and Chemistry*, vol. 53, no. 1, p. 1–18, 1998.

[123] T. Liamsuwan, D. Emfietzoglou, S. Uehara, and H. Nikjoo, "Microdosimetry of low-energy electrons," *International Journal of Radiation Biology*, vol. 88, no. 12, p. 899–907, 2012.

[124] V. A. Semenenko, J. E. Turner, and T. B. Borak, "Norec, a monte carlo code for simulating electron tracks in liquid water," *Radiation and Environmental Biophysics*, vol. 42, no. 3, p. 213–217, 2003.

[125] B. Grosswendt, "Formation of ionization clusters in nanometric structures of propane-based tissue-equivalent gas or liquid water by electrons and -particles," *Radiation and Environmental Biophysics*, vol. 41, no. 2, p. 103–112, 2002.

[126] C. Wälzlein, E. Scifoni, M. Krämer, and M. Durante, "Simulations of dose enhancement for heavy atom nanoparticles irradiated by protons," *Physics in Medicine and Biology*, vol. 59, no. 6, p. 1441–1458, 2014.

[127] I. Plante and F. A., "Monte-carlo simulation of ionizing radiation tracks," *Applications of Monte Carlo Methods in Biology, Medicine and Other Fields of Science*, 2011.

[128] S. Incerti, G. Baldacchino, M. Bernal, R. Capra, C. Champion, Z. Francis, P. Gueye, A. Mantero, B. Mascialino, P. Moretto, and et al., "The geant4-dna project," *International Journal of Modeling, Simulation, and Scientific Computing*, vol. 01, no. 02, p. 157–178, 2010.

[129] J. Allison, K. Amako, J. Apostolakis, P. Arce, M. Asai, T. Aso, E. Bagli, A. Bagulya, S. Banerjee, G. Barrand, and et al., "Recent developments in geant4," *Nuclear Instruments and Methods in Physics Research Section A: Accelerators, Spectrometers, Detectors and Associated Equipment*, vol. 835, p. 186–225, 2016.

[130] S. Incerti, I. Kyriakou, M. A. Bernal, M. C. Bordage, Z. Francis, S. Guatelli, V. Ivanchenko, M. Karamitros, N. Lampe, S. B. Lee, and et al., "Geant4-dna example applications for track structure simulations in liquid water: A report from the geant4-dna project," *Medical Physics*, vol. 45, no. 8, 2018.

[131] J. Perl, J. Shin, J. Schümann, B. Faddegon, and H. Paganetti, "Topas: An innovative proton monte carlo platform for research and clinical applications," *Medical Physics*, vol. 39, no. 11, p. 6818–6837, 2012.

[132] B. Faddegon, J. Ramos-Méndez, J. Schuemann, A. McNamara, J. Shin, J. Perl, and H. Paganetti, "The topas tool for particle simulation, a monte carlo simulation tool for physics, biology and clinical research," *Physica Medica*, vol. 72, p. 114–121, 2020.

[133] J. Schuemann, A. L. McNamara, J. Ramos-Méndez, J. Perl, K. D. Held, H. Paganetti, S. Incerti, and B. Faddegon, "TOPAS-nBio: An Extension to the TOPAS Simulation Toolkit for Cellular and Sub-cellular Radiobiology," *Radiation Research*, vol. 191, no. 2, pp. 125–138, 2019. [Online]. Available: https://doi.org/10.1667/rr15226.1

[134] J. Schuemann, *TOPAS-nBio Documentation Release 1.0*, 2021, version 1.0. [Online]. Available: https://topas-nbio.readthedocs.io/_/downloads/en/latest/pdf/

[135] J. W. Warmenhoven, N. T. Henthorn, S. P. Ingram, A. L. Chadwick, M. Sotiropoulos, N. Korabel, S. Fedotov, R. I. Mackay, K. J. Kirkby, M. J. Merchant, and et al., "Insights into the non-homologous end joining pathway and double strand break end mobility provided by mechanistic in silico modelling," *DNA Repair*, vol. 85, p. 102743, 2020.

[136] S. J. McMahon, J. Schuemann, H. Paganetti, and K. M. Prise, "Mechanistic modelling of dna repair and cellular survival following radiation-induced dna damage," *Scientific Reports*, vol. 6, no. 1, 2016.

[137] H. Nikjoo, P. Oneill, W. E. Wilson, and D. T. Goodhead, "Computational approach for determining the spectrum of dna damage induced by ionizing radiation," *Radiation Research*, vol. 156, no. 5, p. 577–583, 2001.

[138] W. Friedland, P. Jacob, P. Bernhardt, H. G. Paretzke, and M. Dingfelder, "Simulation of dna damage after proton irradiation," *Radiation Research*, vol. 159, no. 3, p. 401–410, 2003.

[139] W. Friedland, M. Dingfelder, P. Kundrát, and P. Jacob, "Track structures, dna targets and radiation effects in the biophysical monte carlo simulation code partrac," *Mutation Research/Fundamental and Molecular Mechanisms of Mutagenesis*, vol. 711, no. 1-2, p. 28–40, 2011.

[140] W. Friedland, E. Schmitt, P. Kundrát, M. Dingfelder, G. Baiocco, S. Barbieri, and A. Ottolenghi, "Comprehensive track-structure based evaluation of dna damage by light

ions from radiotherapy-relevant energies down to stopping," *Scientific Reports*, vol. 7, no. 1, 2017.

[141] S. Meylan, S. Incerti, M. Karamitros, N. Tang, M. Bueno, I. Clairand, and C. Villagrasa, "Simulation of early dna damage after the irradiation of a fibroblast cell nucleus using geant4-dna," *Scientific Reports*, vol. 7, no. 1, 2017.

[142] N. Lampe, M. Karamitros, V. Breton, J. M. Brown, D. Sakata, D. Sarramia, and S. Incerti, "Mechanistic dna damage simulations in geant4-dna part 2: Electron and proton damage in a bacterial cell," *Physica Medica*, vol. 48, p. 146–155, 2018.

[143] M. Mokari, M. H. Alamatsaz, H. Moeini, and R. Taleei, "A simulation approach for determining the spectrum of dna damage induced by protons," *Physics in Medicine Biology*, vol. 63, no. 17, p. 175003, 2018.

[144] D. Sakata, O. Belov, M.-C. Bordage, D. Emfietzoglou, S. Guatelli, T. Inaniwa, V. Ivanchenko, M. Karamitros, I. Kyriakou, N. Lampe, and et al., "Fully integrated monte carlo simulation for evaluating radiation induced dna damage and subsequent repair using geant4-dna," *Scientific Reports*, vol. 10, no. 1, 2020.

[145] W. Friedland, P. Bernhardt, P. Jacob, and H. G. Paretzke, "Simulation of dna damage after proton and low let irradiation," *Radiation Protection Dosimetry*, vol. 99, no. 1, p. 99–102, 2002.

[146] N. T. Henthorn, J. W. Warmenhoven, M. Sotiropoulos, A. H. Aitkenhead, E. A. Smith, S. P. Ingram, N. F. Kirkby, A. Chadwick, N. G. Burnet, R. I. Mackay, and et al., "Clinically relevant nanodosimetric simulation of dna damage complexity from photons and protons," *RSC Advances*, vol. 9, no. 12, p. 6845–6858, 2019.

[147] A. Ottolenghi, V. Smyth, and K. Trott, "Assessment of cancer risk from neutron exposure – the andante project," *Radiation Measurements*, vol. 57, p. 68–73, 2013.

[148] A. Ottolenghi, G. Baiocco, V. Smyth, and K. Trott, "The andante project: A multidisciplinary approach to neutron rbe," *Radiation Protection Dosimetry*, vol. 166, no. 1-4, p. 311–315, 2015.

[149] G. Famulari, P. Pater, and S. A. Enger, "Microdosimetry calculations for monoenergetic electrons using geant4-dna combined with a weighted track sampling algorithm," *Physics in Medicine amp; Biology*, vol. 62, no. 13, p. 5495–5508, 2017.

[150] N. Tang, M. Bueno, S. Meylan, S. Incerti, H. N. Tran, A. Vaurijoux, G. Gruel, and C. Villagrasa, "Influence of chromatin compaction on simulated early radiation-induced dna damage using geant4-dna," *Medical Physics*, vol. 46, no. 3, p. 1501–1511, 2019.

[151] C. Villagrasa, S. Meylan, G. Gonon, G. Gruel, U. Giesen, M. Bueno, and H. Rabus, "Geant4-dna simulation of dna damage caused by direct and indirect radiation effects and comparison with biological data." *EPJ Web of Conferences*, vol. 153, p. 04019, 2017.

[152] A. L. McNamara, J. Ramos-Méndez, J. Perl, K. Held, N. Dominguez, E. Moreno, N. T. Henthorn, K. J. Kirkby, S. Meylan, C. Villagrasa, and et al., "Geometrical structures for radiation biology research as implemented in the topas-nbio toolkit," *Physics in Medicine amp; Biology*, vol. 63, no. 17, p. 175018, 2018.

[153] E. Lieberman-Aiden, N. L. van Berkum, L. Williams, M. Imakaev, T. Ragoczy, A. Telling, I. Amit, B. R. Lajoie, P. J. Sabo, M. O. Dorschner, and et al., "Comprehensive mapping of long-range interactions reveals folding principles of the human genome," *Science*, vol. 326, no. 5950, p. 289–293, 2009.

[154] A. I. Lamond and J. E. Sleeman, "Nuclear substructure and dynamics," *Current Biology*, vol. 13, no. 21, 2003.

[155] L. Seaman, W. Meixner, J. Snyder, and I. Rajapakse, "Periodicity of nuclear morphology in human fibroblasts," *Nucleus*, vol. 6, no. 5, p. 408–416, 2015.

[156] M. A. Śmiałek, N. C. Jones, S. V. Hoffmann, and N. J. Mason, "Measuring the density of dna films using ultraviolet-visible interferometry," *Physical Review E*, vol. 87, no. 6, 2013.

[157] H. Nikjoo, P. O'Neill, D. T. Goodhead, and M. Terrissol, "Computational modelling of low-energy electron-induced dna damage by early physical and chemical events," *International Journal of Radiation Biology*, vol. 71, no. 5, p. 467–483, 1997.

[158] R. Watanabe, S. Rahmanian, and H. Nikjoo, "Spectrum of radiation-induced clustered non-dsb damage – a monte carlo track structure modeling and calculations," *Radiation Research*, vol. 183, no. 5, p. 525–540, 2015.

[159] M. Mokari, H. Moeini, M. Soleimani, and E. Fereidouni, "Calculation and comparison of the direct and indirect dna damage induced by low energy electrons using default and cpa100 cross section models within geant4-dna," *Nuclear Instruments and Methods in Physics Research Section B: Beam Interactions with Materials and Atoms*, vol. 480, p. 56–66, 2020.

[160] D. Charlton and J. Humm, "A method of calculating initial dna strand breakage following the decay of incorporated125i," *International Journal of Radiation Biology*, vol. 53, no. 3, p. 353–365, 1988.

[161] G. van der Schans, "Gamma-ray induced double-strand breaks in dna resulting from randomly-inflicted single-strand breaks: Temporal local denaturation, a new radiation phenomenon?" *International Journal of Radiation Biology and Related Studies in Physics, Chemistry and Medicine*, vol. 33, no. 2, p. 105–120, 1978.

[162] D. Emfietzoglou, "Inelastic cross-sections for electron transport in liquid water: A comparison of dielectric models," *Radiation Physics and Chemistry*, vol. 66, no. 6, p. 373–385, 2003.

[163] I. Kyriakou, S. Incerti, and Z. Francis, "Technical note: Improvements in geant4 energy-loss model and the effect on low-energy electron transport in liquid water," *Medical Physics*, vol. 42, no. 7, p. 3870–3876, 2015.

[164] C. Champion, S. Incerti, H. Aouchiche, and D. Oubaziz, "A free-parameter theoretical model for describing the electron elastic scattering in water in the geant4 toolkit," *Radiation Physics and Chemistry*, vol. 78, no. 9, p. 745–750, 2009.

[165] S. Uehara, H. Nikjoo, and D. T. Goodhead, "Cross-sections for water vapour for the monte carlo electron track structure code from 10 ev to the mev region," *Physics in Medicine and Biology*, vol. 38, no. 12, p. 1841–1858, 1993.

[166] M. Michaud, A. Wen, and L. Sanche, "Cross sections for low-energy (1–100 ev) electron elastic and inelastic scattering in amorphous ice," *Radiation Research*, vol. 159, no. 1, p. 3–22, 2003.

[167] C. E. Melton, "Cross sections and interpretation of dissociative attachment reactions producing oh, o, and hin h2o," *The Journal of Chemical Physics*, vol. 57, no. 10, p. 4218–4225, 1972.

[168] D. Emfietzoglou and H. Nikjoo, "The effect of model approximations on single-collision distributions of low-energy electrons in liquid water," *Radiation Research*, vol. 163, no. 1, p. 98–111, 2005.

[169] M. Dingfelder, M. Inokuti, and H. G. Paretzke, "Inelastic-collision cross sections of liquid water for interactions of energetic protons," *Radiation Physics and Chemistry*, vol. 59, no. 3, p. 255–275, 2000.

[170] M. E. Rudd, T. V. Goffe, R. D. DuBois, and L. H. Toburen, "Cross sections for ionization of water vapor by 7–4000-kev protons," *Physical Review A*, vol. 31, no. 1, p. 492–494, 1985.

[171] M. E. Rudd, Y. K. Kim, D. H. Madison, and T. J. Gay, "Electron production in proton collisions with atoms and molecules: Energy distributions," *Reviews of Modern Physics*, vol. 64, no. 2, p. 441–490, 1992.

[172] H. Tran, Z. El Bitar, C. Champion, M. Karamitros, M. Bernal, Z. Francis, V. Ivantchenko, S. Lee, J. Shin, S. Incerti, and et al., "Modeling proton and alpha elastic scattering in liquid water in geant4-dna," *Nuclear Instruments and Methods in Physics Research Section B: Beam Interactions with Materials and Atoms*, vol. 343, p. 132–137, 2015.

[173] M. Dingfelder, H. Paretzke, and L. Toburen, "An effective charge scaling model for ionization of partially dressed helium ions with liquid water," in *Proceedings of the Monte Carlo 2005 Topical Meeting*, 2005.

[174] J. Perl, D. Hall, J. Shin, J. Schuemann, and J. Ramos-Méndez, "Modular physics lists," 2016. [Online]. Available: https://topas.readthedocs.io/en/latest/parameters/physics/modular.html

[175] C. R. Harris, K. J. Millman, S. J. van der Walt, R. Gommers, P. Virtanen, D. Cournapeau, E. Wieser, J. Taylor, S. Berg, N. J. Smith, R. Kern, M. Picus, S. Hoyer, M. H. van Kerkwijk, M. Brett, A. Haldane, J. F. del Río, M. Wiebe, P. Peterson, P. Gérard-Marchant, K. Sheppard, T. Reddy, W. Weckesser, H. Abbasi, C. Gohlke, and T. E. Oliphant, "Array programming with NumPy," *Nature*, vol. 585, no. 7825, pp. 357–362, Sep. 2020. [Online]. Available: https://doi.org/10.1038/s41586-020-2649-2

[176] W. McKinney *et al.*, "Data structures for statistical computing in python," in *Proceedings of the 9th Python in Science Conference*, vol. 445. Austin, TX, 2010, pp. 51–56.

[177] J. D. Hunter, "Matplotlib: A 2d graphics environment," *Computing in Science & Engineering*, vol. 9, no. 3, pp. 90–95, 2007.

[178] D. Frankenberg, H. J. Brede, U. J. Schrewe, C. Steinmetz, M. Frankenberg-Schwager, G. Kasten, and E. Pralle, "Induction of dna double-strand breaks by 1 h and 4 he ions in primary human skin fibroblasts in the let range of 8 to 124 kev/$\mu$m," *Radiation Research*, vol. 151, no. 5, p. 540, 1999.

[179] M. Belli, R. Cherubini, and M. Dalla Vecchia, "Dna dsb induction and rejoining in v79 cells irradiated with light ions: A constant field gel electrophoresis study," *International Journal of Radiation Biology*, vol. 76, no. 8, p. 1095–1104, 2000.

[180] M. Belli, R. Cherubini, M. Dalla Vecchia, V. Dini, G. Esposito, G. Moschini, O. Sapora, C. Signoretti, G. Simone, E. Sorrentino, and et al., "Dna fragmentation in mammalian cells exposed to various light ions," *Advances in Space Research*, vol. 27, no. 2, p. 393–399, 2001.

[181] A. Campa, F. Ballarini, M. Belli, R. Cherubini, V. Dini, G. Esposito, W. Friedland, S. Gerardi, S. Molinelli, A. Ottolenghi, and et al., "Dna dsb induced in human cells by charged particles and gamma rays: Experimental results and theoretical approaches," *International Journal of Radiation Biology*, vol. 81, no. 11, p. 841–854, 2005.

[182] "Cedar - cc doc," Mar 2021. [Online]. Available: https://docs.computecanada.ca/wiki/Cedar

[183] J. Schuemann, "Simulation crash for high let," Mar 2021. [Online]. Available: https://groups.google.com/u/2/g/topas-nbio-users/c/SnaOA-kSRl4/m/1NYTZ-3VAQAJ?pli=1

[184] H. Zhu, A. L. McNamara, J. Ramos-Mendez, S. J. McMahon, N. T. Henthorn, B. Faddegon, K. D. Held, J. Perl, J. Li, H. Paganetti, and et al., "A parameter sensitivity study for simulating dna damage after proton irradiation using topas-nbio," *Physics in Medicine amp; Biology*, vol. 65, no. 8, p. 085015, 2020.

[185] A. Asokan and M. J. Cho, "Exploitation of intracellular ph gradients in the cellular delivery of macromolecules," *Journal of Pharmaceutical Sciences*, vol. 91, no. 4, p. 903–913, 2002.

[186] E. Proksch, "Ph in nature, humans and skin," *The Journal of Dermatology*, vol. 45, no. 9, p. 1044–1052, 2018.

[187] I. I. Geneva, B. Cuzzo, T. Fazili, and W. Javaid, "Normal body temperature: A systematic review," *Open Forum Infectious Diseases*, vol. 6, no. 4, 2019.